A Velocity Decomposition Approach for Lifting and Free-surface Flows

by

William J. Rosemurgy IV

A dissertation submitted in partial fulfillment
of the requirements for the degree of
Doctor of Philosophy
(Naval Architecture and Marine Engineering)
in the University of Michigan
2014

Doctoral Committee:

Professor Robert F. Beck, Co-Chair
Assistant Professor Kevin J. Maki, Co-Chair
Professor William W. Schultz
Professor Armin W. Troesch

To my dad and grandparents who made me believe I could do anything. And to Tiffany for being there every step of the way.

ACKNOWLEDGMENTS

I've been very lucky to have two advisors who have been so involved and dedicated to my personal and academic development. I must begin by thanking Dr. Kevin Maki who gave me my first research opportunity years ago. For years he has been a great mentor and friend who has a passion for knowledge (including hydrodynamics) that is contagious. I'll always remember riding the rail on *Stripes* discussing my research as we sailed along. It has also been a pleasure to work closely with Prof. Robert Beck. His willingness to teach and share his expertise has been a great asset as I've progressed through my research; I learned something new each and every time we met. I am also grateful for the engaging and challenging discussions that I've had with Prof. Armin Troesch and Prof. William Schultz.

I am forever in debt to my partner, Tiffany, who has supported, encouraged, motivated, comforted, and nourished me daily throughout this long journey. Also, to my dad and grandparents who have offered constant encouragement and support for as long as I can remember.

I have enjoyed the company of friends - Pete, Taylor, Greg, Nastowe, Kramer, Woolli, Cuneo, and many others - who have been there to celebrate, relax, and listen to me complain. In addition, I appreciate the previous work put forth by Deborah Edmund on this research topic.

I am very grateful to the Office of Naval Research for funding my research and supporting me. Travel funds were also generously provided through the Rackham Graduate School.

TABLE OF CONTENTS

LIST OF FIGURES

LIST OF TABLES

LIST OF ACRONYMS

2D Two-Dimensional

3D Three-Dimensional

CFD Computational Fluid Dynamics

RANS Reynolds-Averaged Navier-Stokes

N-S Navier-Stokes

LIST OF SYMBOLS

$\mathbf{u}$ total fluid velocity

$\mathbf{x}$ position vector

Φ total inviscid potential

φ total viscous potential

ϕ viscous perturbation potential

U_∞ free-stream velocity

$\mathbf{w}$ vortical velocity

δ thickness of vortical region

p total fluid pressure

p_d dynamic fluid pressure

$\boldsymbol{\omega}$ vorticity vector

$\overline{\mathbf{u}}$ Reynolds-averaged component of total velocity

$\mathbf{u}'$ fluctuating compononent of total velocity

$\overline{p_d}$ Reynolds-averaged component of dynamic pressure

$p_d{}'$ fluctuating component of dynamic pressure

k turbulent kinetic energy

$\hat{i}$ unit normal vector in x-dir

$\hat{k}$ unit normal vector in z-dir

ρ fluid density

ν kinematic viscosity

ν_t eddy viscosity

μ dynamic viscosity

$\mathbf{g}$ gravity vector

g magnitude of the gravity vector

η free-surface elevation

N_{body} number of body panels

l_{panel} panel length

Γ total circulation around the body

σ strength of source distribution

μ strength of dipole distribution

γ strength of vortex distribution

γ_0 strength of constant vortex panel

γ_1 slope of linearly vayring vortex panel

h submergence depth

H height of bottom-mounted bump

c foil chordlength

t foil thickness

α angle of attack

C_p coefficient of pressure

λ_0 fundamental wavelength

s wave steepness

Re Reynolds number

Fn_c Froude number based on chord length

Fn_h Froude number based on depth of submergence

y^+ nondimensional near-wall spacing

$\hat{n}$ body normal vector

$\hat{t}$ body tangent vector

$\mathcal{F}$ total force on body

$\mathcal{L}$ total lift on body

C_L lift coefficient

C_D drag coefficient

χ body boundary condition for the viscous potential

$w_n(\delta)$ body boundary condition for the viscous potential

$\partial\Omega_{\mathrm{B}}$ body surface

$\partial\Omega_{\mathrm{W}}$ wake surface

$\partial\Omega_{\mathrm{F}}$ free surface at the air-water interface

$\partial\Omega_{\infty}$ boundary at infinity

$\partial\Omega_I$ inlet boundary

$\partial\Omega_{\mathrm{E}}$ inlet & far-field boundaries of the Navier-Stokes sub-problem

$\partial\Omega_{\mathrm{O}}$ downstream boundary of the Navier-Stokes sub-problem

x_{in} distance from the body to the upstream boundary of the Navier-Stokes domain

x_{out} distance from the body to the downstream boundary of the Navier-Stokes domain

x_{extent} distance from the body to the boundaries of the Navier-Stokes domain

N_λ number of sources per wavelength

N_{FS} total number of sources

x_{up} location of the upstream free-surface boundary

x_{down} location of the downstream free-surface boudary

N_{wake} number of wake panels

Δ_{wake} initial spacing of wake panels

ζ_{wake} wake growth coefficient

l_{wake} total length of the wake surface

$\beta_{\boldsymbol{\omega}}$ threshold value of vorticity

$\delta_{\max}$ maximum value of δ

ϵ_φ parameter governing the convergence of the viscous potential inner loops

res_{update} parameter governing the velocity decomposition updates

N_{updates} number of velocity decomposition updates

res_{final} convergence of the Navier-Stokes solver

ABSTRACT

A Velocity Decomposition Approach for

Lifting and Free-surface Flows

by

William J. Rosemurgy IV

Chair: Robert F. Beck & Kevin J. Maki

The principle of velocity decomposition is used to efficiently and accurately solve the Navier-Stokes problem for lifting and free-surface flows. The total fluid velocity is decomposed as the sum of irrotational and solenoidal components. The irrotational component is modeled using a velocity potential which satisfies the Laplace equation. It is shown that the conventional *inviscid* velocity potential does not satisfy the Navier-Stokes problem, even in the irrotational regions of the flow. Whereas, the *viscous* velocity potential is the solution to a modified boundary-value problem which satisfies the Navier-Stokes problem everywhere except where the flow is rotational.

If a viscous potential can be found which satisfies the Navier-Stokes problem directly outside of the rotational regions of the fluid, then the fluid domain over which the Navier-Stokes equations must be solved can be greatly reduced. The viscous potential is the Dirichlet boundary condition for the total velocity on the boundaries of the reduced fluid domain.

The primary development in this work is the formulation of the viscous potential for lifting and free-surface flows. Previously, the viscous potential was developed by Edmund (2012) for deeply-submerged, non-lifting bodies. In Edmund (2012), the

body-boundary condition was modified to include viscous effects from the body and wake. The viscous potential for lifting flows is modified further to account for the loss of lift due to separation by introducing a condition on the total body-bound circulation. The viscous potential is also modified to account for the presence of an asymmetric flow, such as that which exists downstream of a lifting foil. Finally, free-surface effects are incorported by implementing a linear free-surface solver into the viscous potential formulation.

The velocity decomposition approach is used to solve for the flow over a deeply-submerged 2D NACA0012 foil. It is demonstrated that by using the viscous potential, the fluid domain on which the Navier-Stokes equations are solved can be reduced to only include the region within approximately two chord lengths from the body. A computational speed-up of up to 7.5$\times$ is demonstrated. The velocity decomposition approach is also applied to the free-surface flow over a bottom-mounted bump and a fully-submerged foil.

CHAPTER 1

Introduction

The solution of steady, viscous free-surface problems in naval hydrodynamics is a very important task for a naval architect. For example, the steady lift and drag on a body are needed at the earliest stages of design in order to correctly calculate sinkage and trim of vessel, to accurately size the prime mover, or to perform optimization of the shape of the body. These quantities can be determined experimentally or numerically. While experimental methods are well established, they can be very expensive in terms of time and financial cost and also suffer from extrapolation error when full-scale values are approximated from model-scale results. Numerical simulations, on the other hand, have a large range of costs associated depending on the level of accuracy needed.

Typically, potential flow approaches or viscous Computational Fluid Dynamics (CFD) techniques are used to numerically solve the mathematical problem which models a real-world situation. Potential flow methods are appropriate when the effects of viscosity such as boundary-layer thickness, boundary-layer separation, stall, or the effects of a viscous wake can be ignored. When it is important to capture the effects of viscosity, then CFD must be used to solve the viscous flow equations such as the Navier-Stokes (N-S) equations or Reynolds-Averaged Navier-Stokes (RANS) equations. The goal of this research is to use the principle of velocity decomposition to combine the time savings of potential flow with the higher level of accuracy that

fully viscous approaches can provide.

In the velocity decomposition used in this work, the velocity vector is decomposed using a Helmholtz-like decomposition into to an irrotational (curl-free) component and solenoidal (divergence-free) component, Eq. (1.1).

$$\mathbf{u} = \nabla\Phi + \mathbf{w} \tag{1.1}$$

Where $\mathbf{u}$ is the total fluid velocity and satisfies the Navier-Stokes problem, $\nabla\Phi$ is the the irrotational component and is modeled with using a velocity potential, and $\mathbf{w}$ is the rotational component of the velocity. The region over which the rotational flow is solved is reduced to the regions only where vorticity is present ($|\boldsymbol{\omega}| \neq 0$ and $|\mathbf{w}| \neq 0$). The velocity potential is used to specify the Dirichlet condition for the total velocity on the boundaries of the reduced domain which are placed just outside the vortical regions of the flow ($|\boldsymbol{\omega}| = 0$ and $|\mathbf{w}| = 0$).

In order to fully realize the potential of a velocity decomposition approach to solving viscous flows, the velocity potential must satisfy the Navier-Stokes equations *directly* outside of the vortical regions of the flow. This is not the case for the velocity potential which satisfies conventional boundary conditions. Therefore, modifications must be made to the formulation of the velocity potential problem. In this work, the velocity decomposition approach will be developed for application to lifting and free-surface problems and the modifications to the velocity potential in order to solve these problems will be discussed in full.

The need for a modified velocity potential is motivated by examining the flow over a NACA0012 foil at $\mathrm{Re} = 2000$ with $\alpha = 5°$. Fig. 1.1 shows the total streamwise velocity along a sample line at the midchord of the foil. Also shown is the magnitude of vorticity and streamwise *inviscid* potential velocity along the same line. The inviscid velocity potential is defined as the velocity potential which satisfies the non-penetration condition on the body, Eq. (1.2), and is denoted as Φ. As can be seen in

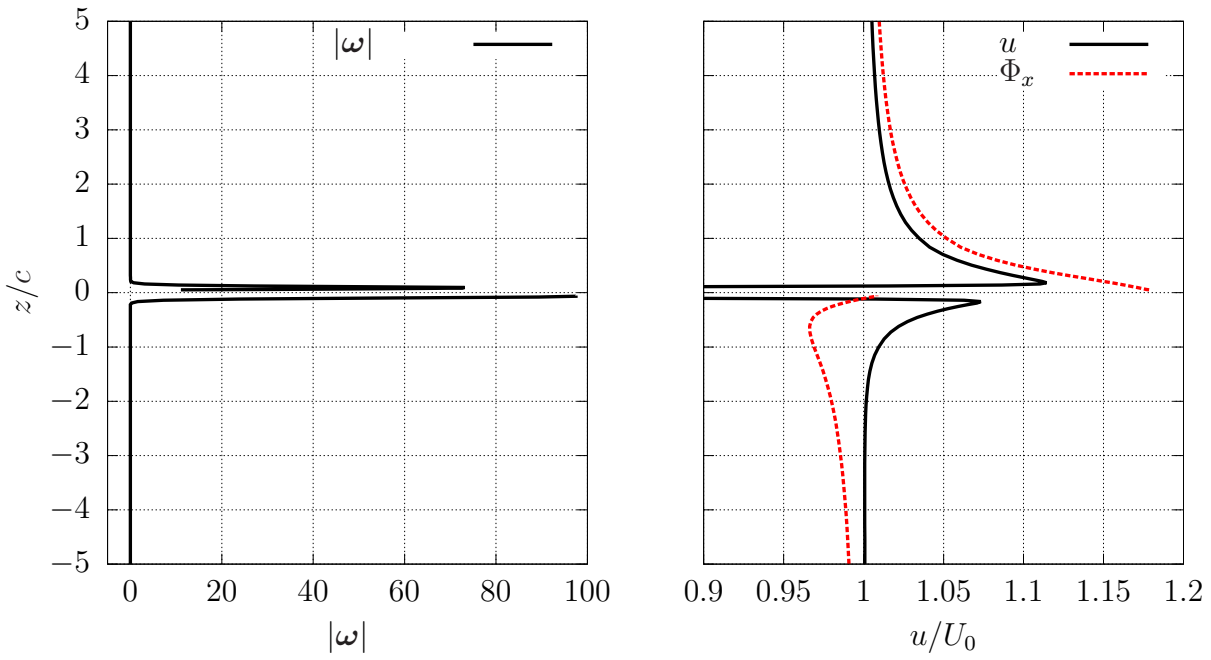

(a) Magnitude of vorticity at the midchord.

(b) Streamwise velocity at the midchord.

Figure 1.1: Vorticity and streamwise velocity over a sample line at the midchord of the NACA0012 foil at $\mathrm{Re} = 2000$ and $\alpha = 5°$.

the figure, the inviscid potential velocity does not match the total velocity, *even* in the region where the flow is irrotational (where the vorticity is negligible).

$$\frac{\partial \Phi}{\partial n} = 0 \qquad \text{on} \qquad \partial\Omega_{\mathrm{B}} \tag{1.2}$$

This simple example is the motivating factor for developing the *viscous* potential, denoted in this work as φ. The viscous potential will satisfy a modified boundary condition on the body, Eq. (1.3), which is not necessarily zero and includes viscous effects.

$$\frac{\partial \varphi}{\partial n} = f(\mathbf{u}) \qquad \text{on} \qquad \partial\Omega_{\mathrm{B}} \tag{1.3}$$

The velocity decomposition used in this work is re-stated in Eq. (1.4), where the

viscous potential is used.

$$\mathbf{u} = \nabla\varphi + \mathbf{w} \tag{1.4}$$

The body-boundary condition for the viscous potential will be further developed in Section 2.4.1. The viscous potential will also be modified to account for the effects of an asymmetric wake, loss of lift due to separation and stall, and the presence of a free surface. The main contribution of this work is the development of a viscous potential for lifting flows and the application of velocity decomposition to lifting and free-surface flows.

1.1 Background

Potential flow methods have been traditionally used to determine wave resistance and are used in conjunction with a friction line to predict total resistance. Michell (1898) presents a concise expression for the wave resistance using his thin-ship theory. The thin-ship theory was developed by linearizing the free-surface and body boundary conditions. As an improvement, Brard (1971) explored the so-called "Neumann-Kelvin" problem. The solution of the Neumann-Kelvin problem satisfies the linearized free-surface conditions on the calm-water plane and the body boundary condition on the mean position of the body. The solution to this problem has been investigated by many researchers. Baar and Price (1988), Wang et al. (1996), Noblesse (1983), and many others give various methods for predicting total resistance using the Neumann-Kelvin model. Chen and Noblesse (1983) survey eleven different methods applied to the Wigley hull and compare the numerical predictions to experiments. They find that, on average, the various methods give acceptable results despite significant scatter in the experimental and theoretical predictions.

With the increase in computational power, CFD simulations have become more widely used as a tool to predict total resistance. For free-surface ship flows, Reynolds-

averaged Navier-Stokes (RANS) methods are preferred. The PARNASSOS package is a finite-difference based code developed by the Marine Research Institute Netherlands specifically for free-surface ship flows (Hoekstra and Eça, 1998). Similar to the methods introduced in this thesis, PARNASSOS uses a boundary-element method to provide improved boundary conditions for the RANS simulation on a reduced computational domain. Unlike the current approach, it appears that the PARNASSOS code does not utilize a two-way interaction between the viscous and inviscid solutions.

Kim et al. (2010) documents the implementation of a state of the art finite-volume based method using OpenFOAM for free-surface flows and shows very acceptable agreement with experiments. Although CFD simulations are able to produce accurate results, they still require a very large amount of computational expense and a high-level of user experience to produce these results.

1.1.1 Decomposition Methods

Decomposition methods were introduced to decrease the computational time of the large domain RANS simulation. Domain decompositions and velocity decompositions have been investigated and implemented with varying degrees of success. In a domain-based decomposition method the fluid domain is divided into regions and different solution techniques are applied to each region. In Campana et al. (1995) a two-way coupling procedure is introduced to free-surface ship flows. The RANS equations are solved on an inner domain and a linearized panel method is employed on the outer domain. There is an overlap section where matching conditions are iterated until convergence between the inner and outer solutions is reached.

Iafrati and Campana (2003) study unsteady wave breaking using the domain decomposition discussed in Campana et al. (1995). In this approach the region of the fluid domain away from the surface is modeled using potential flow and the fluid near the free-surface is solved using the RANS equations with a level set method.

In Chen and Lee (1996) and Chen and Lee (1999) a technique similar to the method of Campana is introduced except that it employs a non-linear velocity potential formulation. The same matching technique is applied and the solutions are found to converge within two or three interactions between the viscous and inviscid solutions.

Guillerm and Alessandrini (2003) use the same approach but employ a free-surface Green function with linearized free-surface conditions to specify the velocity potential in the outer domain. The potential solution is coupled to the RANS solution using a Fourier-Kochin method which allows for the calculation of a velocity potential given a velocity distribution on a boundary. The velocity potential is calculated and used to supply boundary conditions for the RANS solution. This two-way interaction is iterated until a converged solution is found.

In general, approaches that use domain decomposition suffer from sensitivity in the location of the interface as well as the complexity in specifying the compatibility conditions at the interface between the two domains which, if done incorrectly, can result in discontinuities in the velocity and pressure fields.

In the velocity decomposition approach, the velocity vector is generally split into two components. Each component can then be solved for using the most efficient manner with respect to the problem of interest. In Hafez et al. (2006) and Hafez et al. (2007) the velocity vector is also decomposed into an irrotational and solenoidal component. The decomposition is substituted into the two-dimensional Navier-Stokes equations and is used to derive a Poisson equation from the continuity equation with the viscous correction terms acting as source terms. Pressure is then calculated using a modified Bernoulli equation in terms of the potential solution only. The viscous terms are solved for using a traditional RANS approach.

Kendon et al. (2003) also uses a similar decomposition but evaluates the irrotational velocity using a boundary-element method in the frequency domain. The

method is applied to problems with wave-body interactions where diffraction forces, which are modeled well by boundary-element techniques, have a strong influence on the solution. The decomposition is used to modify the Navier-Stokes equations and the modified equations are solved throughout a reduced computational domain. The method is applied to two-dimensional cases and extended to three-dimensions using a strip-theory approach.

The spectral wave explicit Navier-Stokes (SWENSE) method discussed in Luquet et al. (2004) and Ferrant et al. (2008) uses decomposition similar to that of Kendon et al. (2003). A velocity potential-based spectral method is used to model incident waves. A set of modified Navier-Stokes equations is solved to simulate the viscous flow around the body. The incident wave potential is modeled using a non-linear velocity potential formulation and a modified set of RANS equations are used to model the diffracted flow. The SWENSE method has been successfully applied to ship maneuvering and wave-body interaction problems. An advantage of this approach is that the RANS domain does not deform as a result of the body motion.

In Morino (1986), the velocity vector is decomposed into irrotational (curl-free) and solenoidal (divergence-free) components. A vorticity-based method is used to simplify the Navier-Stokes equations to apply them to incompressible flows. The work is theoretical in nature but offers an insight into the novel uses of decomposition methods.

1.1.2 Previous Work at the University of Michigan

The current research is based off of the work in Kim et al. (2005) and Edmund (2012). Similar to the methods above, in Kim et al. (2005) the velocity vector is decomposed into an irrotational (potential) velocity component and a vortical velocity term. The decomposition is substituted into the RANS equations and, after mathematical reduction, the "complementary RANS" equations are derived. This

new set of governing equations is solved throughout the fluid domain. The method was shown to reproduce the accuracy of traditional RANS simulations but did not exhibit a significant computational speed-up. A reduction in domain size was not realized because the potential solution was not adjusted to ensure compatibility with the viscous solution after the initial guess for the potential solution was calculated.

In Edmund et al. (2011), improvements were made to the original work by Kim et al. (2005) by introducing a transpiration velocity term to the body boundary condition which improves the agreement between the inviscid and viscous solutions. The complementary RANS equations were solved using this improved velocity potential and a slight improvement in the solution was realized. This approach, however, was discarded in favor of a simpler approach.

In Edmund (2012), the velocity decomposition is only applied to the body- and far-field-boundary conditions. The far-field boundary of a reduced Navier-Stokes domain is located where the vortical component of velocity is zero and the velocity potential fully describes the flow. In order to achieve this, a non-homogeneous body-boundary condition is derived by applying the velocity decomposition to the body-boundary condition, following Morino (1986). The velocity potential which satisfies this modified body-boundary condition satisfies the Navier-Stokes equations directly outside of the vortical region of the flow. This allows for the Navier-Stokes equations to be solved only in the vortical region. The result of this is an accurate and computationally efficient solution method which is able to solve for the viscous flow around a body in fractions of the time required by a conventional Navier-Stokes approach.

1.2 Research Objectives

The overarching goal of this research track is to continue developing a velocity decomposition approach for free-surface flow problems. The previous research

presented in Edmund (2012) succeeded in developing a velocity decomposition approach for Two-Dimensional (2D) and Three-Dimensional (3D) deeply-submerged, non-lifting problems. The goal of the current research is to extend the capabilities of the method to solve lifting problems and include free-surface effects.

1. Develop the method for use in deeply-submerged, lifting applications
2. Develop the method for to include free-surface effects
3. Combine the lifting approach with the free-surface effects to simulate a fully-submerged body under a free-surface

The remainder of this document will describe the theoretical development, numerical implementation, and application of the velocity decomposition approach to solve lifting and free-surface flows. Chapter 2 begins by describing the problem to be solved. The velocity decomposition is introduced and applied to the Navier-Stokes sub-problem and the viscous potential sub-problem. Chapter 3 discusses the numerical implementation of the Navier-Stokes solver, the calculation of the viscous potential, and the iterative scheme used in the velocity decomposition approach. In Chapter 4, the velocity decomposition approach is applied to deeply-submerged lifting flows. Chapter 5 contains results from the application of velocity decomposition to free-surface problems. Finally, Chapter 6 concludes with some discussion and final remarks.

CHAPTER 2

Mathematical Formulation

The problems of interest in this work are external, deeply-submerged and free-surface flows governed by the steady, incompressible Navier-Stokes equations. In this chapter the Navier-Stokes problem is stated. The problem is then decomposed into two sub-problems using the velocity decomposition. The Navier-Stokes sub-problem is described first, followed by the statement of the viscous potential sub-problem. Finally, the approach used to solve for the viscous potential for lifting and free-surface problems is described.

2.1 Problem Statement

The types of flows of interest in this research are flows which satisfy the Navier-Stokes problem. In this work, the Navier-Stokes problem is defined as the Navier-Stokes equations applied to a fluid domain with appropriate boundary conditions. The problem is restricted to steady, incompressible flow. Furthermore, all work presented in this thesis is performed in two-dimensions. The Navier-Stokes equations consist of the conservation of mass and the conservation of linear momentum and are given in Eqs. (2.1) and (2.2). The fluid domain and the boundaries are shown in Fig. 2.1.

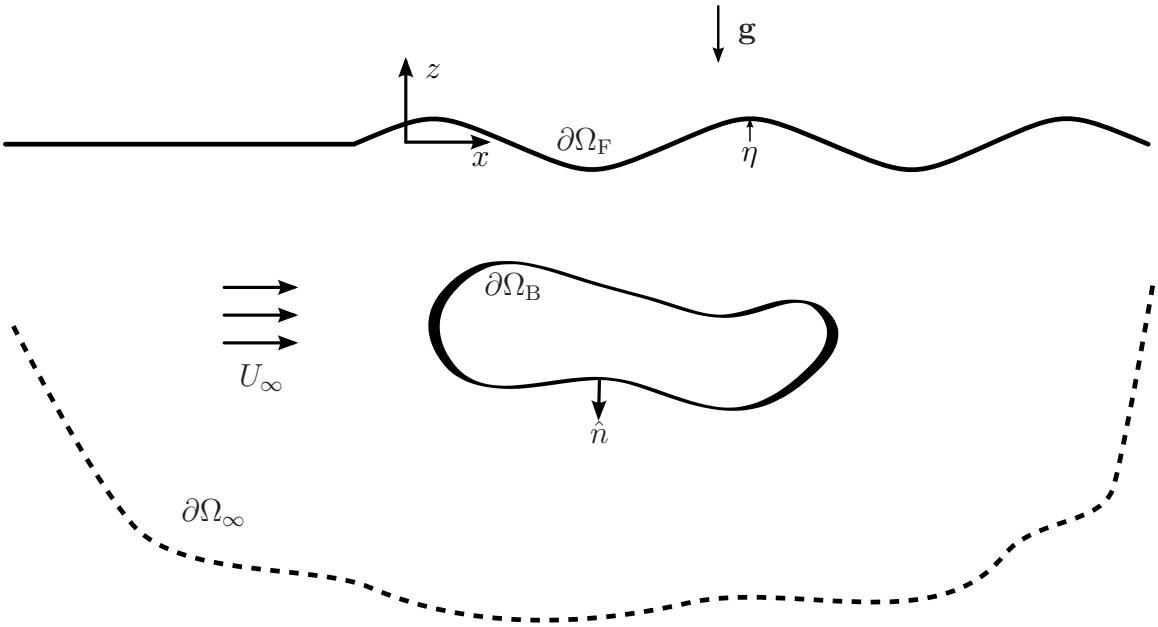

Figure 2.1: The definition of the Navier-Stokes boundary value problem.

$$\nabla \cdot \mathbf{u} = 0 \tag{2.1}$$

$$\nabla \cdot \mathbf{u} \otimes \mathbf{u} = -\nabla p/\rho + \nabla \cdot \nu(\nabla \otimes \mathbf{u} + \nabla \otimes \mathbf{u}^{\mathrm{T}}) - \mathbf{g} \tag{2.2}$$

Where $\mathbf{u}$ is the velocity vector defined in Eq. (2.3), p is the total pressure, $\mathbf{g}$ is the gravity vector representing the body force, ρ is the fluid density, ν is the kinematic viscosity of the fluid, and $()^{\mathrm{T}}$ is the transpose.

$$\mathbf{u} = u\ \hat{i} + w\ \hat{k} \tag{2.3}$$

The form of the momentum equations solved in this work uses a dynamic pressure formulation. The total pressure is expressed as the sum of the dynamic pressure, p_d, and the hydrostatic pressure, $-g\hat{k} \cdot \mathbf{x}$ as shown in Eq. (2.4).

$$p/\rho \equiv p_d/\rho + (-g\hat{k}) \cdot \mathbf{x} \tag{2.4}$$

$$\nabla p/\rho = \nabla p_d/\rho + \nabla(-g\hat{k} \cdot \mathbf{x}) \tag{2.5}$$

$$-\nabla p/\rho = -\nabla p_d/\rho + g\hat{k} \tag{2.6}$$

Eq. (2.6) is substituted into Eq. (2.2) to produce the dynamic pressure formulation of the momentum equations shown in Eq. (2.7).

$$\nabla \cdot \mathbf{u} \otimes \mathbf{u} = -\nabla p_d/\rho + \nabla \cdot \nu(\nabla \otimes \mathbf{u} + \nabla \otimes \mathbf{u}^{\mathrm{T}}) \tag{2.7}$$

When flows of high-Reynolds number (turbulent flows) are of interest, the steady RANS equations are used. A "steady" turbulent flow is characterized by a mean flow field which appears steady with respect to a certain time scale with an unsteady, high-frequency fluctuating component which occurs on a much smaller time scale. The Reynolds-averaging technique is used to deal with this fluctuating component of the flow. To begin to develop the RANS equations, the velocity and pressure variables are expressed as the sum of a mean component denoted with the over-bar and a fluctuating component denoted with a prime symbol as shown in Eqs. (2.8) and (2.9).

$$\mathbf{u} = \overline{\mathbf{u}} + \mathbf{u}' \tag{2.8}$$

$$p_d = \overline{p_d} + p_d{}' \tag{2.9}$$

Eqs. (2.8) and (2.9) are substituted into Eqs. (2.1) and (2.7) and Reynolds-averaging is applied to the resulting equations. Recognizing that the Reynolds-average of a mean value is itself and the Reynolds-average of a fluctuating component is zero, the equations are simplified to get the RANS equations. The RANS equations are

given in Eqs. (2.10) and (2.11).

$$\nabla \cdot \overline{\mathbf{u}} = 0 \tag{2.10}$$

$$\nabla \cdot \overline{\mathbf{u}} \otimes \overline{\mathbf{u}} = -\nabla \overline{p_d}/\rho + \nabla \cdot \left[\nu(\nabla \otimes \overline{\mathbf{u}} + \nabla \otimes \overline{\mathbf{u}}^{\mathrm{T}})\right] - \nabla \cdot \overline{\mathbf{u}' \otimes \mathbf{u}'} \tag{2.11}$$

The resulting Reynolds-averaged equations are nearly identical to the original Navier-Stokes equations with the exception of the final term in the momentum equation involving the mean of the product of the fluctuating component of the velocity vector. This term is referred to as the Reynolds or turbulent stress tensor and represents the loss of momentum due to turbulent fluctuations.

The terms in the Reynolds stress tensor are also additional unknowns which require an equal number of additional governing equations or a closure model. The most common approach to this dilemma is to use the Boussinesq approximation for eddy viscosity. The Boussinesq approximation represents the Reynolds stress tensor in a similar manner as the viscous stress tensor; as the sum of an eddy viscosity term which is proportional to the mean strain rate tensor and the turbulent kinetic energy, as shown in Eq. (2.12).

$$-\overline{\mathbf{u}' \otimes \mathbf{u}'} = \nu_t(\nabla \otimes \overline{\mathbf{u}} + \nabla \otimes \overline{\mathbf{u}}^{\mathrm{T}}) - \frac{2}{3}k\mathbf{I} \tag{2.12}$$

Where ν_t is the turbulent eddy viscosity, k is the turbulent kinetic energy, and $\mathbf{I}$ is the identity matrix. Finally, Eq. (2.12) is substituted in Eq. (2.11) which results in the Reynolds-averaged momentum equation as used in this work as shown in Eq. (2.13), where the overbar denoting the mean component has been removed.

$$\nabla \cdot \mathbf{u} \otimes \mathbf{u} = -\nabla p_d/\rho + \nabla \cdot \left[(\nu + \nu_t)(\nabla \otimes \mathbf{u} + \nabla \otimes \mathbf{u}^{\mathrm{T}})\right] \tag{2.13}$$

The eddy viscosity, ν_t, is an additional unknown and is determined using a tur-

bulence modelling technique, usually involving additional differential equations. The turbulent kinetic energy is absorbed into the dynamic pressure term. The specific turbulence models used in this work will be discussed in Chapter 3.

Throughout the rest of this thesis, it is assumed that the Navier-Stokes equations are used in low Re situations ($\mathrm{Re} \lessapprox 10^4$) while the RANS equations are used in transitional ($10^4 \lessapprox \mathrm{Re} \lessapprox 10^5$) and high Re flows ($10^5 \lessapprox \mathrm{Re}$) with a turbulence model to approximate the eddy viscosity term.

The Navier-Stokes (or RANS) boundary-value problem also requires the specification of boundary conditions in order to be well posed. Eq. (2.14) is the no-slip body boundary condition and is applied to $\partial\Omega_{\mathrm{B}}$, as shown in Fig. 2.1.

$$\mathbf{u} = 0 \qquad \text{on} \qquad \partial\Omega_{\mathrm{B}} \tag{2.14}$$

The free-surface boundary conditions are slightly more complicated because the exact location of the free surface is not immediately known. Therefore, an additional unknown $\eta(x)$, the elevation of the free surface as defined in Eq. (2.15), is introduced. The introduction of an additional unknown also requires an additional boundary condition. The two equations which make up the free-surface boundary conditions are the kinematic and dynamic boundary conditions.

The kinematic free-surface boundary condition requires that the velocity of the free surface is equal to the velocity of the fluid on the free surface. Another way of stating this is that a particle which is located on the free surface, as defined in Eq. (2.15), remains on the free surface. Therefore, the material derivative of Eq. (2.15) must also be zero. Eq. (2.16) is the steady non-linear kinematic free-surface boundary condition.

$$f(x,z) = z - \eta(x) = 0 \qquad \text{on} \qquad \partial\Omega_{\mathrm{F}} \tag{2.15}$$

$$\frac{D}{Dt}(z-\eta) = 0$$

$$\frac{\partial}{\partial t}(z-\eta) + \mathbf{u}\cdot\nabla(z-\eta) = 0 \quad (\partial/\partial t \to 0)$$

$$\mathbf{u}\cdot\nabla(z-\eta) = 0 \qquad \text{on} \qquad \partial\Omega_{\mathrm{F}} \tag{2.16}$$

A free surface is, by definition, a surface which has zero stress. If the pressure exerted on the free surface from the air is zero, then the dynamic free-surface boundary condition for the case of zero stress is stated in Eq. (2.18).

$$\bar{\bar{\sigma}}\cdot\hat{n} = \mathbf{0} \tag{2.17}$$

$$\left[-p\,\mathbf{I} + \mu(\nabla\otimes\mathbf{u} + \nabla\otimes\mathbf{u}^{\mathrm{T}})\right]\cdot\hat{n} = \mathbf{0} \qquad \text{on} \qquad \partial\Omega_{\mathrm{F}} \tag{2.18}$$

For deeply-submerged problems, the velocity is required to return to the free-stream value at the far-field boundary, $\partial\Omega_{\infty}$. Eq. (2.19) is the far-field condition in problems where the body is deeply-submerged and the free-surface, $\partial\Omega_{\mathrm{F}}$, is not present.

$$\lim_{|\mathbf{x}|\to\infty} \mathbf{u} = U_{\infty}\,\hat{i} \tag{2.19}$$

For free-surface problems, the radiation condition is stated in two parts. A condition on the free-surface waves must be imposed so that no waves travel upstream of the disturbance. This is known as the free-surface radiation condition. The specific formulation of the free-surface radiation condition is discussed in Section 2.4. The second part of the radiation condition states that the velocity return to the free-

stream value as the distance from the free surface in the $\hat{k}$-direction grows. Eqs. (2.20) and (2.21) and the free-surface radiation condition constitute the far-field boundary conditions in free-surface problems.

$$\lim_{x \to -\infty} \mathbf{u} = U_\infty \, \hat{i} \tag{2.20}$$

$$\lim_{z \to -\infty} \mathbf{u} = U_\infty \, \hat{i} \tag{2.21}$$

The correct boundary conditions for the pressure field in Navier-Stokes problems are still the subject of discussion and debate in the literature (Gresho and Sani, 1987; Nordström et al., 2007; Rempfer, 2006, 2008; Sani et al., 2006). Boundary conditions for pressure and eddy viscosity are discussed in Section 3.1 because they are treated as part of the numerical approach.

2.2 Velocity Decomposition

Now that the Navier-Stokes boundary-value problem has been defined, the velocity decomposition approach used to solve it can be described. The decomposition of the velocity vector is based on the fundamental theorem of vector calculus which states that any vector field can be expressed as the sum of an irrotational (curl-free) field and solenoidal (divergence-free) field (Arfken and Weber, 2005). Eq. (2.22) defines the velocity decomposition used in this work.

$$\mathbf{u} = \nabla \Phi + \mathbf{w} \tag{2.22}$$

Where the irrotational component of the velocity decomposition is represented as the gradient of a scalar, Φ, and the solenoidal component is $\mathbf{w}$ is also referred to as the vortical component.

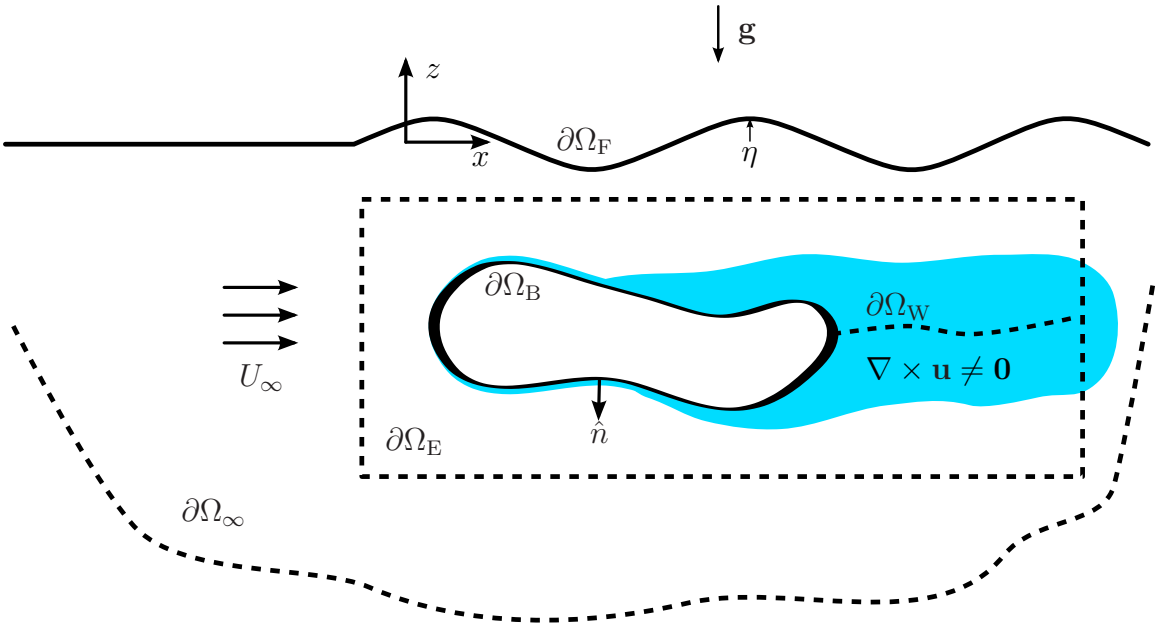

Figure 2.2: A description of the velocity decomposition approach.

As stated in Chapter 1, the strategy driving the use of velocity decomposition for Navier-Stokes problems is to reduce the size of the flow domain over which a Navier-Stokes solver must be used by representing the majority of the flow field with a velocity potential. The velocity potential is then used to supply boundary conditions to the Navier-Stokes solver. This is illustrated in Fig. 2.2 and Eq. (2.23), where $\partial\Omega_E$ is the boundary of the reduced Navier-Stokes domain.

$$\mathbf{u} = \nabla\Phi \qquad \text{on} \qquad \partial\Omega_E \tag{2.23}$$

The decomposition stated in Eq. (2.22) is not unique; there are an infinite number of combinations of vector fields which could combine to re-create the total velocity field. Therefore, a condition is enforced on the decomposition to require the vortical component, $\mathbf{w}$, to go to zero outside of the vortical region of the flow. To put it another way, as the distance from the body grows, the vortical component in the velocity decomposition goes to zero. Once the vortical component is negligible, the total velocity vector can be represented in full by the velocity potential. It is therefore

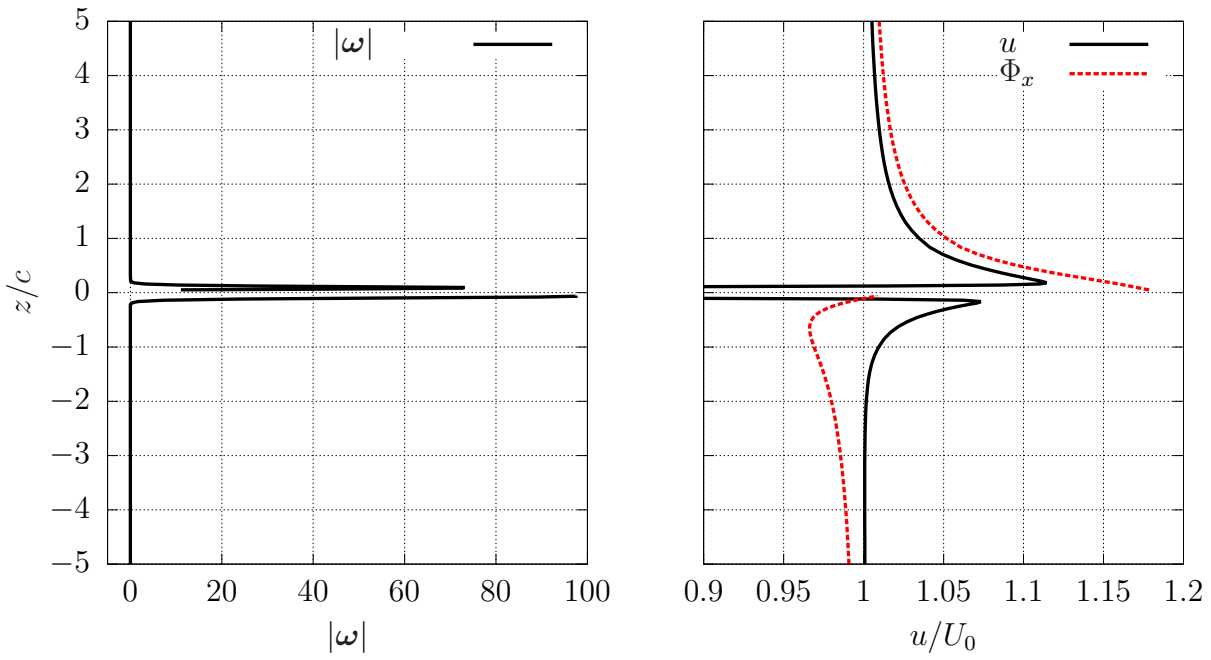

(a) Magnitude of vorticity at the midchord.

(b) Streamwise velocity at the midchord.

Figure 2.3: Vorticity and streamwise velocity over a sample line at the midchord of the NACA0012 foil at Re $= 2000$.

essential to use a velocity potential which satisfies the Navier-Stokes problem directly outside of the vortical regions of the flow. Unfortunately, the velocity potential which satisfies the conventional inviscid boundary conditions on the body - non-penetration and, if applicable, smooth flow at the trailing edge - does not satisfy this requirement. This is very clearly shown in Fig. 2.3 where the streamwise component of the velocity potential is compared to the streamwise component of the viscous flow over a NACA0012 foil at Re $= 2000$ at an angle of attack, $\alpha = 5°$. In fact, the velocity potential does not satisfy the Navier-Stokes problem even at large distances from the body. Additionally, the lift coefficient determined from the velocity potential does not capture the loss of lift due to separation and stall present in the viscous solution.

Therefore, a different velocity potential, the *viscous* potential, must be used. The viscous potential is a velocity potential which satisfies the Navier-Stokes problem directly outside of the vortical region of the flow. In the current approach, the viscous

potential is represented as φ and satisfies a modified body-boundary condition. Conversely, the *inviscid* potential, represented as Φ, is the velocity potential which satisfies the conventional non-penetration body-boundary condition. Eqs. (2.24), (2.25), and (2.26) form the basis of the velocity decomposition using the viscous potential.

$$\mathbf{u} = \nabla\varphi + \mathbf{w} \tag{2.24}$$

$$\mathbf{u} = \nabla\varphi \qquad \text{on} \qquad \partial\Omega_{\mathrm{E}} \tag{2.25}$$

$$\frac{\partial\varphi}{\partial n} = f(\mathbf{u}) \qquad \text{on} \qquad \partial\Omega_{\mathrm{B}} \tag{2.26}$$

The use of the viscous potential was first developed and implemented in Edmund (2012) for 2D and 3D, steady, non-lifting, deeply-submerged problems. Fig. 2.4 shows the streamlines of the viscous potential (black) and viscous flow (grey) around a circular cylinder at $\mathrm{Re} = 200$ overlaid on top of contours of velocity (top) and vorticity (bottom). Clearly, the streamlines of the viscous potential match the viscous flow outside of the vortical region of the flow; whereas the agreement between the inviscid potential and the Navier-Stokes flow would be poor, even outside of the rotational region.

Now that the general velocity decomposition approach has been introduced, the Navier-Stokes problem described in Section 2.1 will be decomposed into the Navier-Stokes sub-problem (Section 2.3) and the viscous potential sub-problem (Section 2.4).

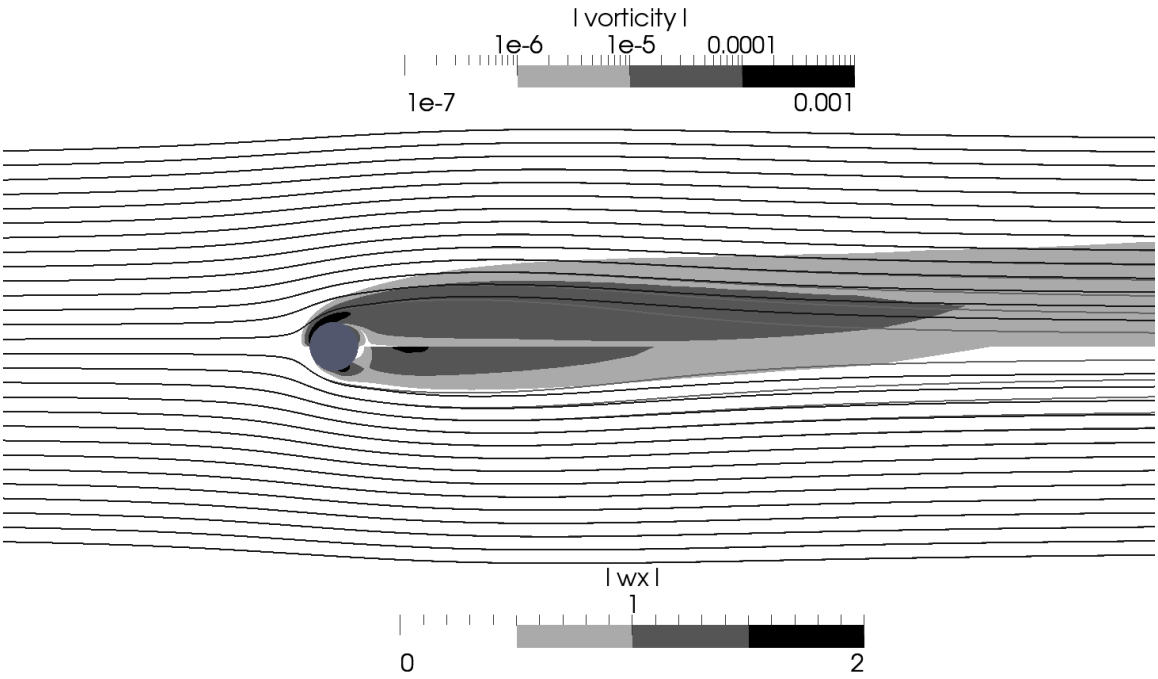

Figure 2.4: Streamlines for the viscous flow (grey) and the viscous potential (black) over a circular cylinder at $\mathrm{Re} = 200$ with contours of vorticity (top) and contours of $|\mathbf{w} \cdot \hat{i}| = |u - \varphi_x|$ (bottom).

2.3 Navier-Stokes Sub-Problem

The Navier-Stokes sub-problem is simply defined as the Navier-Stokes equations with the velocity decomposition expression, Eqs. (2.1), (2.7), and (2.24), on a reduced domain. The boundary-value problem for the Navier-Stokes sub-problem is described in Fig. 2.5.

$$\nabla \cdot \mathbf{u} = 0 \tag{2.1}$$

$$\nabla \cdot \mathbf{u} \otimes \mathbf{u} = -\nabla p/\rho + \nabla \cdot \nu(\nabla \otimes \mathbf{u} + \nabla \otimes \mathbf{u}^{\mathrm{T}}) \tag{2.7}$$

$$\mathbf{u} = \nabla\varphi + \mathbf{w} \tag{2.24}$$

The no-slip body boundary condition is still enforced. The important difference between the Navier-Stokes problem and the Navier-Stokes sub-problem is that the

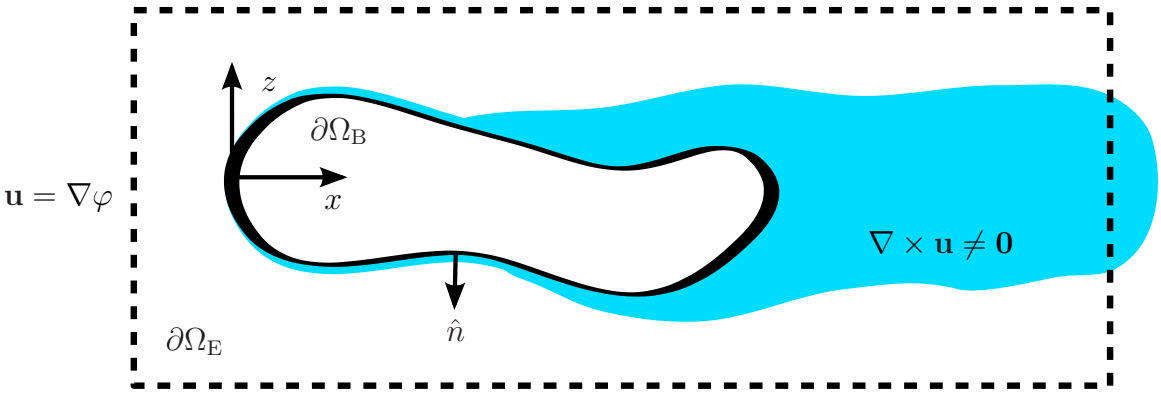

Figure 2.5: The boundary value problem for the Navier-Stokes sub-problem.

domain of the sub-problem is drastically reduced to only include the region of the flow which is vortical. The boundary condition on the boundary of the reduced domain, $\partial\Omega_E$, is given in Eq. (2.27).

$$\mathbf{u} = \nabla\varphi \qquad \text{on} \qquad \partial\Omega_E \tag{2.27}$$

Again, pressure boundary conditions are included as part of the numerical approach and discussed in Section 3.1.

The governing equations which describe the Navier-Stokes sub-problem are coupled to each other, contain nonlinear terms, and the boundary conditions are dependent on the viscous potential. Since there are very few analytical solutions to the Navier-Stokes problem , the Navier-Stokes sub-problem are generally solved numerically. The numerical algorithm which is used to solve the Navier-Stokes sub-problem is also described in the next chapter.

2.4 Viscous Potential Sub-Problem

The irrotational component of the velocity decomposition is represented using a velocity potential. If the flow field is irrotational, then the fundamental theorem of vector calculus states that the velocity field can be represented by the gradient of a

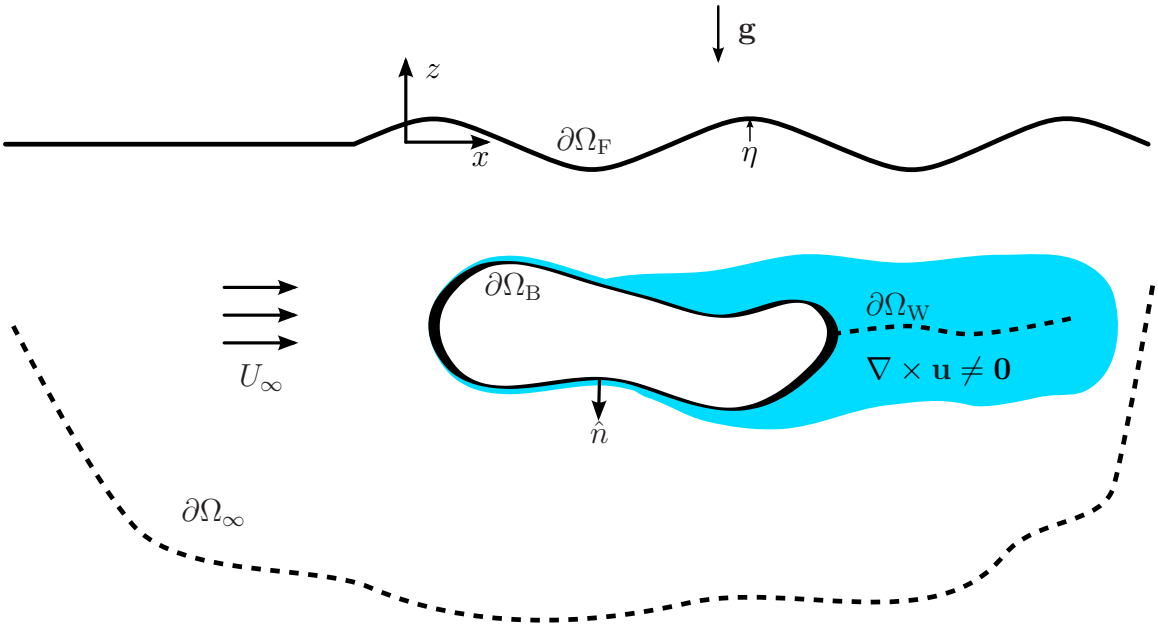

Figure 2.6: The boundary-value problem for the viscous potential sub-problem.

scalar field, Eq. (2.28) (Arfken and Weber, 2005). Additionally, in order to ensure that the flow field remains irrotational, Kelvin's theorem requires that the flow must also be inviscid.

$$\mathbf{u} = \nabla\varphi \tag{2.28}$$

Then, Eq. (2.28) is substituted into the continuity equation, Eq. (2.1), which results Laplace's equation (Eq. (2.29)), the governing equation for the velocity potential. Eqs. (2.29) and (2.24) are the governing equations for the viscous potential sub-problem. Fig. 2.6 shows the definition of the boundary-value problem for the viscous potential.

$$\nabla^2\varphi = 0 \tag{2.29}$$

$$\mathbf{u} = \nabla\varphi + \mathbf{w} \tag{2.24}$$

The governing Laplace equation for the viscous potential is solved using the conventional boundary-element method widely discussed in the literature (Katz and Plotkin (1991), for example). Green's identities are used to express the velocity potential as a surface distribution of singularities which are also fundamental solutions to Laplace's equation. The singularities are known as sources and dipoles. Therefore, the velocity potential is represented by distributions of sources and dipoles on the boundaries of the problem as shown in Eq. (2.30).

$$\varphi = \int_{\partial\Omega_{\mathrm{B}}+\partial\Omega_{\mathrm{F}}+\partial\Omega_{W}} \ln r \; \sigma + \frac{\partial}{\partial n} (\ln r) \, \mu \; \mathrm{dS} + U_{\infty} x \tag{2.30}$$

Where σ and μ are the unknown strengths of the source and dipole distributions and the boundaries are defined in Fig. 2.6. The strengths of the singularities are determined by applying boundary conditions. However, there are twice as many unknowns as there are boundaries (and boundary conditions). Therefore, additional constraints or assumptions must be stated in order to make the problem solvable. For example, some solution techniques assume that the strength of the source distribution is a known quantity and solve for the dipole strength while other approaches will set $\mu = 0$ on the body, effectively removing the dipole distribution from the body. The boundary-element method is very flexible as long as fundamental solutions are distributed over all surfaces and that the number of unknowns is equal to the number points at which the boundary conditions are satisfied. In this work, the velocity potential is represented by a source and vortex (another fundamental solution) distribution on the body, a source and dipole distribution on the wake surface, and a source distribution on the free surface.

In order to complete the viscous potential sub-problem, the boundary conditions for the viscous potential are now stated. Following Edmund (2012), the body-boundary condition for the viscous potential is developed from the no-slip boundary

condition, Eq. (2.14).

$$\begin{aligned} \mathbf{u} &= 0 \qquad \text{on} \qquad \partial\Omega_{\mathrm{B}} \\ &= \nabla\varphi + \mathbf{w} \end{aligned} \tag{2.14}$$

or

$$\nabla\varphi = -\mathbf{w} \qquad \text{on} \qquad \partial\Omega_{\mathrm{B}} \tag{2.31}$$

Both sides of Eq. (2.31) are then dotted with the surface normal vector, $\hat{n}$, to obtain a Neumann condition for the viscous potential, Eq. (2.32). The body-boundary condition for the viscous potential in Eq. (2.32) is written in terms of the vortical component of the velocity decomposition and, therefore, contains information about the viscous flow. The body-boundary condition for the viscous potential will be further developed in Section 2.4.1.

$$\frac{\partial\varphi}{\partial n} = -\mathbf{w}\cdot\hat{n} \qquad \text{on} \qquad \partial\Omega_{\mathrm{B}} \tag{2.32}$$

In many flows of interest in this research, a large portion of the rotational flow exists in the region immediately downstream of the body in the viscous wake. It was found by Edmund (2012) that it is essential to include a wake surface downstream of the body in order to incorporate these effects. The body-boundary condition for the viscous potential is also applied to the wake surface as shown in Eq. (2.33).

$$\frac{\partial\varphi}{\partial n} = -\mathbf{w}\cdot\hat{n} \qquad \text{on} \qquad \partial\Omega_{\mathrm{W}} \tag{2.33}$$

The free-surface boundary conditions are developed by applying the assumption of inviscid flow to the viscous free-surface boundary conditions; by doing this, the effects of viscosity at the free-surface are neglected. Removing the viscous term from

the dynamic free-surface boundary condition, Eq. (2.18), results in Eq. (2.34).

$$p = 0 \qquad \text{on} \qquad \partial\Omega_{\mathrm{F}} \tag{2.34}$$

Then, Bernoulli's equation is used to relate the pressure on the free surface to the fluid velocity and free-surface elevation. The inviscid non-linear dynamic free-surface boundary condition in terms of the velocity potential and free-surface elevation is given in Eq. (2.35).

$$\eta = -\frac{1}{g}\left(\phi_x U_\infty + \frac{1}{2}\nabla\phi\cdot\nabla\phi\right) \qquad \text{on} \qquad \partial\Omega_{\mathrm{F}} \tag{2.35}$$

Where ϕ is the perturbation of the viscous potential from the free stream potential as defined in Eq. (2.36).

$$\varphi \equiv \phi + U_\infty x \tag{2.36}$$

Eq. (2.35) is linearized by assuming that $U_\infty \gg |\nabla\phi|$ and applied to the mean free surface. The result is the linearized dynamic free-surface boundary condition, Eq. (2.37).

$$\eta = -\frac{U_\infty}{g}\phi_x \qquad \text{on} \qquad z = 0 \tag{2.37}$$

The inviscid nonlinear kinematic free-surface boundary condition in Eq. (2.38) is nearly equivalent to the viscous nonlinear kinematic free-surface boundary condition in Eq. (2.16).

$$\nabla\varphi\cdot\nabla(z-\eta) = 0 \qquad \text{on} \qquad \partial\Omega_{\mathrm{F}} \tag{2.38}$$

Eq. (2.38) is expanded in Eq. (2.39).

$$\phi_z = U_\infty \eta_x + \phi_x \eta_x \qquad \text{on} \qquad \partial\Omega_F \tag{2.39}$$

Eq. (2.39) is linearized by applying a Taylor series expansion about $z = 0$ and discarding the higher-order terms. Eq. (2.40) is the inviscid linearized kinematic free-surface boundary condition.

$$\phi_z = U_\infty \eta_x \qquad \text{on} \qquad z = 0 \tag{2.40}$$

The combined linearized free surface condition in Eq. (2.41) is developed by taking the partial derivative with respect to x of Eq. (2.37) and substituting it into Eq. (2.40). This is the free-surface boundary condition used in the current method. After the singularity strengths are determined, the free-surface elevation is calculated using the linearized dynamic free-surface boundary condition, Eq. (2.37).

$$\phi_{xx} + \frac{g}{{U_\infty}^2}\phi_z = 0 \qquad \text{on} \qquad z = 0 \tag{2.41}$$

The free-surface radiation condition requires that all waves generated by the body flow downstream. In some free surface solution methods the radiation condition is enforced by using an upstream finite-difference operator to calculate the velocity potential derivatives on the free surface which automatically satisfies the radiation condition (Dawson, 1977). Others sometimes shift the upstream collocation points with respect to the source locations (Raven, 1989). Since the approach used in this work uses analytic expressions for the velocity potential derivatives in the free-surface condition, an additional condition must be included. Following Scullen (1998), this is accomplished by requiring that the vertical component of velocity is equal to zero at two points sufficiently far upstream from the body.

$$\phi_z(x = x_1, z = 0) = 0$$
$$\phi_z(x = x_2, z = 0) = 0 \tag{2.42}$$

Where x_1 and x_2 are located far upstream of the body, usually at a distance of at least three fundamental wavelengths. The distance between the two points must not be equal to an integer multiple of half of the fundamental wavelength because this would allow waves to exist upstream with nodes located at the two points.

$$|x_1 - x_2| \neq n\frac{\lambda_0}{2} \tag{2.43}$$

Where $\lambda_0 = 2\pi {U_\infty}^2/g$ is fundamental wavelength predicted by linear theory.

The far-field radiation condition for the viscous potential is found by applying the velocity decomposition expression, Eq. (2.24), to the far-field boundary condition for the Navier-Stokes problem. The vortical velocity goes to zero in the far field and the viscous potential fully describes the velocity field. Eq. (2.44) is the far-field radiation condition for deeply-submerged problems while Eqs. (2.45) and (2.46) state the far-field radiation condition for free-surface problems.

$$\mathbf{u} = \nabla\varphi + \mathbf{w} \tag{2.24}$$
$$\lim_{|\mathbf{x}|\to\infty} \nabla\varphi = U_\infty \hat{i} \tag{2.44}$$
$$\lim_{x\to-\infty} \nabla\varphi = U_\infty \hat{i} \tag{2.45}$$
$$\lim_{z\to-\infty} \nabla\varphi = U_\infty \hat{i} \tag{2.46}$$

The far-field boundary conditions are automatically satisfied due to the nature of the singularities which are distributed on the body boundary and on the free surface.

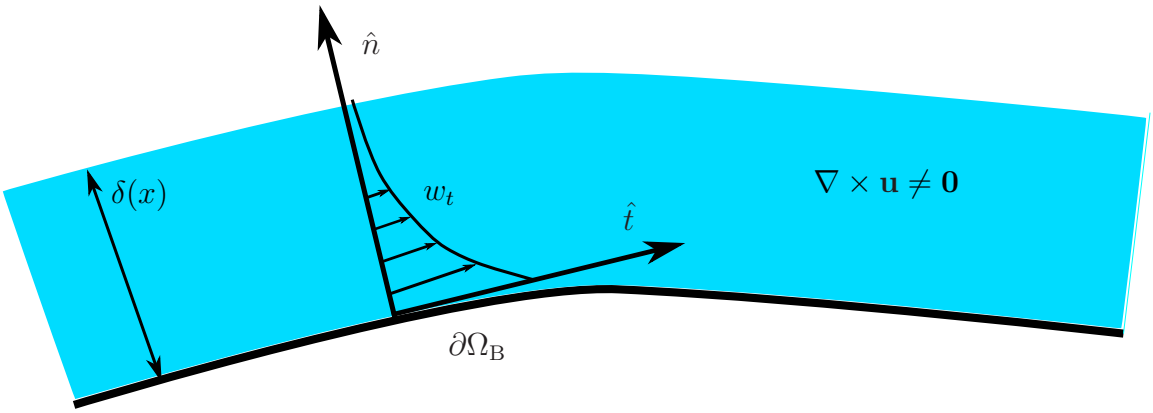

Figure 2.7: A figure describing the local-orthogonal coordinate system and the δ-boundary.

2.4.1 Body Boundary Condition for the Viscous Potential

The body-boundary condition for the viscous flow is motivated from Morino et al. (1999) and directly follows Edmund (2012), and is reproduced here for completeness. To begin, the velocity decomposition expression is substituted into the continuity equation, Eq. (2.1), resulting in the requirement that the vortical velocity is also divergence-free, Eq. (2.47).

$$\nabla \cdot \mathbf{u} = 0 \tag{2.1}$$

$$\nabla \cdot (\nabla\varphi + \mathbf{w}) = 0$$

$$\cancelto{0}{\nabla^2\varphi} + \nabla \cdot \mathbf{w} = 0$$

$$\nabla \cdot \mathbf{w} = 0 \tag{2.47}$$

Then, the vortical velocity and gradient operator are expressed in a local-orthogonal coordinate system as shown in Eqs. (2.48) and (2.49) and Fig. 2.7.

$$\mathbf{w} = w_n\hat{n} + w_t\hat{t} \tag{2.48}$$

$$\nabla = \frac{\partial}{\partial n}\hat{n} + \frac{\partial}{\partial t}\hat{t} \tag{2.49}$$

Eq. (2.47) is also written in the local-orthogonal coordinate system.

$$\frac{\partial w_n}{\partial n} + \frac{\partial w_t}{\partial t} = 0 \tag{2.50}$$

Eq. (2.50) is then integrated along the local normal vector out to a distance δ which is defined as the edge of the vortical region. The integral for the normal component of the vortical velocity is directly evaluated. The result is an expression for the normal component of the vortical velocity on the body, Eq. (2.51).

$$\begin{aligned}
\frac{\partial w_n}{\partial n} &= -\frac{\partial w_t}{\partial t} \\
\int_0^\delta \frac{\partial w_n}{\partial n}\ \mathrm{dn} &= -\int_0^\delta \frac{\partial w_t}{\partial t}\mathrm{dn} \\
w_n(\delta) - w_n(0) &= -\int_0^\delta \frac{\partial w_t}{\partial t}\ \mathrm{dn} \\
w_n(0) &= \int_0^\delta \frac{\partial w_t}{\partial t}\ \mathrm{dn} + w_n(\delta)
\end{aligned} \tag{2.51}$$

Then, Eq. (2.32) is used to obtain the Neumann condition for the viscous potential on the body by applying the requirement that the vortical velocity go to zero outside of the vortical region.

$$\frac{\partial \varphi}{\partial n} = -\mathbf{w} \cdot \hat{n} \qquad \text{on} \qquad \partial\Omega_{\mathrm{B}} \tag{2.32}$$

$$= -w_n(0)$$

$$= -\int_0^{\delta} \frac{\partial w_t}{\partial t}\, \mathrm{dn} - \cancelto{0}{w_n(\delta)}$$

$$\frac{\partial \varphi}{\partial n} = -\int_0^{\delta} \frac{\partial w_t}{\partial t}\, \mathrm{dn} \qquad \text{on} \qquad \partial\Omega_{\mathrm{B}} \tag{2.52}$$

The body-boundary condition for the viscous potential is not the conventional non-penetration condition. In fact, it requires that a normal flow exist through the body surface. The effect of the body-boundary condition for the viscous potential is to alter the shape of the body based on the thickness of the boundary layer and other viscous effects, such as separation. It is important to note that this approach has similarities to the equivalent source technique from Lighthill (1958). While there is some likeness in the approach, Lighthill's formulation makes the assumption that the boundary layer is fully attached, thin, and two-dimensional. On the other hand, the approach used in this work is valid for cases where the boundary layer is very thick and massively separated (as in the case of the circular cylinder at $\mathrm{Re} = 200$) and is directly applicable to three-dimensional situations as demonstrated in Edmund (2012).

2.4.2 Circulation Condition for the Viscous Potential

While motivating the need for the development of the viscous potential, an allusion was made to the need to modify Kutta condition applied at the sharp trailing edge in lifting flows. In potential flow, the Kutta condition is used to ensure that a stagnation point exist at the trailing edge of a foil. When the Kutta condition is satisfied, the

velocity field is smooth as it leaves the trailing edge. The Kutta condition can be stated in various ways; requiring that the velocity field be smooth as it leaves the trailing edge, requiring that a stagnation point be located at the trailing edge, or alternatively requiring zero pressure difference across a wake surface emanating from the trailing edge. Essentially, the Kutta condition is an additional physical constraint on the velocity potential which is used to determine the value of the body-bound circulation.

In this work, the equal pressure Kutta condition is used for the calculation of the inviscid potential. Eq. (2.53) is the result of using Bernoulli's equation to equate the pressure at two points where the small change in hydrostatic pressure is neglected. The two points are located just behind the trailing edge, slightly above and below the wake surface.

$$\nabla\varphi^+ \cdot \nabla\varphi^+ - \nabla\varphi^- \cdot \nabla\varphi^- = 0 \tag{2.53}$$

However, the issue with using a Kutta condition in the velocity decomposition framework is that it does not account for the loss of lift due to separation which is purely a viscous effect. Preliminary velocity decomposition calculations in Rosemurgy et al. (2013) found that the lift coefficient was greatly over predicted when compared to the lift predicted by a Navier-Stokes solver. This was due to the fact that the viscous potential satisfied the inviscid Kutta condition, which resulted in a body-bound circulation that corresponded to a lift coefficient nearly twice the value of the lift coefficient predicted by a Navier-Stokes solver.

The solution to the problem of over-prediction of lift is to use the Kutta-Joukowski theorem, Eq. (2.54), to relate the lift on the body calculated in the Navier-Stokes sub-problem to the total body-bound circulation in the viscous potential sub-problem.

$$\mathcal{L} = \rho U_\infty \Gamma \tag{2.54}$$

The force on the body in the Navier-Stokes sub-problem is calculated as the integral of the stress on the body as shown in Eq. (2.55). The lift is the component of the force in the $\hat{k}$ direction, Eq. (2.56).

$$\mathcal{F} = \int_{\partial\Omega_{\mathrm{B}}} \left[p_d \, \mathbf{I} - \mu(\nabla \otimes \mathbf{u} + \nabla \otimes \mathbf{u}^{\mathrm{T}}) \right] \cdot \hat{n} \; \mathrm{dS} \tag{2.55}$$

$$\mathcal{L}^{NS} = \mathcal{F} \cdot \hat{k} \tag{2.56}$$

Once the lift from the Navier-Stokes sub-problem is calculated, the circulation required to generate this lift is found by re-arranging the Kutta-Joukowski theorem, Eq. (2.57).

$$\Gamma^{NS} = \frac{\mathcal{L}^{NS}}{\rho U_\infty} \tag{2.57}$$

Finally, Eq. (2.58) is the total circulation condition which is used in place of the Kutta condition to determine the magnitude of the body-bound circulation in the viscous potential.

$$\int_{\partial\Omega_{\mathrm{B}}} \gamma \; \mathrm{dS} = \Gamma^{NS} \tag{2.58}$$

CHAPTER 3

Numerical Implementation

In this chapter the numerical implementation of the velocity decomposition approach described in Chapter 2 are described. First, the solution methodology for the Navier-Stokes sub-problem and viscous potential sub-problem will be described. Then, the iterative solution strategy implemented to solve the full Navier-Stokes problem using velocity decomposition will be described.

3.1 Navier-Stokes Sub-Problem

The Navier-Stokes equations are solved using the open-source CFD library, OpenFOAM (Weller et al., 1998). OpenFOAM has the capability to numerically solve coupled, non-linear differential equations in both space and time on arbitrary polygonal 2D and 3D meshes. In this work, OpenFOAM is primarily used to solve the steady, 2D Navier-Stokes equations.

The steady, 2D Navier-Stokes equations are a set of three coupled, non-linear differential equations. In OpenFOAM , the finite-volume method is used to discretize the flow field and transform the differential equations into a set of linear systems of equations. An iterative scheme must be employed in order to solve such a complex system of equations. The SIMPLE algorithm (Patankar, 1980) is used to iteratively solve the coupled pressure-velocity system. The SIMPLE algorithm is briefly described below.

1. Calculate the matrix coefficients using the finite-volume method to form the linear systems for each momentum equation
2. Solve for each component of velocity by solving the linear system derived from the discretized momentum equation
3. Calculate the velocity and pressure terms to assemble the pressure correction equation
4. Solve the pressure correction equation to enforce the continuity equation
5. Correct the velocity and pressure fields based on the solution of the pressure correction equation
6. Repeat until convergence.

Before each linear system is solved, the initial residual of the system is calculated. The residual of a linear system is a representation of the error in the current solution. A linear matrix solver then iterates on the linear system until the residual of the system drops below a specified threshold, or drops by a value relative to the initial residual. The convergence of the Navier-Stokes equations is generally determined by monitoring the initial residuals of the momentum and pressure equations.

It is a conventional approach in finite-volume CFD to use a Neumann boundary condition for pressure on all but one boundary where a Dirichlet condition is used to set the reference pressure. Generally, the Dirichlet condition for pressure is applied to the outlet boundary as shown in Eq. (3.1), and the Neumann condition in Eq. (3.2) is used on the inlet boundaries.

$$p_d = 0 \qquad \text{on} \qquad \partial\Omega_{\mathrm{O}} \tag{3.1}$$

$$\frac{\partial p_d}{\partial n} = 0 \qquad \text{on} \qquad \partial\Omega_{\mathrm{E}} \tag{3.2}$$

However, the zero normal derivative condition is not correct when smaller domain sizes are used. In this case, the Neumann condition for the pressure field is calculated by using Bernoulli's equation to relate the pressure and viscous potential. A two-point finite difference is used to calculate the derivative in the direction normal to the boundary as shown in Eq. (3.3).

$$\frac{\partial p_d}{\partial n}(\mathbf{x}_f) = \frac{\rho}{2}\frac{|\nabla\Phi(\mathbf{x}_f)|^2 - |\nabla\Phi(\mathbf{x}_f - \sqrt{A_f}\cdot\hat{n})|^2}{\sqrt{A_f}} \qquad \text{on} \qquad \partial\Omega_{\mathrm{E}} \tag{3.3}$$

Where $\mathbf{x}_f$ is the center of a face on the boundary, A_f is the area of the face, and the normal vector follows the OpenFOAM convention and points outside of the computational domain.

In high-Reynolds number (Re) cases where the RANS equations are applicable, a turbulence model is needed to approximate the eddy viscosity, ν_t. In all of the cases presented in this research, the one-equation Spalart-Allmaras turbulence model (Spalart and Allmaras, 1992) is used. A wall function is used to approximate the behavior of the turbulent stress on the body; the turbulent stress is then used to calculate the value of the eddy viscosity on the body. The inlet boundary condition for the eddy viscosity is given in Eq. (3.4). This is slightly higher than recommended in Spalart and Allmaras (1992), but is useful in order to stabilize the high Re simulations so that a steady solution is obtained.

$$\nu_t = 10\cdot\nu \qquad \text{on} \qquad \partial\Omega_I \tag{3.4}$$

$$\frac{\partial \nu_t}{\partial n} = 0 \qquad \text{on} \qquad \partial\Omega_{\mathrm{O}} \tag{3.5}$$

3.2 Viscous Potential Sub-Problem

The numerical implementation of the viscous potential is very similar to the conventional boundary-element method used to solve most velocity potential problems. However, there are a few important modifications that need to be highlighted. As discussed in Section 2.4, the solution to the Laplace equation for the velocity potential can be found by distributing singularities of unknown strength on the boundaries of the fluid domain. The strengths of these singularities are determined by applying the boundary conditions and making assumptions about the nature of the flow.

The total viscous potential is composed of five singularity distributions as well as the freestream potential as shown in Eq. (3.6).

$$\varphi = \phi_V + \phi_{BS} + \phi_{WS} + \phi_D + \phi_{FS} + U_\infty x \tag{3.6}$$

Where ϕ_V is the vortex distribution on the body, ϕ_{BS} is the source distribution on the body, ϕ_{WS} is the source distribution on the wake surface, ϕ_D is the dipole distribution on the wake surface, and ϕ_{FS} is the source distribution on the free surface. The reason for this mix of singularity distributions is discussed below.

The body is discretized with flat panels corresponding to the finite-volume discretization from the viscous flow solver. The vortex distribution on the body is represented using panels of linearly varying strength while the source distribution is represented using constant strength panels. The wake surface is either placed on a straight line originating at the trailing edge and parallel to the $x-$axis or upon a streamline beginning at the trailing edge. On the wake surface, the source and dipole panels are constant strength, flat, and coincidentally located. The free-surface source distribution is represented using point sources raised above the mean free surface (Cao et al., 1991).

The body-boundary condition for the viscous potential is applied to the body

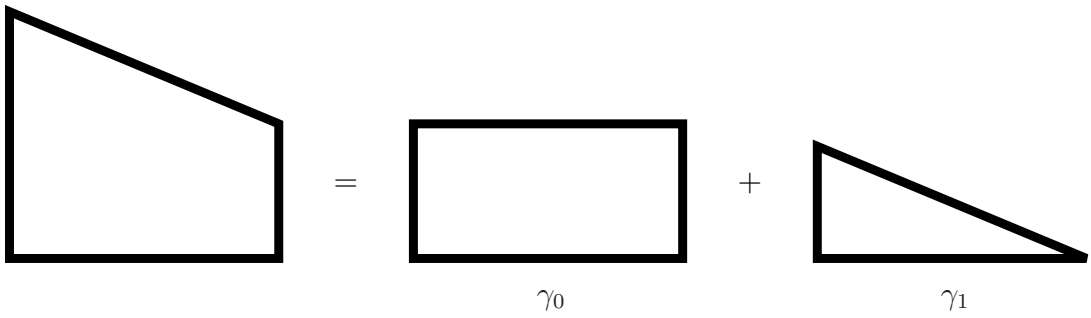

Figure 3.1: The linearly varying strength vortex panel is the sum of a constant strength (γ_0) and linearly varying strength (γ_1).

surface as shown in Eq. (3.7), where χ represents the integral term in Eq. (2.52) and will be further developed later. However, the body-boundary condition is split into two parts. The linear vortex panels satisfy the inviscid lifting problem, Eq. (3.8), while the source panels account for the effects of viscosity, Eq. (3.9).

$$\frac{\partial \varphi}{\partial n} = -\int_0^{\delta} \frac{\partial w_t}{\partial t}\,\mathrm{dn} \qquad \text{on} \quad \partial\Omega_\mathrm{B} \tag{2.52}$$

$$\frac{\partial \varphi}{\partial n} = \chi \qquad \text{on} \quad \partial\Omega_\mathrm{B} \tag{3.7}$$

$$\frac{\partial}{\partial n}(\phi_V + \phi_{WS} + \phi_D + \phi_{FS}) = -U_\infty \hat{i} \cdot \hat{n} \qquad \text{on} \quad \partial\Omega_\mathrm{B} \tag{3.8}$$

$$\frac{\partial \phi_{BS}}{\partial n} = \chi \qquad \text{on} \quad \partial\Omega_\mathrm{B} \tag{3.9}$$

The reason that the body-boundary condition for the viscous potential is satisfied in two parts is because the influence of a constant strength vortex panel (a building block of the linear vortex panel) on itself is zero when applying a condition based on the normal velocity. This means that an individual vortex panel cannot produce a flow through itself and must rely on neighboring panels which would result in a poorly conditioned coefficient matrix.

For each linearly varying strength vortex panel there are two unknowns, γ_0 and γ_1, as depicted in Fig. 3.1. For N_body panels on the body, this means that there are

$2 \cdot N_{\text{body}}$ unknowns. Additional constraint equations can be included to require the vortex strength at the panel ends to be equal. However, a simpler way to achieve a continuous distribution at the panel ends is to actually solve for the unknown strength at the panel ends. This gives $N_{\text{body}} + 1$ unknowns with N_{body} equations. The Kutta condition or total circulation condition serves as the additional equation to solve for the unknown strengths.

As described in Section 2.4.2, the equal-pressure Kutta condition is only used for the inviscid potential while the viscous potential uses the total circulation condition. The equal pressure condition is satisfied by calculating the pressure at two points located behind the trailing edge as shown in Eq. (3.10). Upon testing, the resulting pressure distribution on the body was found to be insensitive to the exact location of the point.

$$\mathbf{x}_{EP}^{+/-} = \mathbf{x}_{TE} + l_{panel}\hat{i} \pm l_{panel}\hat{k} \tag{3.10}$$

Where $\mathbf{x}_{EP}^{+/-}$ is the location of the two points at which the equal pressure condition is enforced.

The equal pressure condition is a non-linear condition, because of this non-linearity the equal pressure condition is not satisfied exactly without iteration. An iterative scheme is not employed because the validation of the pressure coefficient on the body (Section 4.1) is very good, except at one point near the trailing edge. Additionally, the inviscid potential is only used as the initial condition for the velocity decomposition approach and should have no affect on the final solution (as shown in Section 4.3.4).

The total circulation condition uses the Kutta-Joukowski theorem to set the lift on the body in the viscous potential equal to the lift on the body from the Navier-Stokes sub-problem. Eq. (2.58) is discretized as shown in Eq. (3.11).

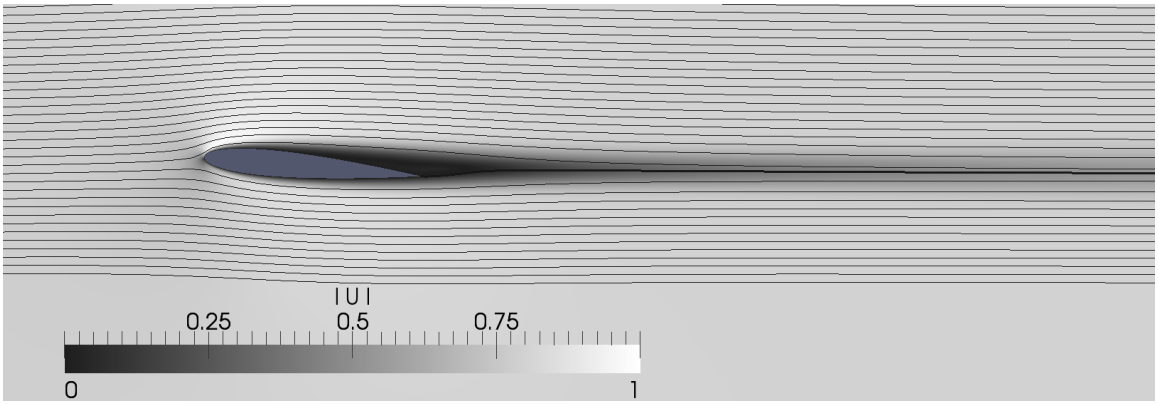

Figure 3.2: Streamlines of the viscous flow overlaid on contours of the magnitude of velocity field over a NACA0012 foil at Re = 200. The streamline emanating from the trailing edge is emphasized.

$$\sum_{m=0}^{N_{\text{body}}} \gamma_m \cdot l_{\text{panel},\, m} = \Gamma^{NS} \tag{3.11}$$

The identical body-boundary condition for the viscous potential is applied to the wake surface as shown in Eq. (3.12). One of the defining characteristics of a lifting flow is an asymmetric wake. For example, Fig. 3.2 shows streamlines and contours of the magnitude of velocity of the flow over a NACA0012 foil at $\alpha = 5°$ with Re = 2000. Especially near the trailing edge, it is clear that the flow above a dividing streamline beginning from the trailing edge is not equal to the flow below it. This asymmetry must be accounted for in the viscous potential. The proposed solution to this problem is to use source and dipole panels coincidentally placed on the wake surface.

$$\frac{\partial \varphi}{\partial n} = \chi \qquad \text{on} \qquad \partial\Omega_{\text{W}} \tag{3.7}$$

$$\frac{\partial}{\partial n}(\phi_V + \phi_{BS} + \phi_{WS} + \phi_D + \phi_{FS}) = -U_\infty \hat{i} \cdot \hat{n} + \chi \qquad \text{on} \qquad \partial\Omega_{\text{W}} \tag{3.12}$$

The boundary condition satisfied on the wake surface will now be developed. To simplify the discussion, first the boundary condition will be developed for the case where only the wake source and dipole distributions are present. The effect of

the body and free-surface singularity distributions will be included once the wake boundary condition has been described.

The body-boundary condition for the viscous potential requires an integration of a partial derivative of the vortical velocity over a line parallel to the body normal vector. Since the wake surface has two normal vectors pointing into the fluid (up and down), there are two boundary conditions that must be satisfied on the wake surface at the same place. The boundary conditions resulting from the integration over the upwards and downwards pointing normal vectors are denoted χ^+ and χ^-, respectively. This presents a problem because there are two different conditions on the normal velocity that must be enforced simultaneously at the same location. The solution to this problem is described in Fig. 3.3 and Eqs. (3.13) and (3.14) where the source panel satisfies the average of the two boundary conditions and the dipole panel satisfies the difference. Physically this means that the source panel is accounting for the thickness of the wake and the dipole panel is representing the asymmetry in the wake. The source and dipole combination is especially suited for this purpose due to the nature of their influence coefficients which describe the nature of the flow induced by each panel. As described in Fig. 3.3, the source panel creates a jump in the normal velocity at the panel center while the dipole panel allows for a continuous normal flow through the panel.

$$\frac{\partial \phi_S}{\partial n} = \frac{\chi^+ + \chi^-}{2} \qquad \text{on} \qquad \partial\Omega_{\mathrm{W}} \tag{3.13}$$

$$\frac{\partial \phi_D}{\partial n} = -U_\infty \hat{i} \cdot \hat{n} + \frac{\chi^+ - \chi^-}{2} \qquad \text{on} \qquad \partial\Omega_{\mathrm{W}} \tag{3.14}$$

However, the problem is only half solved. While it is possible to apply two different boundary conditions for two separate unknowns at the same location, the result would be that the sum of these conditions is applied (which is exactly what is done with the

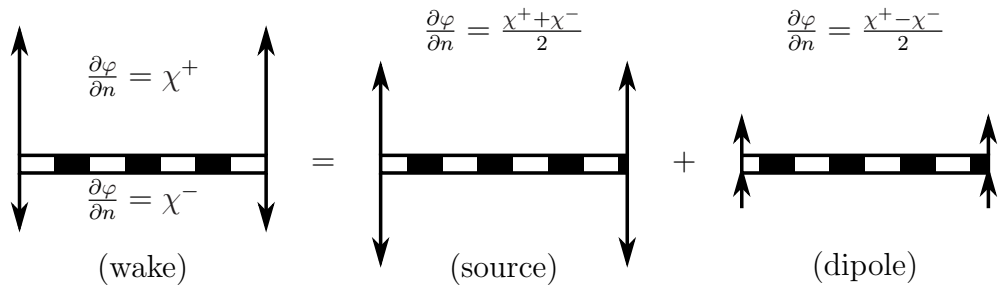

Figure 3.3: The asymmetry in the flow field in the wake results in different values of χ above and below the wake surface; a source panel is used to model the average, while a dipole panel accounts for the asymmetry.

boundary condition on the body). However, as shown in Eq. (3.15), Eq. (3.12) is the result and the information about the asymmetry is lost.

$$\frac{\partial}{\partial n}(\phi_S + \phi_D) = \frac{\chi^+ + \chi^-}{2} + \frac{\chi^+ - \chi^-}{2} - U_\infty \hat{i} \cdot \hat{n} = -U_\infty \hat{i} \cdot \hat{n} + \chi^+ \tag{3.15}$$

The solution to this is to prescribe the wake source strength shown in Eq. (3.16). The dipole strength is solved to satisfy Eq. (3.17), where the body and free-surface singularity distributions are included.

$$\sigma_W = 2 \cdot \left[\frac{\chi^+ + \chi^-}{2}\right] \tag{3.16}$$

$$\frac{\partial}{\partial n}(\phi_V + \phi_{BS} + \phi_D + \phi_{FS}) = -U_\infty \hat{i} \cdot \hat{n} + \frac{\chi^+ - \chi^-}{2} \qquad \text{on} \qquad \partial\Omega_{\mathrm{W}} \tag{3.17}$$

Although this is a simplification that will result in a loss of accuracy in the solution, the loss appears to be minimal because of the observation that source panels which lie along a straight line, as in the case of a flat plate, have zero influence on each other and the source strength can simply be expressed as twice the normal velocity specified at the boundary. This is an acceptable assumption to make because the wake surface is also straight, or in the case that it is placed on a streamline, very

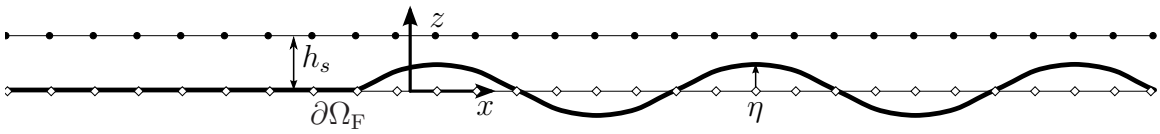

Figure 3.4: The free-surface point sources (solid circles) are located at a distance h_s directly above the free-surface collocation points (empty diamonds).

close to straight.

The combined linear free-surface boundary condition, Eq. (2.41), is satisfied in all free-surface simulations in this work. Point sources are used to represent the free surface instead of flat panels because this greatly simplifies the calculation of the influence coefficients in the free-surface boundary condition. As depicted in Fig. 3.4, the point sources are raised above the mean free-surface. This is done in order to remove the singularity in the calculation of the influence coefficients and to allow the use of point sources instead of panels to represent the free-surface source distribution. The sources are raised to the stagnation height, Eq. (3.18), above the collocation points. The free-surface sources (and collocation points) are equally distributed from the upstream location of the free surface, x_{up}, to the downstream location, x_{down}. The spacing between sources is determined by specifying N_λ, the number of sources per fundamental wavelength. The sensitivity of the calculation of the free-surface elevation to x_{up}, x_{down}, and N_λ is tested in Section 5.1.

$$h_s = \frac{1}{2g} {U_\infty}^2 \tag{3.18}$$

A linear system is formed by computing the influence coefficients for each block of the total coefficient matrix as shown in Eq. (3.19) and Table 3.1. An influence coefficient is calculated by determining the effect of each individual singularity of unit strength on a certain boundary condition at each collocation point. All influence coefficients are calculated analytically using the expressions for point singularities and linearly varying and constant panels found in Katz and Plotkin (1991). When the

effect of the flat panels on the free-surface condition is calculated, the flat panels are represented as a point singularity located at the center of the panel. The expressions for each block, including the inviscid Kutta condition and total circulation condition, are given in Equations 3.20 through 3.39.

$$\begin{bmatrix} \begin{bmatrix}[A]\\[D]\end{bmatrix} & \begin{bmatrix}\mathbf{0}\\\mathbf{0}\end{bmatrix} & \begin{bmatrix}[B]\\\mathbf{0}\end{bmatrix} & \begin{bmatrix}[C]\\\mathbf{0}\end{bmatrix} \\ \mathbf{0} & [E] & \mathbf{0} & \mathbf{0} \\ [F] & [G] & [H] & [I] \\ [J] & [K] & [L] & [M] \end{bmatrix} \cdot \begin{bmatrix} [\gamma] \\ [\sigma_{BS}] \\ [\mu] \\ [\sigma_{FS}] \end{bmatrix} = \begin{bmatrix} \begin{bmatrix}-U_\infty \hat{i} \cdot \hat{n}\\ \Gamma^{NS}\end{bmatrix} \\ \chi \\ \frac{(\chi^+ - \chi^-)}{2} \\ \mathbf{0} \end{bmatrix} - \begin{bmatrix} \begin{bmatrix}\nabla\phi_{WS}\cdot\hat{n}\\ 0\end{bmatrix} \\ \mathbf{0} \\ \mathbf{0} \\ \phi_{WS,xx} + g/{U_\infty}^2 \phi_{WS,z} \end{bmatrix} \tag{3.19}$$

$$A_{l,m} = \nabla\phi_{V,m} \cdot \hat{n}_l \qquad \text{for} \begin{Bmatrix} 0 \le l < N_{\text{body}} \\ 0 \le m < N_{\text{body}} \end{Bmatrix} \tag{3.20}$$

$$B_{l,m} = \nabla\phi_{D,m} \cdot \hat{n}_l \qquad \text{for} \begin{Bmatrix} 0 \le l < N_{\text{body}} \\ 0 \le m < N_{\text{wake}} \end{Bmatrix} \tag{3.21}$$

$$C_{l,m} = \nabla\phi_{FS,m} \cdot \hat{n}_l \qquad \text{for} \begin{Bmatrix} 0 \le l < N_{\text{body}} \\ 0 \le m < N_{FS} \end{Bmatrix} \tag{3.22}$$

$$D_{l,m} = \nabla\phi^+_{V,m} \cdot \nabla\phi^+_{V,m} + \nabla\phi^-_{V,m} \cdot \nabla\phi^-_{V,m} \qquad \text{for} \begin{Bmatrix} l = N_{\text{body}} \\ 0 \le m < N_{\text{body}} \end{Bmatrix} \tag{3.23}$$

coefficient matrix	is the influence of the	on the	condition at
$A_{l,m}$	body vortex panel m	inviscid body boundary	body panel l
$B_{l,m}$	wake dipole panel m	inviscid body boundary	body panel l
$C_{l,m}$	f-s point source m	inviscid body boundary	body panel l
$D_{l,m}$	body vortex panel m	total circulation	-
$E_{l,m}$	body source panel m	viscous body boundary	body panel l
$F_{l,m}$	body vortex panel m	wake boundary	wake panel l
$G_{l,m}$	body source panel m	wake boundary	wake panel l
$H_{l,m}$	wake dipole panel m	wake boundary	wake panel l
$I_{l,m}$	f-s point source m	wake boundary	wake panel l
$J_{l,m}$	body vortex panel m	f-s boundary	f-s col point l
$K_{l,m}$	body source panel m	f-s boundary	f-s col point l
$L_{l,m}$	wake dipole panel m	f-s boundary	f-s col point l
$M_{l,m}$	f-s point source m	f-s boundary	f-s col point l

Table 3.1: The description of each block of the coefficient matrix.

$$D_{l,m} = 1/2 \cdot l_{panel,m} \quad \text{for} \begin{Bmatrix} l = N_{\text{body}} \\ m = 0 \end{Bmatrix} \tag{3.24}$$

$$D_{l,m} = 1/2 \cdot (l_{panel,m-1} + l_{panel,m}) \quad \text{for} \begin{Bmatrix} N_{\text{body}} = 0 \\ 0 < m < N_{\text{body}} \end{Bmatrix} \tag{3.25}$$

$$D_{l,m} = 1/2 \cdot l_{panel,m-1} \quad \text{for} \begin{Bmatrix} N_{\text{body}} = 0 \\ m = N_{\text{body}} \end{Bmatrix} \tag{3.26}$$

$$E_{l,m} = \nabla \phi_{BS,m} \cdot \hat{n}_l \quad \text{for} \begin{Bmatrix} 0 \leq l < N_{\text{body}} \\ 0 \leq m < N_{\text{body}} \end{Bmatrix} \tag{3.27}$$

$$F_{l,m} = \nabla \phi_{V,m} \cdot \hat{n}_l \quad \text{for} \begin{Bmatrix} 0 \leq l < N_{\text{wake}} \\ 0 \leq m \leq N_{\text{body}} \end{Bmatrix} \tag{3.28}$$

$$G_{l,m} = \nabla \phi_{BS,m} \cdot \hat{n}_l \quad \text{for} \begin{Bmatrix} 0 \leq l < N_{\text{wake}} \\ 0 \leq m < N_{\text{body}} \end{Bmatrix} \tag{3.29}$$

$$H_{l,m} = \nabla \phi_{D,m} \cdot \hat{n}_l \quad \text{for} \begin{Bmatrix} 0 \leq l < N_{\text{wake}} \\ 0 \leq m < N_{\text{wake}} \end{Bmatrix} \tag{3.30}$$

$$I_{l,m} = \nabla\phi_{FS,m} \cdot \hat{n}_l \qquad \text{for} \begin{Bmatrix} 0 \leq l < N_{\text{wake}} \\ 0 \leq m < N_{FS} \end{Bmatrix} \tag{3.31}$$

$$J_{l,m} = \phi_{V,xx,m} + g/{U_\infty}^2 \phi_{V,z,m} \qquad \text{for} \begin{Bmatrix} 0 \leq l < N_{FS} \\ 0 \leq m \leq N_{\text{body}} \end{Bmatrix} \tag{3.32}$$

$$J_{l,m} = \phi_{V,z,m} \qquad \text{for} \begin{Bmatrix} l = 0,\ l = N_{FS} - 1 \\ 0 \leq m \leq N_{\text{body}} \end{Bmatrix} \tag{3.33}$$

$$K_{l,m} = \phi_{BS,xx,m} + g/{U_\infty}^2 \phi_{BS,z,m} \qquad \text{for} \begin{Bmatrix} 0 \leq l < N_{FS} \\ 0 \leq m < N_{\text{body}} \end{Bmatrix} \tag{3.34}$$

$$K_{l,m} = \phi_{BS,z,m} \qquad \text{for} \begin{Bmatrix} l = 0,\ l = N_{FS} - 1 \\ 0 \leq m < N_{\text{body}} \end{Bmatrix} \tag{3.35}$$

$$L_{l,m} = \phi_{D,xx,m} + g/{U_\infty}^2 \phi_{D,z,m} \qquad \text{for} \begin{Bmatrix} 0 \leq l < N_{FS} \\ 0 \leq m < N_{\text{wake}} \end{Bmatrix} \tag{3.36}$$

$$L_{l,m} = \phi_{D,z,m} \qquad \text{for} \begin{Bmatrix} l = 0,\ l = N_{FS} - 1 \\ 0 \leq m < N_{\text{body}} \end{Bmatrix} \tag{3.37}$$

$$M_{l,m} = \phi_{FS,xx,m} + g/{U_\infty}^2 \phi_{FS,z,m} \qquad \text{for} \begin{Bmatrix} 0 \leq l < N_{FS} \\ 0 \leq m < N_{FS} \end{Bmatrix} \tag{3.38}$$

$$M_{l,m} = \phi_{FS,z,m} \qquad \text{for} \begin{Bmatrix} l = 0,\ l = N_{FS} - 1 \\ 0 \leq m < N_{FS} \end{Bmatrix} \tag{3.39}$$

The linear system is solved using the open-source linear algebra package, LAPACK (Anderson et al., 1999). An LU-decomposition is used to invert the matrix of influence coefficients. Once the matrix is inverted, it is multiplied by the sum of the right-hand vectors to obtain the unknown strengths. The inverted matrix is saved in memory in order to save computational effort. After the unknowns are obtained, the boundary

conditions are checked for convergence. If all boundary conditions are satisfied to within $1e-8$ tolerance, the system is considered to be converged. The condition number of the entire matrix is also calculated by LAPACK. In practice, if the matrix is invertible by LAPACK, then the reported condition number correlates to a solution accurate to $8-12$ digits (depending on the problem) and the boundary conditions are always satisfied within the tolerance. The only cases encountered where the matrix is not invertible occur when the free-surface source distribution is too dense (when each source has a strong influence on multiple collocation points) or when there was a bug present in the computer code.

3.3 Velocity Decomposition

In this section, the specific details relating to the velocity decomposition approach are discussed. First, the iterative scheme used to solve the coupled sub-problems is described. Then, a numerical maneuver is presented which simplifies the computation of the body-boundary condition for the viscous potential. Next, the specific numerical approaches to determining the location of the δ-boundary and $w_n(\delta)$ (which is used in the calculation of the body-boundary condition for the viscous potential). Finally, a summary is given of the parameters which govern the various numerical schemes described in this chapter.

3.3.1 Iterative Solution Strategy

As described in Chapter 2, the interaction between the viscous potential and the Navier-Stokes sub-problems occurs on the body boundary, wake surface, and the boundary of the reduced domain, $\partial\Omega_{\mathrm{E}}$, through Eqs. (2.27) and (2.52).

$$\mathbf{u} = \nabla\varphi \qquad \text{on} \qquad \partial\Omega_{\mathrm{E}} \tag{2.27}$$

$$\frac{\partial\varphi}{\partial n} = -\int_0^{\delta} \frac{\partial w_t}{\partial t}\,\mathrm{dn} \qquad \text{on} \qquad \partial\Omega_{\mathrm{B}} \text{ and } \partial\Omega_{\mathrm{W}} \tag{2.52}$$

Eq. (2.52) provides the interaction from the Navier-Stokes sub-problem to the viscous potential sub-problem. Eq. (2.27) provides the interaction from the viscous potential sub-problem to the Navier-Stokes sub-problem. The two sub-problems are coupled and either need to be solved in a fully coupled manner or using an iterative scheme. An iterative approach is more fitting to this problem, mainly because the Navier-Stokes equations in the Navier-Stokes sub-problem are also solved in an iterative manner.

The first step in the iterative scheme is to initialize the Dirichlet condition for total velocity on $\partial\Omega_{\mathrm{E}}$ to the inviscid velocity potential, Eq. (3.40).

$$\mathbf{u}^0 = \nabla\Phi \qquad \text{on} \qquad \partial\Omega_{\mathrm{E}} \tag{3.40}$$

The Navier-Stokes equations are then solved iteratively using the SIMPLE algorithm, as described in Section 3.1, until the system of equations is partially converged. Once the equations reach partial convergence, the body-boundary condition for the viscous potential is computed from the viscous flow. The viscous potential is then calculated and the Dirichlet condition for the total velocity is updated, Eq. (3.41).

$$\mathbf{u}^i = \nabla\varphi^i \qquad \text{on} \qquad \partial\Omega_{\mathrm{E}} \tag{3.41}$$

Where the superscript i is the velocity decomposition update number. Each time the viscous potential is re-calculated and the boundary condition on $\partial\Omega_{\mathrm{E}}$ is updated is referred to as one *velocity decomposition update*. In most cases, three to five velocity

decomposition updates are needed. The iterative scheme is described schematically in Fig. 3.5.

The partial convergence of the Navier-Stokes sub-problem is determined by the user as an input parameter, res_{update}. As shown in Fig. 3.5, once the maximum initial residual of the momentum equations drops below res_{update} the viscous potential is calculated and the boundary condition on the reduced domain is updated. The Navier-Stokes sub-problem is then solved with the updated boundary conditions until partial convergence is reached again. As the updates proceed, the Navier-Stokes sub-problem is allowed to become more converged before updating the boundary condition on the reduced domain. In order to achieve this, res_{update} is modified as shown in Eq. (3.42).

$$res_{\text{update}}{}^{i} = res_{\text{update}}/2^{(i-1)} \tag{3.42}$$

The total number of velocity decomposition updates, N_{updates}, is also controlled by the user. The number of updates needed for a problem is generally chosen from experience. Usually, three to five updates is all that is required to achieve a converged solution. An investigation of the impact of N_{updates} and res_{update} parameters on the final solution is discussed in Section 4.3.3.

Throughout this thesis, the term *velocity decomposition* refers to the iterative approach of solving the Navier-Stokes and viscous potential sub-problems in order to achieve the solution of the full Navier-Stokes problem. While the term *viscous potential* specifically refers to the velocity potential which satisfies the Navier-Stokes problem outside of the vortical regions of the flow.

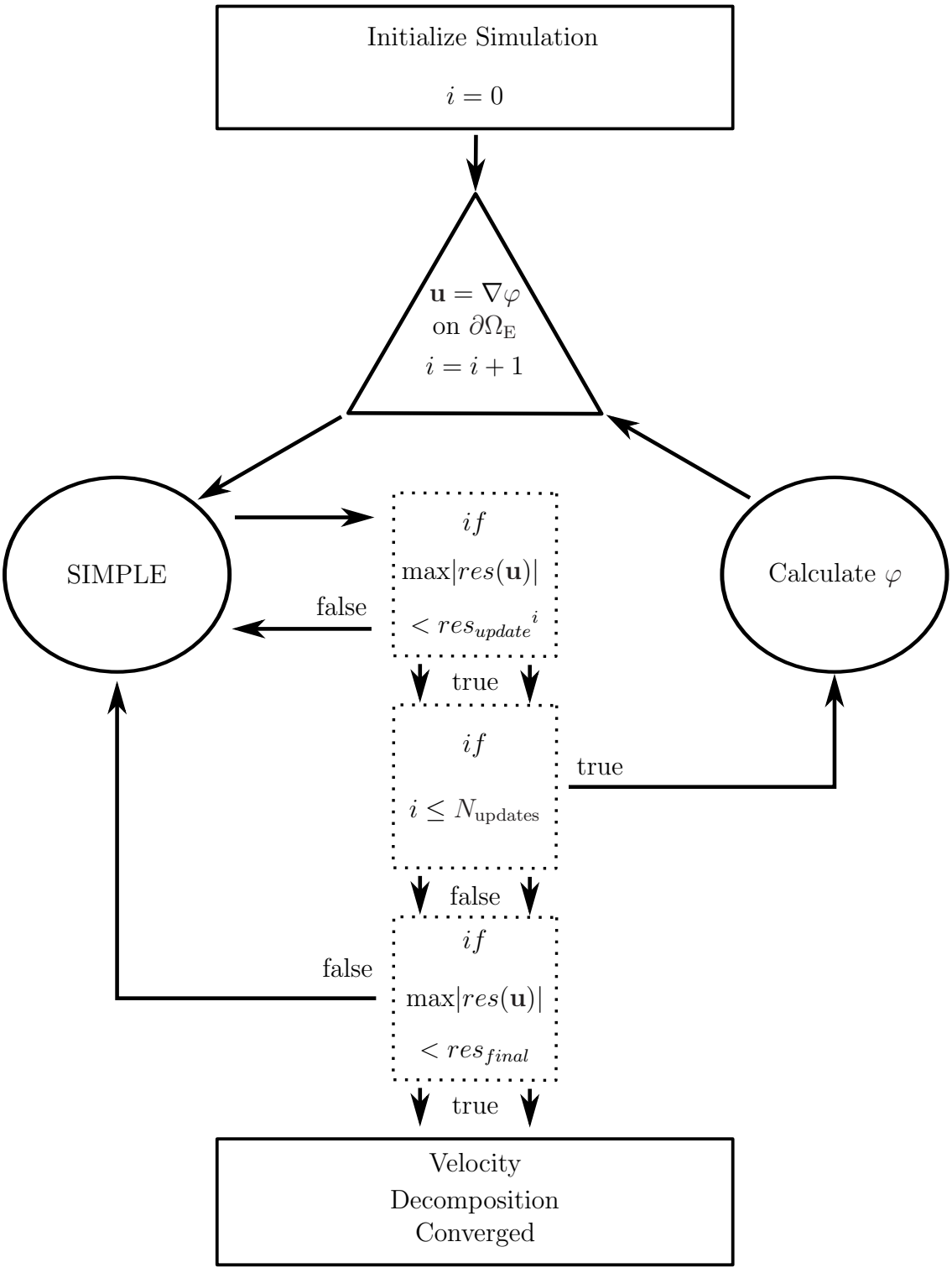

Figure 3.5: The iterative velocity decomposition solution strategy.

3.3.2 Viscous Potential Inner Loops

As often stated, one of the purposes of using velocity decomposition is to decrease the computation time required to solve the Navier-Stokes problem by reducing the size of the Navier-Stokes domain. This is achieved by finding a velocity potential which satisfies the Navier-Stokes problem *directly* outside of the vortical region. This is done by using the viscous potential which is modified to includ viscous effects. One of the principle ways of including viscous effects is through the use of the body-boundary condition for the viscous potential, Eq. (2.52). Clearly, the body boundary condition for the viscous potential is a function of the vortical velocity. This presents a problem because the vortical velocity is calculated as the difference between the total velocity and the viscous potential. Therefore, the viscous potential and vortical velocity are both initially unknown and also are dependent on each other. Once again, the most straightforward solution to this problem is to use an iterative approach.

The iterative approach given in Edmund (2012), is identical to that which is used here and is described below. First, a number of equations previously defined are re-stated for convenience. Eq. (2.32) is the body-boundary condition for the viscous potential directly derived from substituting the velocity decomposition expression into the non-penetration body-boundary condition. Eq. (2.52) is the final expression for the body boundary condition for the viscous potential. Eq. (3.44) is an identity which was used to formulate Eq. (2.52) and is used to develop the iterative approach here.

$$\frac{\partial \varphi}{\partial n} = -\mathbf{w} \cdot \hat{n} \qquad \text{on} \qquad \partial\Omega_{\mathrm{B}} \tag{2.32}$$

$$= -w_n(0) \tag{3.43}$$

$$-\int_0^{\delta} \frac{\partial w_t}{\partial t}\, \mathrm{dn} = w_n(0) - w_n(\delta) \tag{3.44}$$

$$\frac{\partial \varphi}{\partial n} = -\int_0^{\delta} \frac{\partial w_t}{\partial t}\, \mathrm{dn} \qquad \text{on} \qquad \partial\Omega_{\mathrm{B}} \tag{2.52}$$

When calculating the body-boundary condition for the viscous potential, the total velocity field and inviscid potential are initially known. The approach begins with a vortical velocity field calculated as the difference between the total velocity and the inviscid velocity potential, as shown in Eq. (3.45). The first iteration of the body-boundary condition for the viscous potential is calculated from this vortical velocity field as shown in Eq. (3.46).

$$\mathbf{w}^{(0)} = \mathbf{u} - \nabla\Phi \tag{3.45}$$

$$\frac{\partial \varphi}{\partial n}^{(1)} = -\int_0^{\delta} \frac{\partial w_t}{\partial t}^{(0)} \mathrm{dn} \tag{3.46}$$

Where the superscript is the iteration counter for each loop. Eq. (3.47) gives the next, and subsequent, iterations where j is the iteration counter.

$$\frac{\partial \varphi}{\partial n}^{(j)} = -\int_0^{\delta} \frac{\partial w_t}{\partial t}^{(j-1)} \mathrm{dn} \tag{3.47}$$

Eq. (3.44) is now used to relate the integral term to two point values of the vortical velocity as shown in Eq. (3.48). This is a great simplification which avoids numerical

approximation of the integral term.

$$\frac{\partial\varphi}{\partial n}^{(j)} = -w_n(0)^{(j-1)} + w_n(\delta)^{(j-1)} \tag{3.48}$$

Where $w_n(\delta)^{(j-1)}$ is non-zero because the correct body-boundary condition for the viscous potential has not been determined yet. A final adjustment to Eq. (3.48) is made by using Eq. (3.43). Eq. (3.49) shows that the correction to body-boundary condition for the viscous potential at each iteration is simply the value of the vortical velocity at the $\delta-$boundary. This is demonstrated in Table 3.2.

$$\frac{\partial\varphi}{\partial n}^{(j)} = \frac{\partial\varphi}{\partial n}^{(j-1)} + w_n(\delta)^{(j-1)} \tag{3.49}$$

j	$\frac{\partial\varphi^j}{\partial n}$	$w_n^j(0)$	$w_n^j(\delta)$
0	0	0	$\neq 0$
1	$w_n(\delta)^0$	$-w_n(\delta)^0$	$\neq 0$
2	$w_n(\delta)^0 + w_n(\delta)^1$	$-w_n(\delta)^0 - w_n(\delta)^1$	$\neq 0$
3	$w_n(\delta)^0 + w_n(\delta)^1 + w_n(\delta)^2$	$-w_n(\delta)^0 - w_n(\delta)^1 - w_n(\delta)^2$	$\neq 0$
n	$\sum_{j=1}^{n} w_n(\delta)^{j-1}$	$-\frac{\partial\varphi^n}{\partial n}$	$= 0$

Table 3.2: A table showing the evolution of the iterative scheme used to determine the body-boundary condition for the viscous potential.

Although a concrete proof is not given, it has been demonstrated that this scheme results in a viscous potential which satisfies the Navier-Stokes problem outside of the vortical region (the vortical velocity is non-zero only in the vortical regions).

The convergence of this loop is determined by calculating ${\epsilon_\varphi}^j$. ${\epsilon_\varphi}^j$ is a panel length weighted average of the change in the boundary condition for the viscous potential at each panel on the body and wake surface, Eq. (3.50). The use of a convergence criteria is new to this work and has, in practice, shown to be a useful metric to determine

convergence of the viscous potential. The loop is considered converged when ${\epsilon_\varphi}^j$ is less than ϵ_φ. The value ϵ_φ is usually 0.01 to 0.10. The effect of this parameter on the resulting viscous potential is examined in Section 4.3.2.

$$ {\epsilon_\varphi}^j = \frac{\sum_{l=1}^{N_{\text{body}}+N_{\text{wake}}} \frac{w_n(\delta)_l^i - w_n(\delta)_l^{(i-1)}}{w_n(\delta)^{(i-1)}} \cdot l_{panel,l}}{\sum_{j=1}^{N_{\text{body}}+N_{\text{wake}}} l_{panel,l}} \tag{3.50} $$

A flowchart of the iterative scheme described here to determine the viscous potential is shown in Fig. 3.6.

3.3.3 Determination of δ and $w_n(\delta)$

At the beginning of each viscous potential update, the location of the δ-boundary must be determined. The location of the δ-boundary is determined for each panel and is defined as a scalar distance away from the panel center in the panel normal direction. First, the vorticity field is sampled along a line extending from the center of the panel out to a distance $\delta_{\max}$ in the normal direction. The maximum value of the magnitude of vorticity along this sample line is determined. Once the maximum vorticity is found, the vorticity field is sampled along the normal line again until the magnitude of the vorticity vector decreases to below the threshold value, Eq. (3.51).

$$ |\omega|_{threshold} = \beta_{\boldsymbol{\omega}} \cdot |\omega|_{max} \tag{3.51} $$

Where $\beta_{\boldsymbol{\omega}}$ is specified by the user. For efficiency, as well as to avoid any possible oscillatory behavior in the vorticity field, the second sample line begins at the location of the maximum magnitude of vorticity. Once the sample procedure has found a value below the threshold vorticity, the value of δ is determined by linearly interpolating the adjacent values of vorticity to determine the "exact" distance to the threshold vorticity. The linear interpolation results in a smoother δ-boundary, which gives more

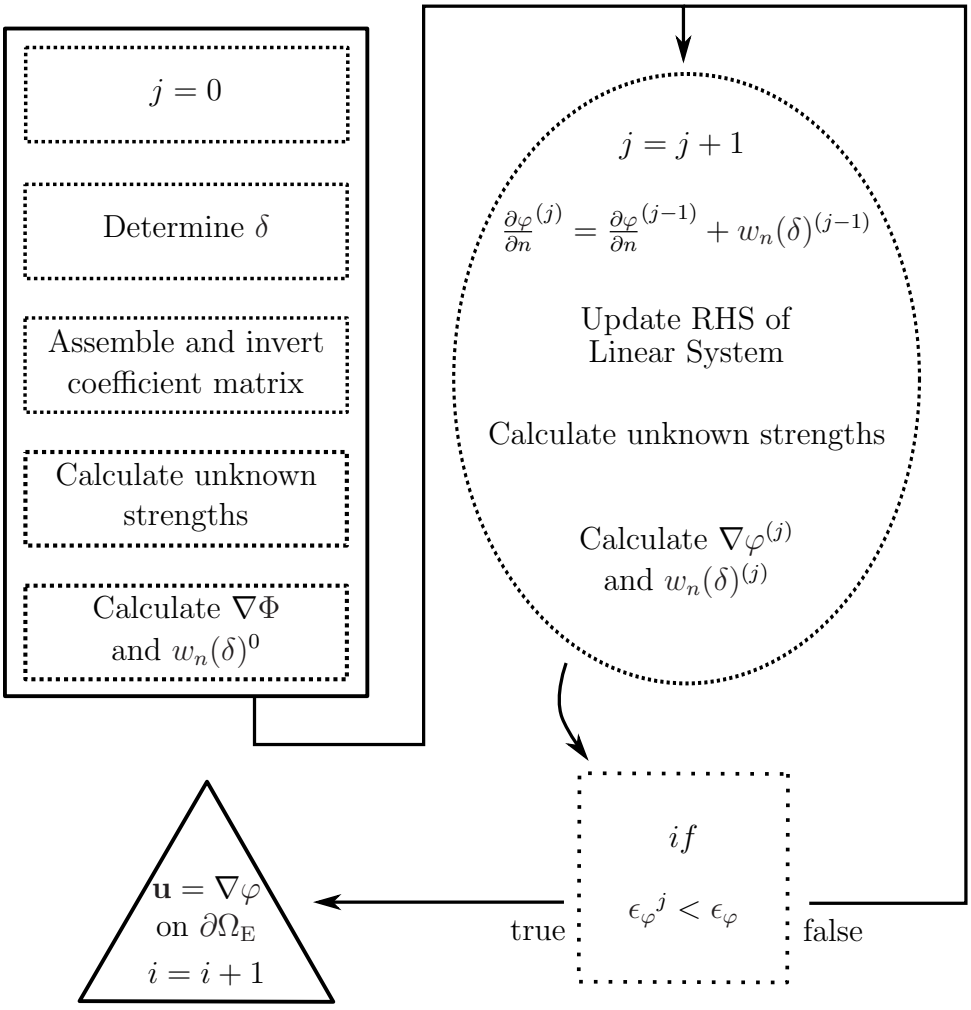

Figure 3.6: A flowchart describing the iterative loop to determine the viscous potential.

consistent results.

To compute the value of $w_n(\delta)$, $\nabla\varphi(\delta)$ and $\mathbf{u}(\delta)$ are needed. $\nabla\varphi(\delta)$ can be computed directly using the singularity strengths from the previous iteration. $\mathbf{u}(\delta)$ is interpolated from the nearest cell center, as shown in Eq. (3.52).

$$\mathbf{u}(\delta) = \mathbf{u}(\mathbf{x}_c) + ((\mathbf{x}_p + \delta\hat{n}) - \mathbf{x}_c) \cdot \nabla\mathbf{u}(\mathbf{x}_c) \tag{3.52}$$

Where $\mathbf{x}_c$ is the location of the cell center closest to the location of the $\delta-$boundary, $\mathbf{x}_p$ is the location of a panel center, and $\nabla\mathbf{u}(\mathbf{x}_c)$ is approximated using the finite-volume method.

3.3.4 Summary of Parameters

In total, there are 12 parameters which control the iterative velocity decomposition approach and the determination of the viscous potential. Two parameters affect the velocity decomposition scheme while nine parameters affect the calculation of the viscous potential and one affects the Navier-Stokes sub-problem. The two parameters which affect the velocity decomposition approach are res_{update} and N_{updates} and were previously discussed in Section 3.3.1. The convergence of the Navier-Stokes sub-problem is controlled with res_{final}. When the initial residual of the momentum equation drops below res_{final}, then the Navier-Stokes sub-problem is considered converged.

Of the nine parameters which govern the calculation of the viscous potential, three determine the discretization of the wake surface, two control the location of the $\delta-$boundary, and three determine the discretization of the free surface. The final parameter is ϵ_φ which determines the convergence of the loop to determine the body-boundary condition for the viscous potential.

The wake is discretized using three parameters. First, the number of wake panels,

N_{wake}, is simply the number of wake panels used for a specific case. Secondly, the length of the first wake panel is Δ_{wake}. Finally, ζ_{wake} defines the growth rate of the length of the wake panels. The wake panels emanate from the trailing edge of the body along a streamline or a line parallel to the x-axis. The length of wake panel i, $l_{panel,i}$, is given by Eq. (3.53).

$$l_{panel,i} = \Delta_{\text{wake}} * (1 + \zeta_{\text{wake}})^{i-1} \qquad \text{for} \qquad 1 \leq i \leq N_{\text{wake}} \tag{3.53}$$

The total length of the wake surface is given in Eq. (3.54).

$$l_{total} = \Delta_{\text{wake}} * \frac{1 + {\zeta_{\text{wake}}}^{n} - 1}{\zeta_{\text{wake}}} \tag{3.54}$$

Eq. (3.54) is used to solve for N_{wake} as shown in Eq. (3.55).

$$N_{\text{wake}} = \frac{\log\left(\frac{l_{total} * \zeta_{\text{wake}}}{\Delta_{\text{wake}}} + 1\right)}{\log(1 + \zeta_{\text{wake}})} \tag{3.55}$$

Δ_{wake} is set to be equal to the average length of the trailing edge body panels. This provides a smooth transition between the body and wake panels. ζ_{wake} and N_{wake} are chosen by the user of the software code. Generally the best approach is to choose the desired total length of the wake panels and then use the above relations to calculate the ζ_{wake} and N_{wake}. The effect of the wake surface parameters on the calculation of the viscous potential is investigated in Section 4.3.3.

There are two parameters that control the location of the δ-boundary. The first is $\delta_{\max}$ which is a cutoff for the sampling of the vorticity field. The reason for this cut-off is that the boundary of the reduced domain $\partial\Omega_{\text{E}}$ generates vorticity due to the Dirichlet boundary condition on the total velocity. It is not desirable to incorporate this generated vorticity into the viscous potential because it is purely a numerical effect. Therefore, the value of $\delta_{\max}$ is set by based on the characteristics of the flow field and the geometry of the computational domain. $\delta_{\max}$ has little to no effect on the

parameter	function
l_{wake}	total length of the wake surface
Δ_{wake}	initial spacing of the wake panels
ζ_{wake}	wake panel growth factor
N_{wake}	total number of wake panels
$\beta_{\boldsymbol{\omega}}$	fraction of $max(\lvert\boldsymbol{\omega}\rvert)$ considered negligible
δ_{max}	maximum distance to search for negligible $\lvert\boldsymbol{\omega}\rvert$
ϵ_{φ}	convergence parameter for the viscous potential loops
res_{final}	convergence parameter for the SIMPLE algorithm
res_{update}	max residual of the momentum equations to initiate the first velocity decomposition update
N_{updates}	number of velocity decomposition updates
x_{up}	the upstream location of the free surface
x_{down}	the downstream location of the free surface
N_{λ}	the number of free-surface point sources per fundamental wavelength

Figure 3.7: A summary of the parameters which govern the calculation of the viscous potential and the numerical solution of the velocity decomposition problem.

final viscous potential. If the vorticity field has not decayed to below the threshold before δ_{max} is reached, then the body-boundary condition for that panel reverts to the inviscid non-penetration condition. The second parameter is $\beta_{\boldsymbol{\omega}}$ which is the fraction of the maximum value of vorticity which is considered negligible. $\beta_{\boldsymbol{\omega}}$ was discussed in Section 3.3.3. The effect of the $\beta_{\boldsymbol{\omega}}$ on the viscous potential is investigated in Section 4.3.3.

The three parameters which govern the discretization of the free surface are x_{up}, the x-location of the upstream free-surface boundary, x_{down}, the location of the downstream free-surface boundary, and N_{λ}, the number of point sources (and collocation points) per fundamental wavelength. The effect of the free-surface parameters on the free-surface elevation is investigated in Section 5.1.

CHAPTER 4

Lifting Flow Results

In this chapter the velocity decomposition approach is applied to deeply submerged lifting problems. First, the velocity potential implementation is validated. Then, the approach of using source and doublet distributions on the wake surface to capture flow asymmetry is analyzed by applying that idea to the viscous flow over an infinitely thin flat plate with different boundary layer thicknesses above and below the plate, much like a shear flow. After demonstrating the utility of the wake singularity distribution, the full velocity decomposition method is applied to solve for the laminar flow around a NACA0012 foil at $\alpha = 5°$. Grid convergence studies, including domain size and mesh resolution, are performed. Finally, results are given for the same NACA0012 foil, but at a turbulent Re of 1.34×10^6 at $\alpha = 8°$.

4.1 Validation of the Velocity Potential for Lifting Flow

In this section the panel method for deeply submerged lifting flows is validated against results from XFOIL (Drela, 1989). In all results in this section, the body is discretized using only the linearly-varying vortex panels. Fig. 4.1 shows the pressure coefficient on a NACA0012 foil at $\alpha = 5°$ for three different grid densities compared to the XFOIL result (using 160 panels, the default setting). Table 4.1 gives the lift

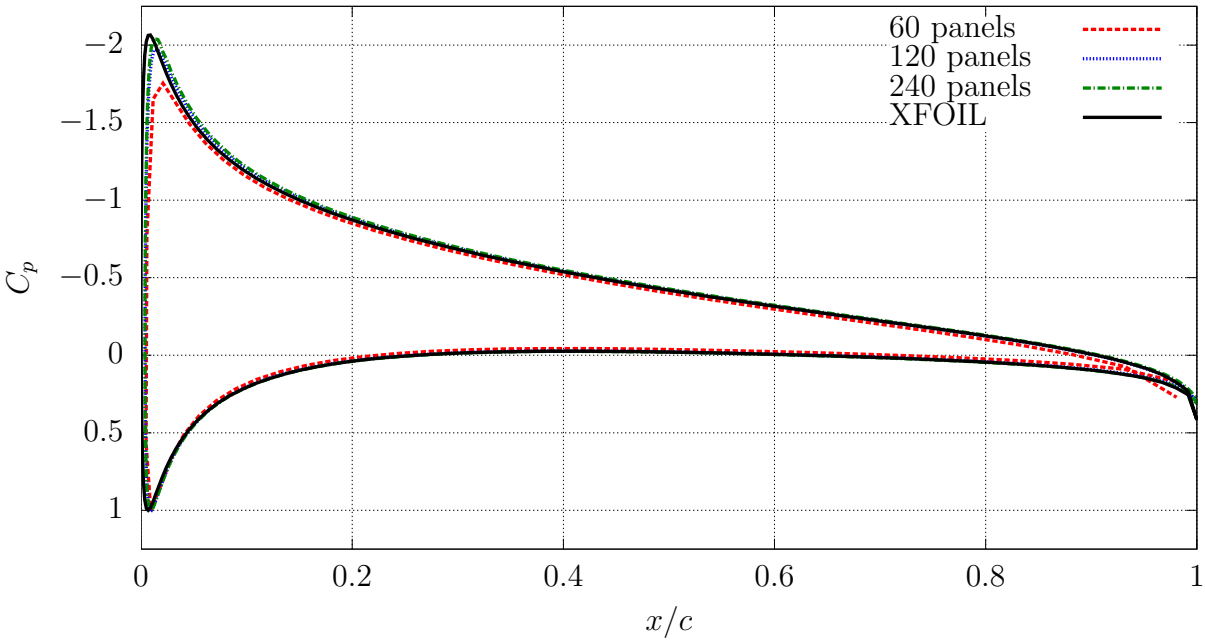

Figure 4.1: Coefficient of pressure (C_p) on the body for the deeply-submerged NACA0012 airfoil at $\alpha = 5°$ on three different grids compared to XFOIL (Drela, 1989).

	C_L
XFOIL	0.603
60 panels	0.553
120 panels	0.591
240 panels	0.603

Table 4.1: The lift coefficient, C_L, calculated for the NACA0012 foil at $\alpha = 5°$.

coefficient for the same case. Fig. 4.2 shows the pressure coefficient on a Joukowski foil at $\alpha = 5°$ for three different levels of discretization. Table 4.2 gives the lift coefficient. There is very good agreement for all cases tested.

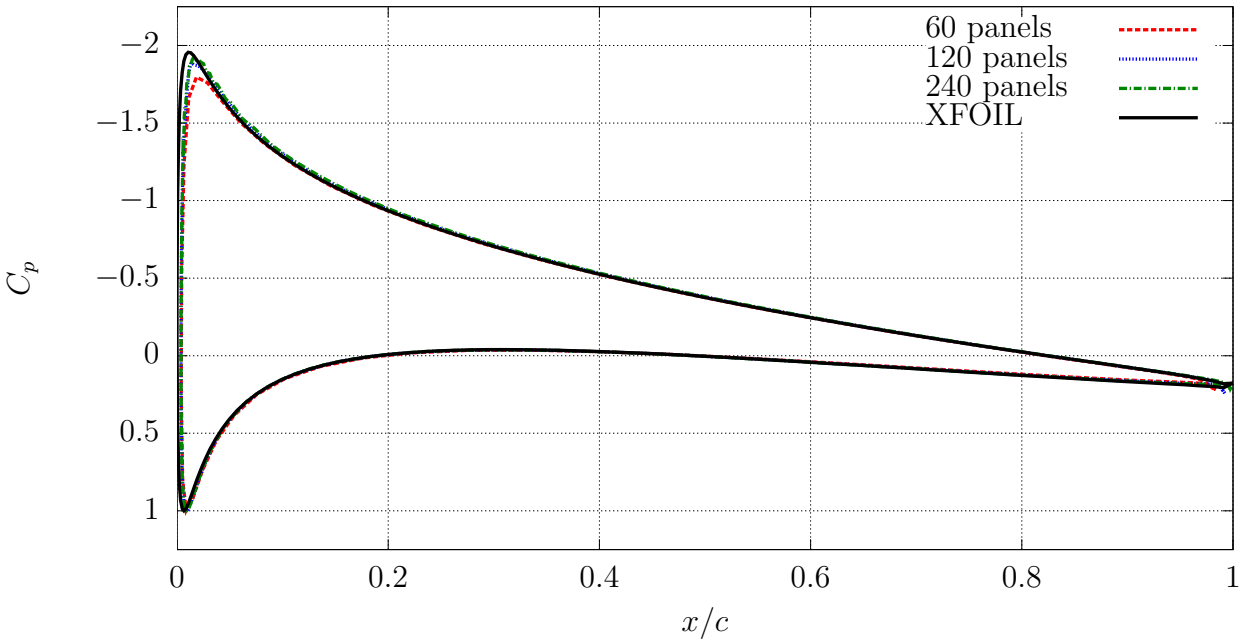

Figure 4.2: Coefficient of pressure (C_p) on the body for the deeply-submerged Joukowski airfoil at $\alpha = 5°$ on three different grids compared to XFOIL (Drela, 1989).

	C_L
XFOIL	0.598
60 panels	0.575
120 panels	0.588
240 panels	0.593

Table 4.2: The lift coefficient, C_L, calculated for the Joukowski foil at $\alpha = 5°$.

4.2 Laminar Flat-plate

In this section, the flow over an infinitely thin flat plate is analyzed in order to study the proposed approach of representing the wake surface in a lifting flow using overlapping source and doublet distributions. The plate has a length of $c = 1.0\ m$, is parallel to the x-axis and the leading edge is located at $(x, z) = (0, 0)$. The free-stream velocity is $U_\infty = 1.0\ m/s$ and the Re's used are 200, 2000, 4000, and ∞ based on the length of the plate.

This section will only examine the ability of the source and dipole approach to calculate a viscous potential from an asymmetric viscous flow. The coupled solver is not used. Also, in these results only, the body is also represented with source and dipole distributions (instead of a vortex and source distribution). This is because the focus of this section is to only examine the wake model in an asymmetric flow.

Navier-Stokes solutions for the Re's listed above were generated on large half-domains split at $z = 0$. The domains were then joined together at $z = 0$. An example of this is shown in Figs. 4.3 and 4.4. In all the results presented, the top half-domain always has the $\mathrm{Re} = 2000$ solution while the bottom half-domain contains either the $\mathrm{Re} = 200$, 4000, or ∞ solutions. The combinations are referred to as $\mathrm{Re}\,2000/200$, $\mathrm{Re}\,2000/4000$, or $\mathrm{Re}\,2000/\infty$. The parameters which govern the calculation of the viscous potential are constant for all simulations and are given in Table 4.3. An in-depth study of the parameters which govern the calculation of the viscous potential and the iterative velocity decomposition approach is described in Section 4.3. The ability of the viscous potential to emulate the real viscous flow is measured by comparing the streamwise velocity of the viscous potential and viscous flow at the midchord ($x/c = 0.5$), trailing edge ($x/c = 1.0$), and in the wake ($x/c = 3.0$) over a sample line perpendicular to the plate from $z/c = -2$ to $z/c = 2$.

Figures 4.5, 4.6 and 4.7 show logarithmic contours of vorticity for the $\mathrm{Re}\,2000/\infty$, $\mathrm{Re}\,2000/200$, and $\mathrm{Re}\,2000/4000$, respectively. Also shown in the figures is the δ-

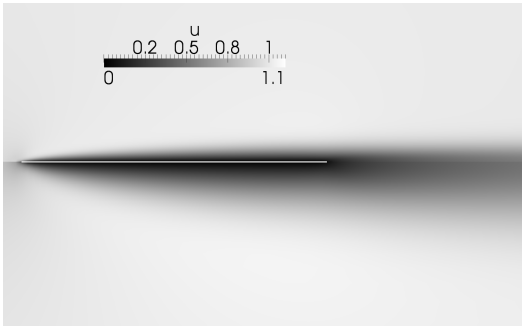

Figure 4.3: Contour of the streamwise velocity for the Re 2000/200 case over the flat plate (white).

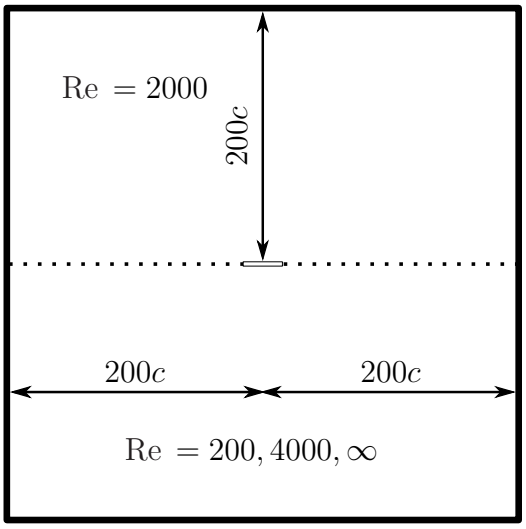

Figure 4.4: Flat plate Navier-Stokes domain size and Re schematic.

parameter	value
N_{body}	100
N_{wake}	230
l_{wake}	125
Δ_{wake}	0.01
ζ_{wake}	0.025
$\beta_{\boldsymbol{\omega}}$	0.025
ϵ_{φ}	0.05
$\delta_{\max}$	50

Table 4.3: A summary of the parameters used to determine the viscous potential for all flat plate calculations.

boundary, colored in black.

Figures 4.8, 4.9 and 4.10 show the velocity profiles for the Re 2000/∞, Re 2000/200, and Re 2000/4000, respectively. The viscous potential shows very good agreement (less than 1%) with the Navier-Stokes flow and is a remarkable improvement over the inviscid potential solution, which would give $u/U_\infty = 1.0$ everywhere. The agreement with the Navier-Stokes flow improves as the difference between Re becomes less, with the best agreement in the Re 2000/4000 case.

Figures 4.11 and 4.12 show the source and dipole strengths along the flat plate and into the wake for the all three cases. The source strengths represent the average

Figure 4.5: The magnitude of the vorticity field for the Re = 2000 / 0 case with the plate outlined in white and the δ-boundary also colored in black, from $x/c = 0.0$ to $x/c = 5.0$.

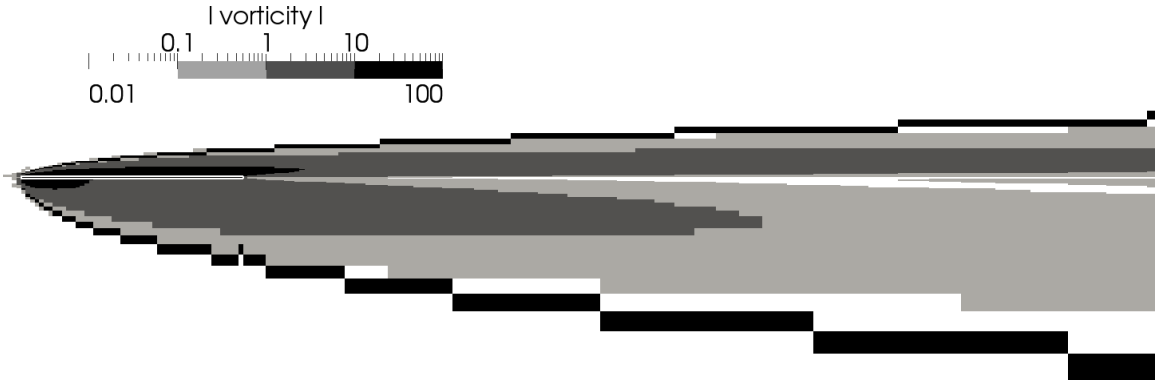

Figure 4.6: The magnitude of the vorticity field for the Re = 2000 / 200 case with the plate outlined in white and the δ-boundary also colored in black, from $x/c = 0.0$ to $x/c = 5.0$

Figure 4.7: The magnitude of the vorticity field for the Re = 2000 / 4000 case with the plate outlined in white and the δ-boundary also colored in black, from $x/c = 0.0$ to $x/c = 5.0$.

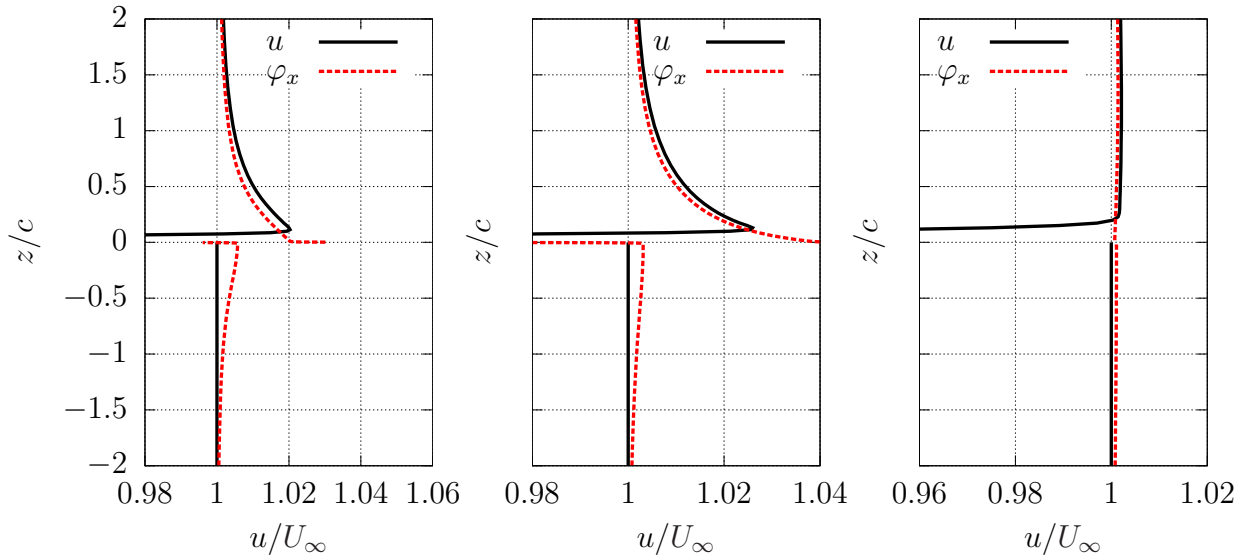

(a) Streamwise velocity at the midchord ($x/c = 0.5$).

(b) Streamwise velocity at the trailing edge ($x/c = 1.0$).

(c) Streamwise velocity in the wake ($x/c = 3.0$).

Figure 4.8: The streamwise velocity at three sample lines for the $\mathrm{Re}\,2000/\infty$ case.

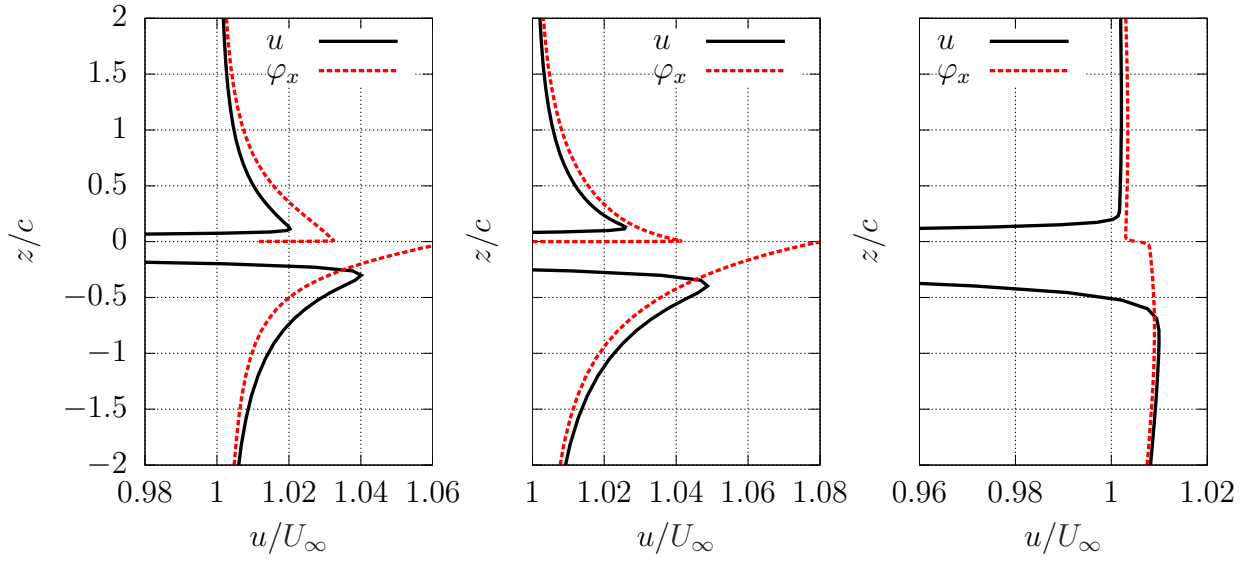

(a) Streamwise velocity at the midchord ($x/c = 0.5$).

(b) Streamwise velocity at the trailing edge ($x/c = 1.0$).

(c) Streamwise velocity in the wake ($x/c = 3.0$).

Figure 4.9: The streamwise velocity at three sample lines for the $\mathrm{Re}\,2000/200$ case.

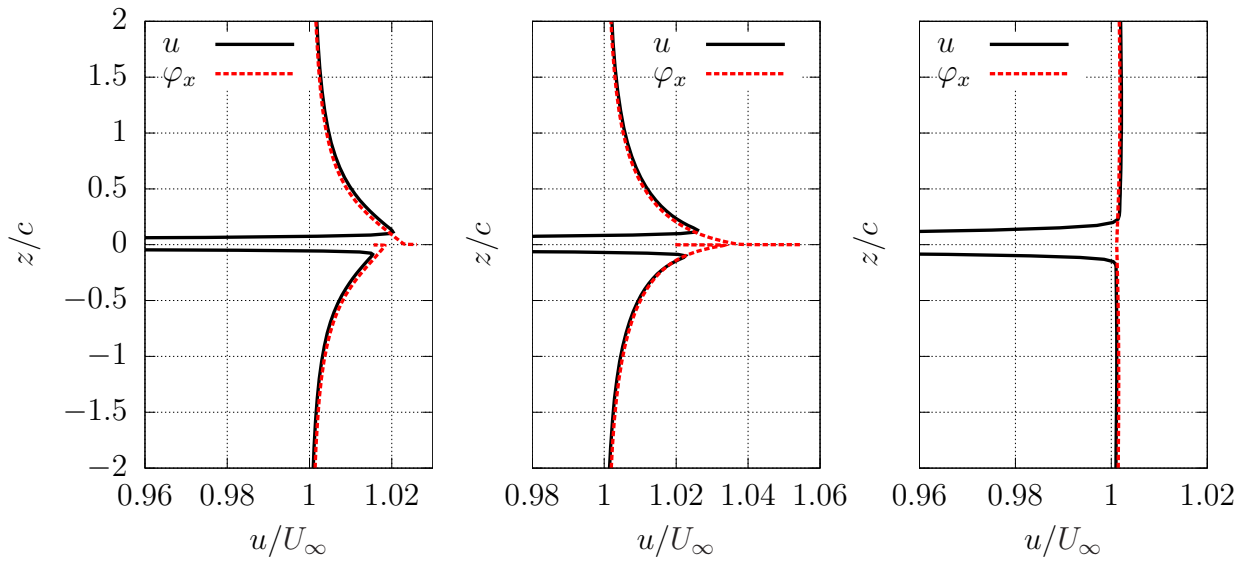

(a) Streamwise velocity at the midchord ($x/c = 0.5$).

(b) Streamwise velocity at the trailing edge ($x/c = 1.0$).

(c) Streamwise velocity in the wake ($x/c = 3$).

Figure 4.10: The streamwise velocity at three sample lines for the Re 2000/4000 case.

thickness of the vortical region, which is why the Re 2000/200 case has the largest strengths, while the Re 2000/∞ has the smallest strengths. For all cases, the strengths are largest on the body and then decay quickly into the wake as the strength of the vorticity decays. In the Navier-Stokes flow, the streamlines constrict slightly near the trailing edge of the body, this is why the source strength is negative directly behind the trailing edge.

The dipole strengths, on the other hand, represent the asymmetry of the flow in the vortical region. The dipole strength on the plate is positive for the Re 2000/4000 and Re 2000/∞ cases because the vortical layer on the top of the plate is thicker than the bottom and requires flow through the plate from the bottom to top to displace the streamlines more. The opposite is the case in the Re 2000/200 case where the thicker vortical layer is on the bottom. This requires flow through the plate from the top to the bottom of the plate.

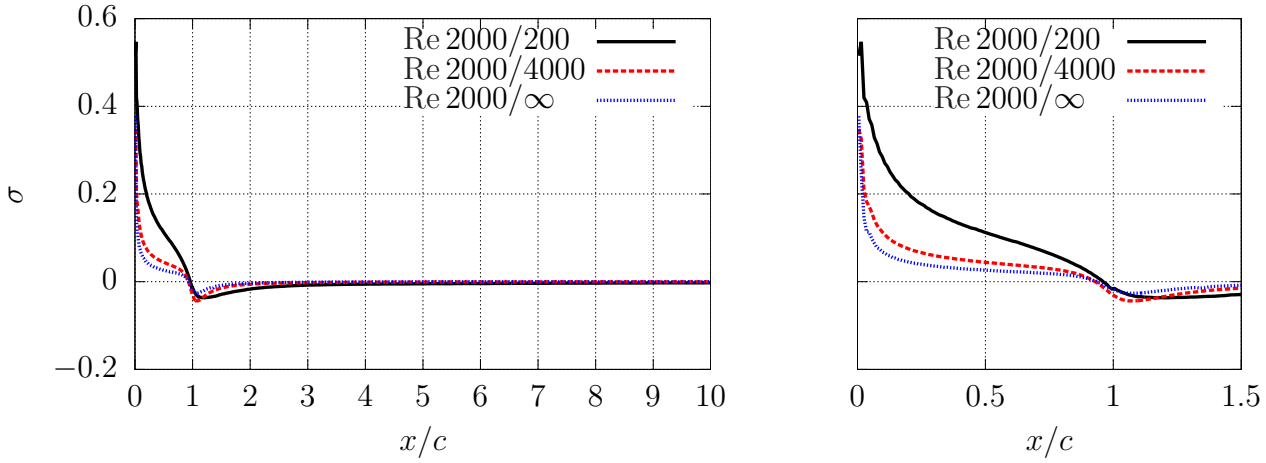

Figure 4.11: The value of the source strengths on the body and in the wake for the flat plate at all three Re combinations. The plot on the left is zoomed-in to show the behavior on the plate.

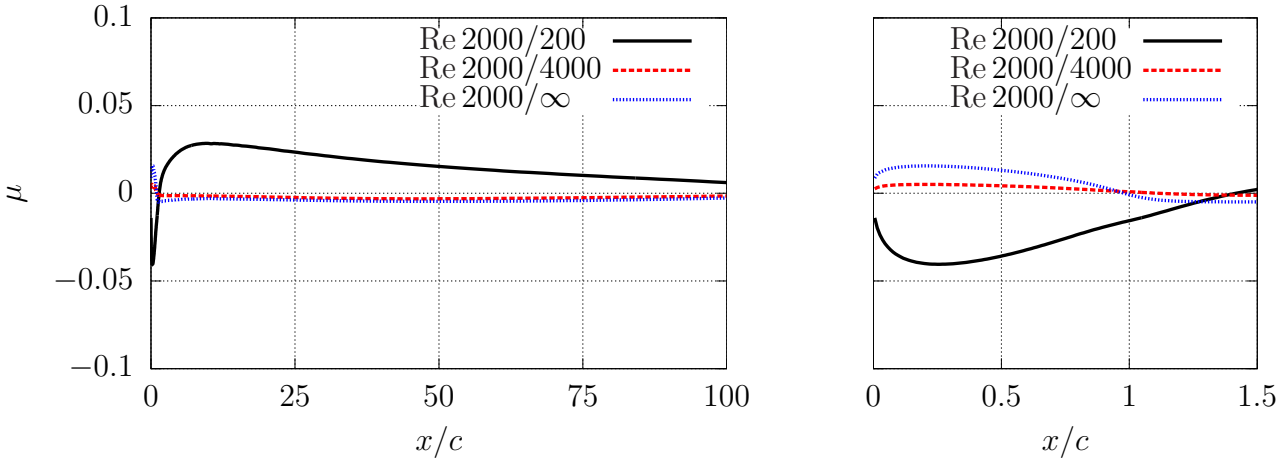

Figure 4.12: The value of the dipole strengths on the body and in the wake for the flat plate at all three Re combinations. The plot on the left is zoomed-in to show the behavior on the plate.

4.3 Laminar NACA-0012 Airfoil

In this section the velocity decomposition approach is applied to NACA0012 foil at α of 5° in an infinite fluid domain. The Re is 2000 based on chord length. A low Re is challenging for the method because it will give a larger vortical region than a higher Re and separation of the flow over the body will occur at a lower angle of attack, as shown in Fig. 4.13. The challenging nature of this problem makes it a good test case. The chord length of the foil is $c = 0.203$ m, the free-stream velocity is $U_\infty = 0.8$ m/s, and the kinematic viscosity is $\nu = 8.12 \cdot 10^{-5}$ m^2/s.

4.3.1 Navier-Stokes Domain Size Study

One of the advantages of using velocity decomposition is to reduce the computational domain size needed to solve the Navier-Stokes problem. This section investigates the effect of domain size on the Navier-Stokes solution without the use of velocity decomposition. This is done in order to be able to evaluate the velocity decomposition solutions later in this section.

The domain sizes in this investigation range from $x_{\text{extent}}/c = 2000$ to $x_{\text{extent}}/c = 1$ where x_{extent} is defined in Fig. 4.14. To be consistent, all grids have the same topology in overlapping regions. In order to minimize the effect of the downstream boundary on the Navier-Stokes solution, the outlet boundary, $\partial\Omega_{\text{O}}$, is located at $x/c = 200$ for domains $x_{\text{extent}}/c = 200$ and smaller. The boundary conditions used for the Navier-Stokes simulations are given in Eqs. (4.1) and (4.2).

$$\mathbf{u} = U_\infty \hat{i} \qquad \frac{\partial p_d}{\partial n} = 0 \qquad \text{on} \qquad \partial\Omega_{\text{E}} \tag{4.1}$$

$$\frac{\partial \mathbf{u}}{\partial n} = \mathbf{0} \qquad p_d = 0 \qquad \text{on} \qquad \partial\Omega_{\text{O}} \tag{4.2}$$

There are four metrics used to evaluate the effect of domain size on the Navier-

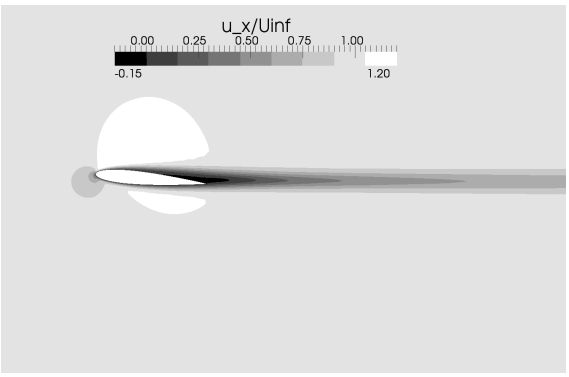

(a) The streamwise component of velocity normalized by the freestream velocity.

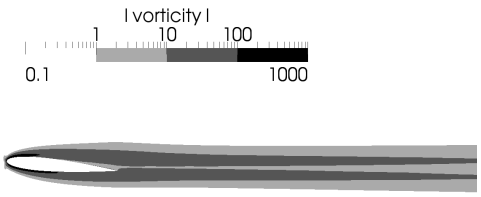

(b) The magnitude of the vorticity.

Figure 4.13: Contours of velocity and vorticity for the flow over the NACA0012 at $\mathrm{Re} = 2000$ and $\alpha = 5°$.

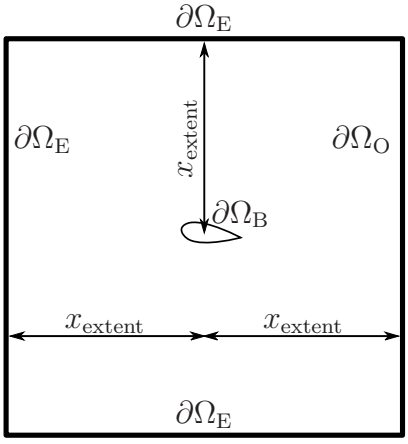

Figure 4.14: The domain and boundary definitions for the NACA0012 foil simulations.

Stokes solution. The first two are the root-mean square error in streamwise velocity over a sample line at midchord and a sample line at the trailing edge, as shown in Fig. 4.15. RMS error is calculated as shown in Eq. (4.3). The velocity is compared at the cell centers of coincident points on each sample line. The solution on the $x_\mathrm{extent}/c = 2000$ domain is used as the baseline for the measurements. The total lift and drag on the foil are also calculated and compared using Eq. (4.4). For all metrics, 0.1% is used as a consistent bound on the error.

Fig. 4.16 shows the error in the lift and drag coefficients and Fig. 4.17 shows the error in the velocity at midchord and at the trailing edge. The error decays linearly

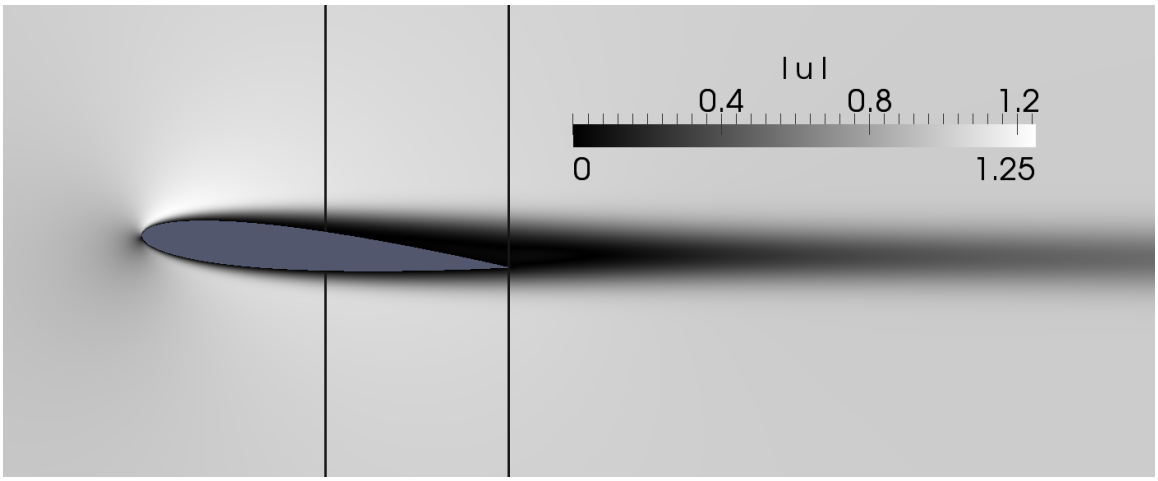

Figure 4.15: The magnitude of velocity over the NACA0012 foil at Re $= 2000$ with $\alpha = 5°$. Also shown are the sample lines at the midchord and trailing edge.

for all metrics on the *log-log* plot. The information in these plots will be later in this section to evaluate the velocity decomposition approach.

$$RMS_{error} = \frac{1}{n}\sqrt{\sum_{i=1}^{n}\left(\frac{\varphi_{x,i} - u_i^{2000c}}{u_i^{2000c}}\right)^2} \tag{4.3}$$

$$C_{(l,d),error} = \left|\frac{C_{(l,d)} - C_{(l,d)}^{2000c}}{C_{(l,d)}^{2000c}}\right| \tag{4.4}$$

4.3.2 Viscous Potential Parameter Study

In this section the five parameters which govern the numerical schemes that calculate the viscous potential are investigated. In order to do this, the viscous potential is calculated using the converged Navier-Stokes velocity field calculated on the $x_{\text{extent}}/c = 2000$ sized domain for a NACA0012 foil at Re $= 2000$ with $\alpha = 5°$. Each set of figures compares the streamwise component of the viscous potential, φ_x, to the streamwise component of the total velocity, u.

The different parameter settings are evaluated by visually investigating the velocity profiles sampled at the midchord and at the trailing edge. The root-mean square

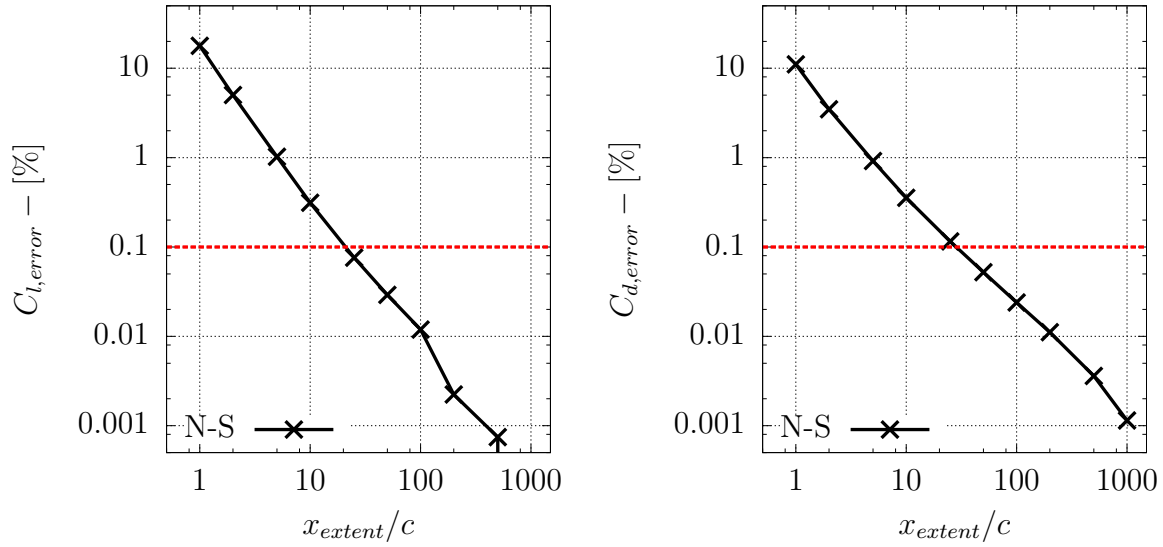

(a) Error in the lift coefficient.

(b) Error in the drag coefficient.

Figure 4.16: The effect of reducing the domain size on the components of the integrated force on the NACA0012 foil at Re $= 2000$ at $\alpha = 5°$.

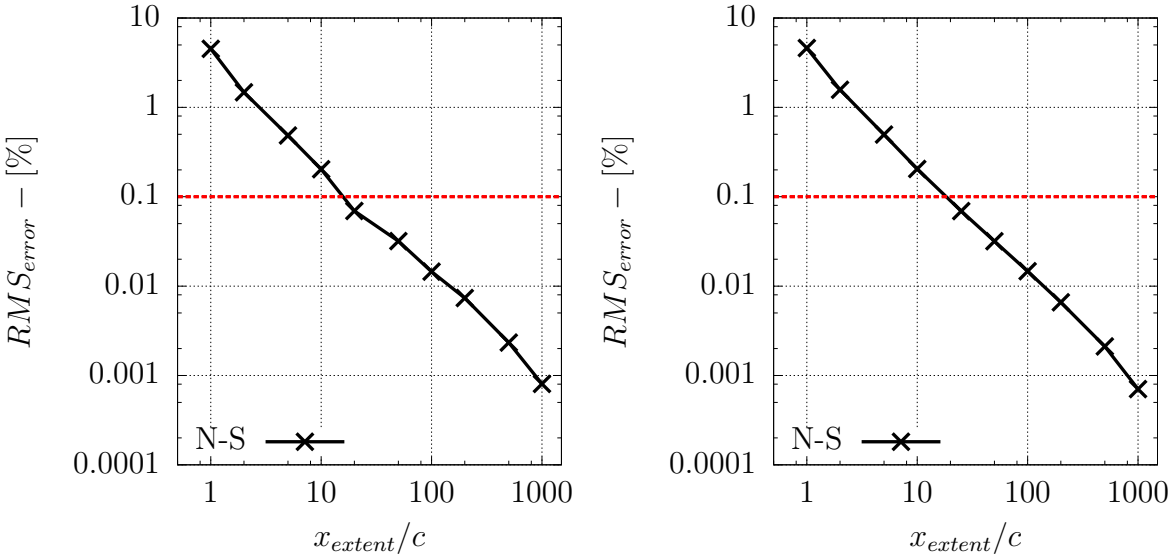

(a) Error in the streamwise velocity at the midchord.

(b) Error in the streamwise velocity at the trailing edge.

Figure 4.17: The effect of reducing the domain size on the streamwise component of velocity over two sample lines on the NACA0012 foil at Re $= 2000$ at $\alpha = 5°$.

parameter	value
$\beta_{\boldsymbol{\omega}}$	0.05
ϵ_{φ}	0.05
l_{wake} / c	10
ζ_{wake}	0.15
wake on streamline?	no

Table 4.4: The baseline parameter values used in the viscous potential parameter study.

error is not used because the error in the vortical region dominates the total error measure when the viscous potential velocity is compared to the Navier-Stokes solution which disguises the small changes caused by the different parameter values. Table 4.4 shows the baseline values of the parameters used. The sensitivity of viscous potential to each parameter is investigated one parameter at a time. When one parameter is changed, the others retain the baseline values.

Fig. 4.18 shows the influence of ϵ_{φ} which dictates the convergence level of the inner loop to calculate the body boundary condition for the viscous potential. Clearly, 25% is a poor choice, however there is very little difference between 5% and 1%. Using $\epsilon_{\varphi} = 5\%$, Fig. 4.19 shows how the velocity profiles at the midchord and at the trailing edge change as the iterative scheme to determine the viscous potential proceeds.

Fig. 4.20 shows the influence of $\beta_{\boldsymbol{\omega}}$ which determines the location of the δ-boundary by altering the threshold at which the vorticity is considered negligible. Again, the 25% threshold is a poor choice while the other two values are more than suitable.

Fig. 4.21 shows the influence of the total length of the wake, l_{wake}, on the viscous potential. The effect of wake length is very minimal, even at the trailing edge. Fig. 4.22 shows the influence of ζ_{wake} which dictates how quickly the length of the wake panels increases away from the trailing edge. The viscous potential is not affected by this parameter. Finally, Fig. 4.23 shows the effect of placing the wake panels on a streamline originating at the trailing edge or simply placing them in a straight line parallel to the $x-$axis emanating from the trailing edge. The streamline approach

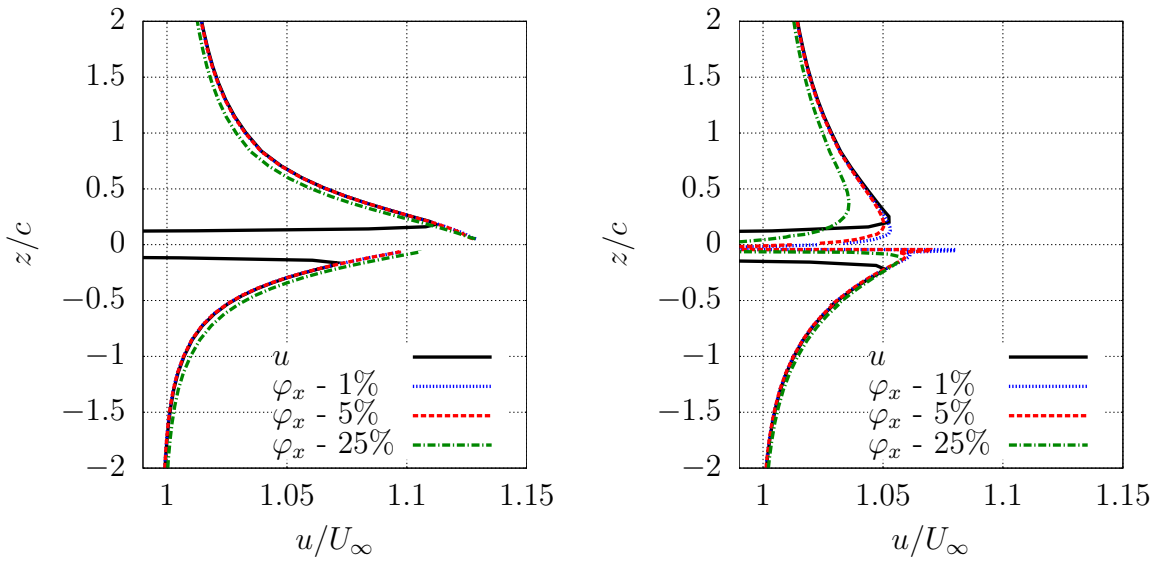

(a) Streamwise velocity at the mid-chord.

(b) Streamwise velocity at the trailing edge.

Figure 4.18: The effect of the inner loop convergence parameter on the streamwise component of the viscous potential compared to the Navier-Stokes result.

gives a slightly better result near the trailing edge, but in both cases the agreement with the Navier-Stokes solution outside of the vortical region is unaffected.

In summary, the calculation of the viscous potential is relatively insensitive to the parameters chosen as long as the values are near those given in Table 4.4. Although, in most cases even the "poor" results agree very well with the Navier-Stokes solution at a distance of one chord length away from the body.

4.3.3 Velocity Decomposition Parameter Study

In this section the two parameters which govern the iterative velocity decomposition approach are investigated. The iterative velocity decomposition method was used to compute the flow over a NACA0012 foil at Re $= 2000$ with $\alpha = 5°$. The inlet of the computational domain was located at $x_{\text{extent}}/c = 2$, while the downstream boundary was placed at $x_{\text{extent}}/c = 200$. A full investigation of the effect of domain size on the velocity decomposition approach is presented in Section 4.3.4.

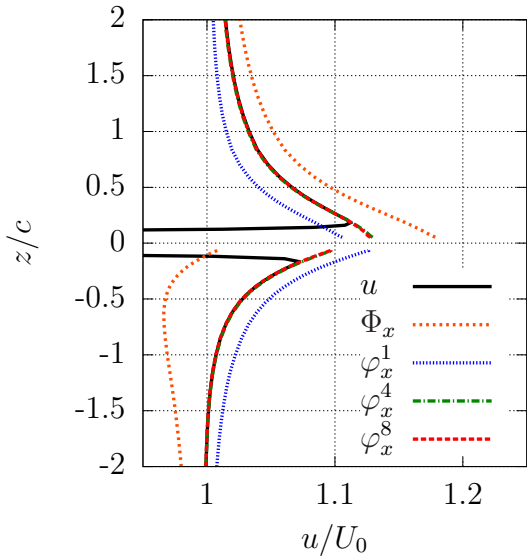

(a) Streamwise velocity at the midchord.

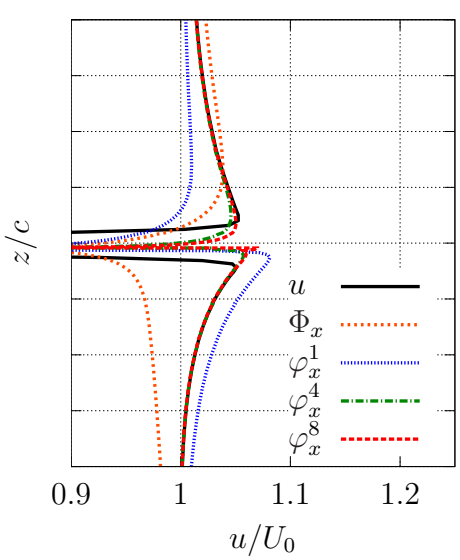

(b) Streamwise velocity at the trailing edge.

Figure 4.19: The evolution of the viscous potential at the midchord and trailing edge compared to the inviscid potential and Navier-Stokes solution.

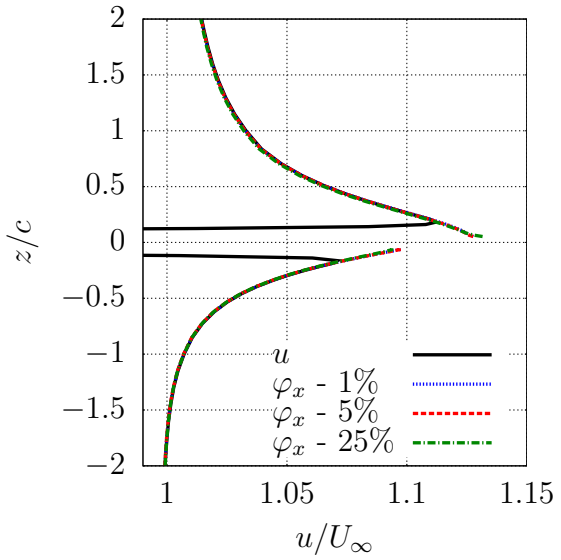

(a) Streamwise velocity at the midchord.

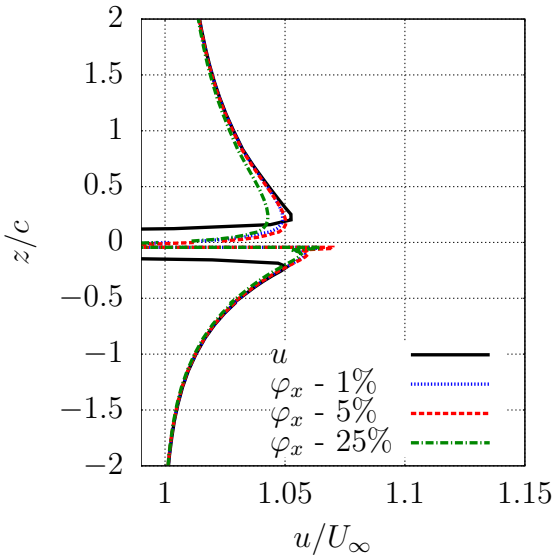

(b) Streamwise velocity at the trailing edge.

Figure 4.20: The effect of the vorticity limit parameter ($\beta_{\boldsymbol{\omega}}$) on the streamwise component of the viscous potential compared to the Navier-Stokes result.

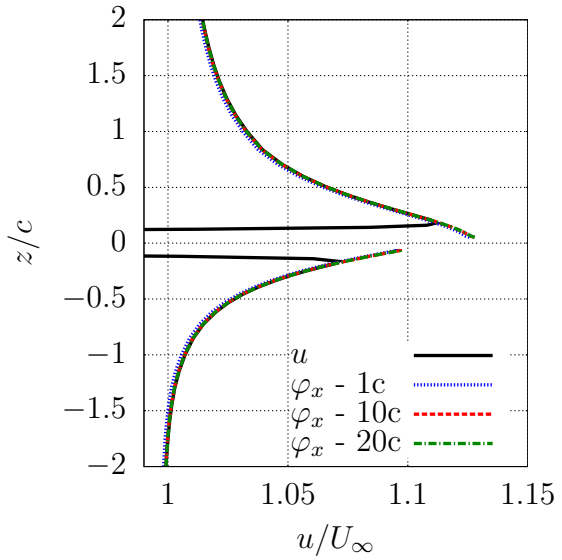

(a) Streamwise velocity at the mid-chord.

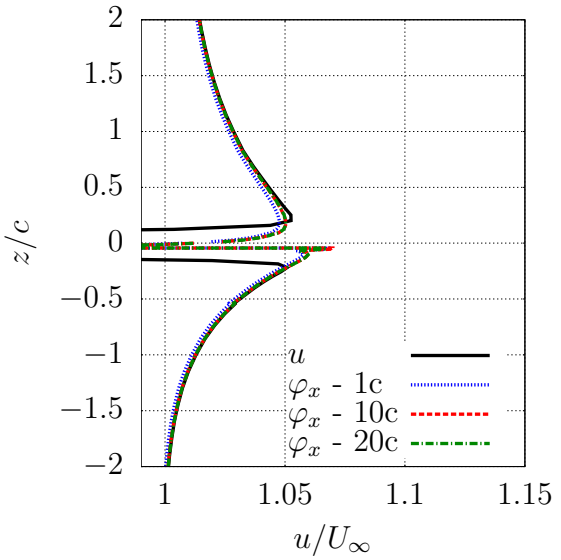

(b) Streamwise velocity at the trailing edge.

Figure 4.21: The effect of the total wake length on the streamwise component of the viscous potential compared to the Navier-Stokes result.

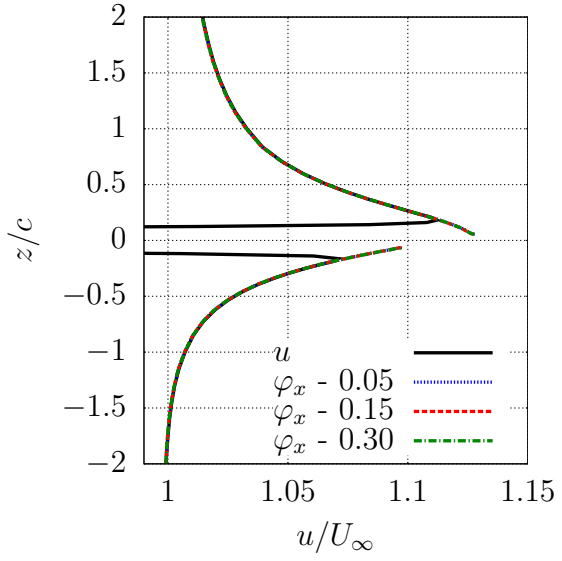

(a) Streamwise velocity at the mid-chord.

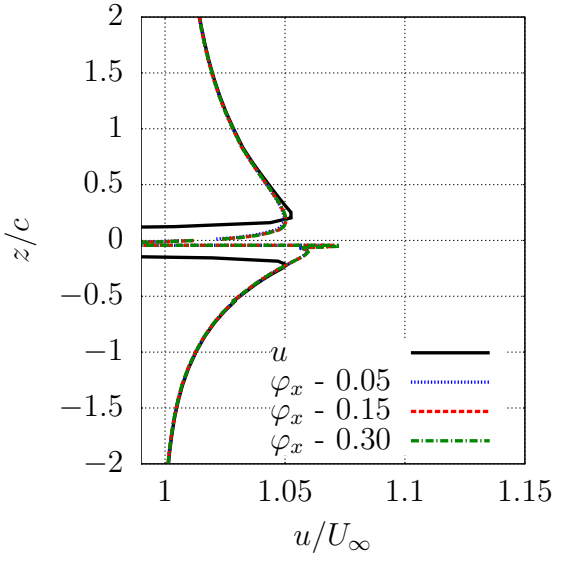

(b) Streamwise velocity at the trailing edge.

Figure 4.22: The effect of the wake panel growth parameter on the streamwise component of the viscous potential compared to the Navier-Stokes result.

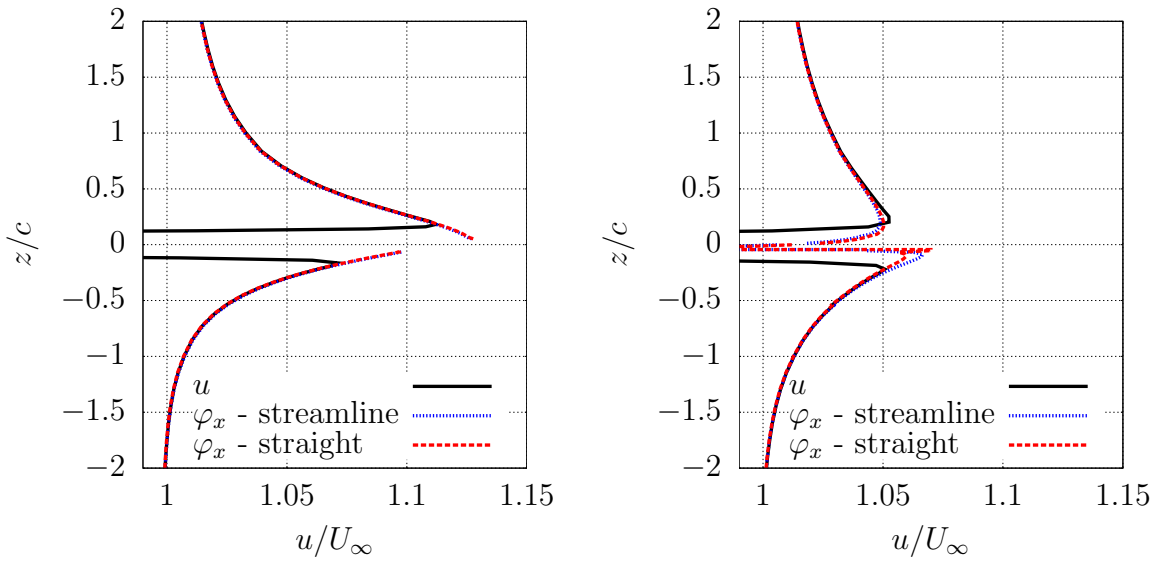

(a) Streamwise velocity at the midchord.

(b) Streamwise velocity at the trailing edge.

Figure 4.23: The effect of the wake surface placement on the streamwise component of the viscous potential compared to the Navier-Stokes result.

The effect of the parameters upon the velocity decomposition approach is measured by calculating the root-mean square error in the streamwise velocity over the midchord and trailing edge sample lines as well as the comparing the lift and drag forces to the Navier-Stokes solution computed on the domain with $x_{\text{extent}}/c = 2000$.

Each of the following plots contains three lines which correspond to three different values of res_{update}. res_{update} controls the threshold minimum initial residual of the momentum equations at which the first, and subsequent, velocity decomposition updates occur in the iterative procedure. A lower value of res_{update} means that the Navier-Stokes sub-problem becomes more converged before the boundary conditions at $\partial\Omega_{\text{E}}$ are updated from the initial inviscid conditions. The $x-$axis corresponds to N_{updates}, the number of velocity decomposition updates that occur in each simulation.

Fig. 4.24 shows the effect of the two parameters on the error in the velocity over the two sample lines. Fig. 4.25 shows the effect of the two parameters on the error in the lift and drag coefficients. All plots show that setting $res_{\text{update}} = 0.01$ is too

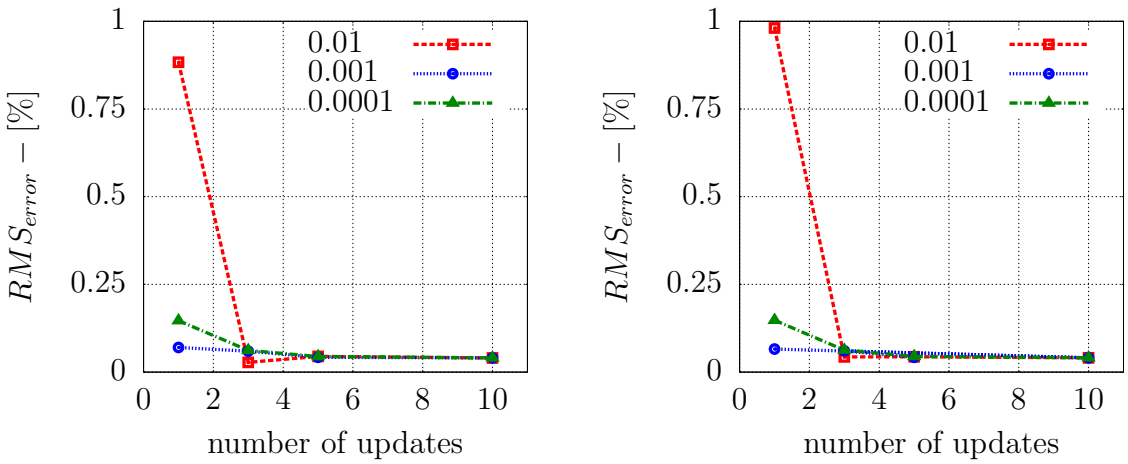

(a) Error in the streamwise velocity at the midchord.

(b) Error in the streamwise velocity at the trailing edge.

Figure 4.24: The effect of res_{update} and N_{updates} on the streamwise component of the total velocity calculated using velocity decomposition compared to a large domain Navier-Stokes solution.

high; the Navier-Stokes solution is not well developed enough at the first update to give correct and meaningful information to the viscous potential. All plots also show that the minimum number of updates used should be five. Similar to the findings in the viscous potential parameter investigation, the numerical scheme used to perform the velocity decomposition simulations is relatively insensitive to the parameters used and that the scheme converges as the various parameters are refined.

4.3.4 Velocity Decomposition

This section demonstrates the ability of the velocity decomposition approach to considerably reduce the domain size of the Navier-Stokes sub-problem while maintaining accuracy in the measured quantities. The same metrics which where used in the Navier-Stokes domain dependence study are used to evaluate the velocity decomposition approach. The Navier-Stokes solution on the domain with $x_{\text{extent}}/c = 2000$ is used as the baseline solution for comparison. The parameters shown in Table 4.5 are used for all simulations in this section. In addition to the velocity decomposition

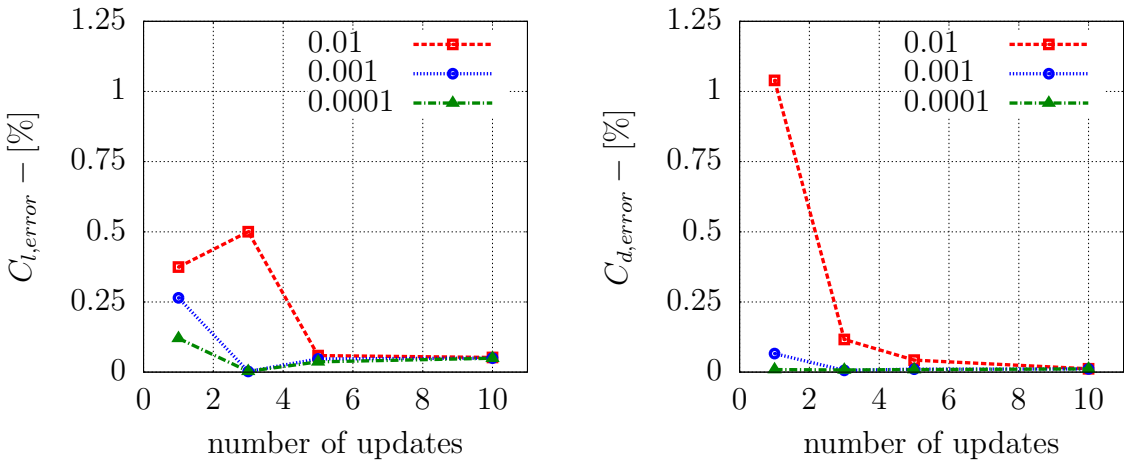

(a) Error in the lift coefficient.

(b) Error in the drag coefficient.

Figure 4.25: The effect of res_{update} and N_{updates} on the lift and drag coefficients calculated using velocity decomposition compared to a large domain Navier-Stokes solution.

parameter	value
$\beta_{\boldsymbol{\omega}}$	0.05
ϵ_{φ}	0.05
l_{wake} / c	10
ζ_{wake}	0.15
wake on streamline?	no
N_{updates}	5
res_{update}	0.001

Table 4.5: The parameter values used in for the velocity decomposition domain dependence investigation.

and Navier-Stokes results, simulations were also run which used the inviscid potential as a boundary condition for the velocity on $\partial\Omega_I$. This is sometimes referred to as the "far-field correction" (Thomas and Salas, 1986) in the literature and is used because it is often a better approximation than simply using the freestream velocity.

Fig. 4.26 shows the error in the lift and drag coefficients compared to the Navier-Stokes solution. The velocity decomposition results give at least an order of magnitude increase (if not better) in accuracy of the measured quantities (C_L, C_D, and RMS_{error} in streamwise velocity) on a similar sized domain compared to the Navier-Stokes simulations. Also, using the inviscid potential as an improved boundary con-

dition achieves a small improvement in the accuracy, but it is not significant. At this low Re of 2000, the flow is strongly separated (as seen in Fig. 4.15) which results in an large loss of lift. The lift coefficient calculated using velocity decomposition on the domain with boundaries at $x_{\text{extent}}/c = 2$ is $C_L = 0.207$ while the inviscid lift coefficient is $C_L = 0.595$ (for reference, the lift coefficient predicted by the $2\pi\alpha$ approximation is $C_L = 0.548$). The use of the inviscid potential as a boundary condition is detrimental because it is applying a velocity field which is predicting over twice the amount of lift present in the real Navier-Stokes solution. The total circulation condition which matches the lift predicted by the viscous potential to the lift present in the Navier-Stokes flow is essential to the accuracy of the velocity decomposition approach in cases of severe loss of lift.

Fig. 4.27 shows the error in the streamwise velocity calculated using the velocity decomposition approach compared to the Navier-Stokes solution and the Navier-Stokes solution using the inviscid potential for boundary conditions on the total velocity. The velocity decomposition results very quickly converge to an extremely high level of accuracy.

The next figures examine the effect of the iterative velocity decomposition approach on the determination of the viscous potential. There are two different approaches used to calculate the viscous potential. The first way is to use a converged Navier-Stokes solution. This is only useful for studying the viscous potential. The second is the velocity decomposition approach where neither the Navier-Stokes solution nor the viscous potential are known ahead of time and are calculated iteratively. The following figures demonstrate that the iterative scheme has very little effect on the final viscous potential.

The two plots in Fig. 4.28 show the root-mean square error in the streamwise component of the viscous potential velocity calculated using the iterative velocity decomposition approach compared to the streamwise component of the viscous po-

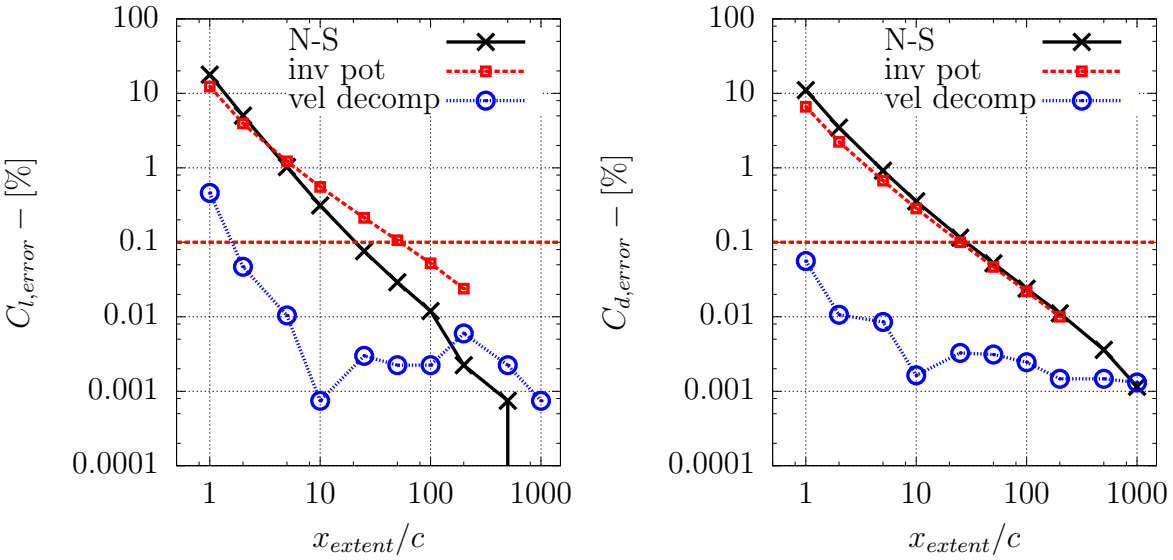

(a) Error in the lift coefficient.

(b) Error in the drag coefficient.

Figure 4.26: The error in the integrated forces on the NACA0012 foil calculated using the iterative velocity decomposition solver compared to the forces calculated from a converged Navier-Stokes solution on a large ($2000c$) domain.

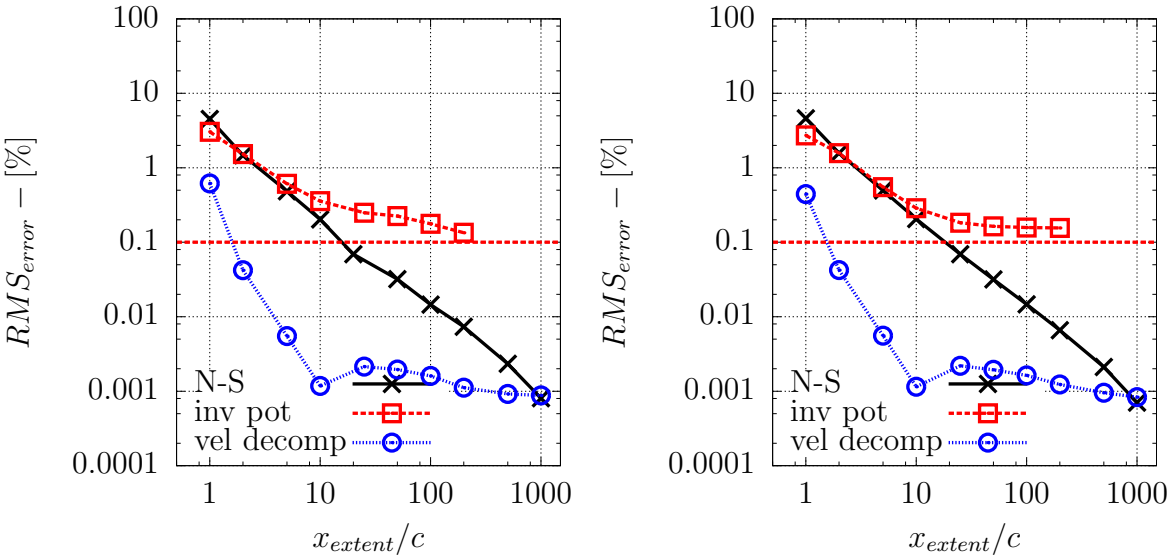

(a) Error in the streamwise velocity on a sample line at the midchord.

(b) Error in the streamwise velocity on a sample line at the trailing edge.

Figure 4.27: Error in the streamwise component of the total velocity calculated using the iterative velocity decomposition solver compared to the streamwise component of the total velocity calculated on a converged Navier-Stokes solution on a large ($2000c$) domain.

tential velocity (*not* the total velocity) calculated from a converged Navier-Stokes solution. The plots show that, for domain sizes which produced accurate results compared the Navier-Stokes solution ($x_{\text{extent}}/c > 1.0$), the iterative scheme reproduces the viscous potential calculated from a converged Navier-Stokes flow to within nearly five significant figures. Therefore, the iterative scheme has little effect on the overall solution.

Fig. 4.29 shows contours of vortical component of velocity, which is calculated as the difference between the total velocity and the velocity potential. Fig. 4.29a shows contours of the vortical component calculated using the inviscid potential while Fig. 4.29b shows contours of the vortical component calculated using the viscous potential. These figures demonstrate that the viscous potential drives the vortical component of velocity to zero much more rapidly than the inviscid potential.

Fig. 4.30 shows the pressure gradient normal to the boundary calculated from the viscous potential on the upper boundary of the reduced domain (from $-2.0 \leq x/c \leq 10.0$ at $z/c = 2.0$). This is used as the Neumann boundary condition for the pressure in the Navier-Stokes sub-problem. The gradient of the pressure field from a large domain Navier-Stokes solution is also included. The Neumann condition calculated from the viscous potential agrees well with the result from the large domain. This shows that the use of a non-zero Neumann condition for the pressure is warranted and that the viscous potential provides the correct value.

Table 4.6 shows the effect of the initial boundary conditions on the reduced domain. The initial condition used in all simulations in this work, $\mathbf{u} = \nabla\Phi$ on $\partial\Omega_{\text{E}}$, is compared to an initial condition of $\mathbf{u} = U_\infty$ on $\partial\Omega_{\text{E}}$ as well as $\mathbf{u} = \nabla\Phi$ on $\partial\Omega_{\text{E}}$ and $\mathbf{u} = \nabla\varphi$ everywhere in the field. The RMS error in the converged streamwise velocity at midchord and the trailing edge is calculated. There is a very small difference between the different initial conditions.

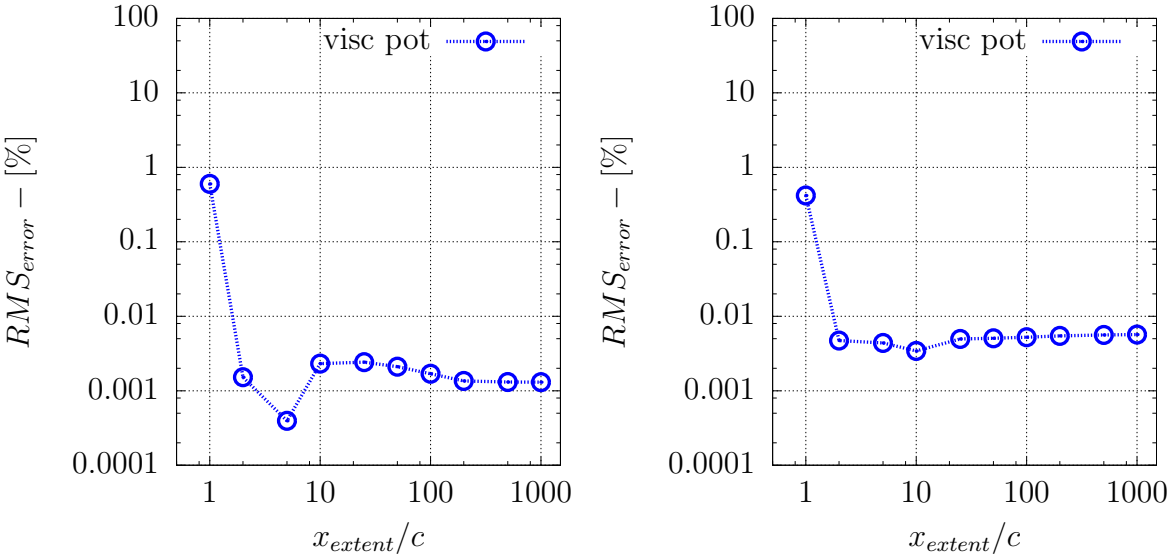

(a) Error in the streamwise velocity on a sample line at the midchord.

(b) Error in the streamwise velocity on a sample line at the trailing edge.

Figure 4.28: Error in the streamwise component of the viscous potential velocity calculated using the iterative velocity decomposition solver compared to the streamwise component of the viscous potential velocity calculated on a converged Navier-Stokes solution on a large ($2000c$) domain.

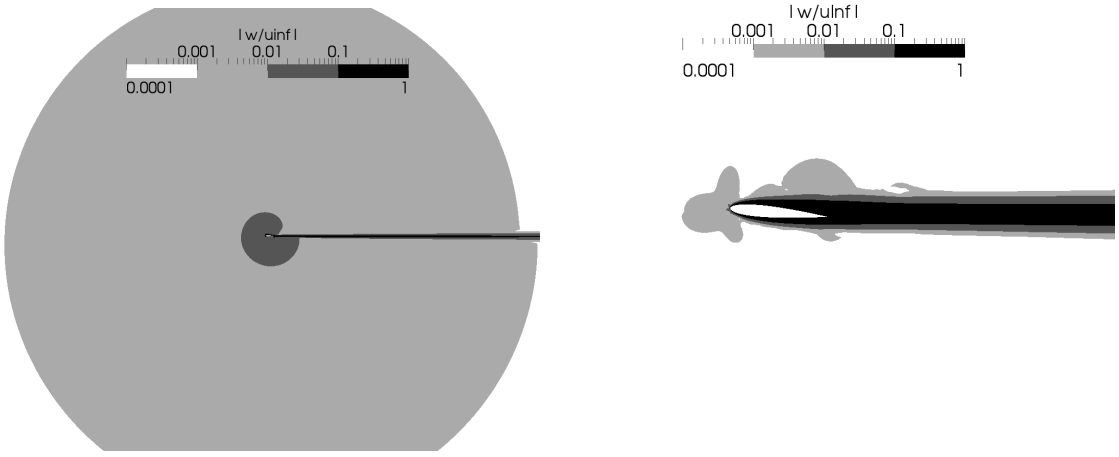

(a) The vortical velocity using the inviscid potential.

(b) The vortical velocity using the viscous potential.

Figure 4.29: A comparison of the inviscid potential and viscous potential by showing contours of the magnitude of the vortical velocity normalized by the freestream velocity.

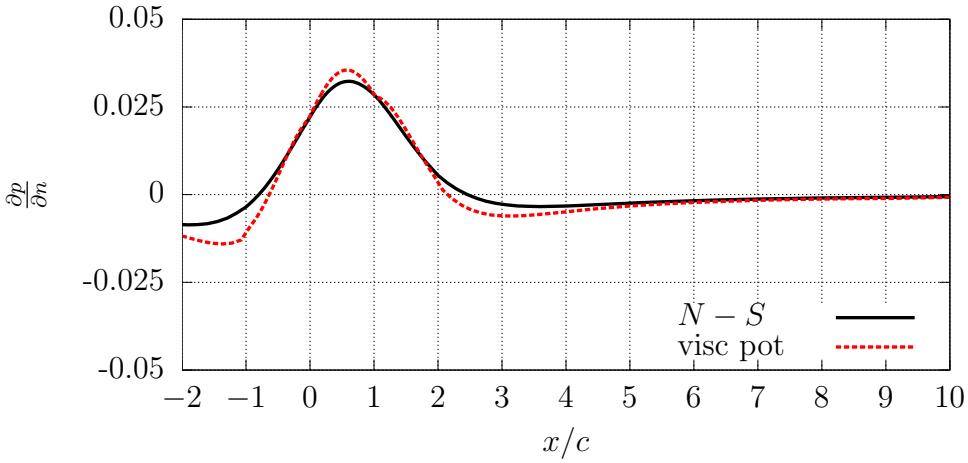

Figure 4.30: The normal pressure gradient on the upper boundary of the reduced domain (from $-2.0 \leq x/c \leq 10.0$ at $z/c = 2.0$) as calculated using the viscous potential compared to the pressure gradient at the same location but calculated from the pressure field on a large domain Navier-Stokes solution.

initial condition	midchord [%]	trailing edge [%]
$\mathbf{u} = \nabla\Phi$ on $\partial\Omega_{\mathrm{E}}$	0.04221	0.04233
$\mathbf{u} = U_\infty$ on $\partial\Omega_{\mathrm{E}}$	0.04006	0.04067
$\mathbf{u} = \nabla\Phi$ on $\partial\Omega_{\mathrm{E}}$ and in the field	0.04295	0.04316

Table 4.6: The RMS error in the converged streamwise velocity at the midchord and trailing edge from three different initial conditions for the total velocity.

	C_L	C_D
Navier-Stokes on $2000c$	0.2064	0.0941
Velocity Decomposition on $5c$	0.2065	0.0941
XFOIL	0.2193	0.0955

Table 4.7: A comparison of the lift and drag coefficients calculated from the Navier-Stokes solver, the velocity decomposition approach, and XFOIL in viscous mode.

4.3.5 Computational Expense

One of the benefits of using velocity decomposition are the large computational savings realized. The time savings of using velocity decomposition on the NACA0012 foil case is described in the following tables. In the following tables, three different levels of accuracy are specified. The domain size which provides the specified level of accuracy in the lift, drag and root-mean square error in velocity is reported for both the Navier-Stokes solver and the velocity decomposition approach. In order to make a fair comparison, all results were computed on grids which are topologically identical in the overlapping regions and were calculated using a single processor on a multiple-core desktop computer.

In Table 4.8 the Navier-Stokes domains required to achieve a 1%, 0.1%, and 0.01% error threshold are shown. Table 4.9 shows the same for the velocity decomposition approach. Finally, Table 4.10 compares the two approaches and the time required to compute the solution which meets that error threshold. The velocity decomposition approach offers a $3 - 7.5\times$ speed-up to achieve an equal level of accuracy because of the drastically smaller domains on which the Navier-Stokes sub-problem is solved.

Another observation that can be made is that, for the domain with inlet boundaries at $x_{\text{extent}}/c = 5$ the difference in computational time is only four seconds. This means that the entire viscous potential calculation (including all five updates and 104 more iterations of the SIMPLE algorithm) required less than four seconds. In other words, for a four second cost in computational time, the use of velocity decomposition will improve the accuracy of the solution by two orders of magnitude in the measured quantities on the domain with $x_{\text{extent}}/c = 5$.

Furthermore, it is likely that by investigating the effect of the outlet and grid stretching (remove the requirement that the grids are topologically similar in overlapping regions), the speed-up of the velocity decomposition approach could be made even more pronounced.

error threshold	domain size [c]	grid points [-]	SIMPLE iters [-]	time [s]
1%	5	20,182	626	92
0.1%	50	45,262	1356	338
0.01%	500	117,526	1859	595

Table 4.8: Computational time required to converge the Navier-Stokes solver in order to achieve three different orders of accuracy in C_L, C_D, and the streamwise velocity over sample lines at the midchord and trailing edge.

error threshold	domain size [c]	grid points [-]	SIMPLE iters [-]	time [s]
1%	1	8,800	738	30
0.1%	2	12,398	738	45
0.01%	5	20,182	730	96

Table 4.9: Computational time required to converge the iterative velocity decomposition solver in order to achieve three different orders of accuracy in C_L, C_D, and the streamwise velocity over sample lines at the midchord and trailing edge.

error threshold	N-S [s]	vel decomp [s]	speed-up [-]
1%	92	30	3.07
0.1%	338	45	7.50
0.01%	595	96	6.20

Table 4.10: A comparison of the time required to converge the velocity decomposition approach to the Navier-Stokes solver.

4.4 Turbulent NACA0012 Foil

In this section the flow over a NACA0012 foil at $\mathrm{Re} = 1.34 \times 10^6$ is studied. For the range of angles of attack initially tested, 8° was the largest at which a steady solution was found. Contours of velocity and vorticity for this case are shown in Fig. 4.31. First, a domain dependence study is performed for the RANS solver. Then, the same is done for the iterative velocity decomposition approach and compared to the RANS result. Finally, the computational time required for the two methods is compared.

4.4.1 RANS Domain Size Study

The domain dependence of the RANS solution is shown in Figs. 4.32 and 4.33. Fig. 4.32 shows the effect of the domain size on the lift and drag coefficients. The convergence in the forces is not as smooth as the laminar case. This is partly due to the large amount of high-aspect ratio cells which are required to correctly capture the thin boundary layer. High aspect ratio cells negatively affect the ability of the RANS solver to converge the RANS equations to a high level of accuracy. Fig. 4.33 shows the root-mean square error in the streamwise velocity over sample lines at the midchord and at the trailing edge. The error in all plots decays steadily as the domain size increases, and it appears that the domain with boundaries at $x_{\mathrm{extent}}/c = 2000$ is sufficiently large enough to be used as a baseline case.

For all domain sizes, the non-dimensional near-wall spacing, y^+, on the body has an average of 48 and a maximum of 158 which is in the acceptable range for the wall function used.

4.4.2 Velocity Decomposition

The velocity decomposition approach is now applied to the turbulent NACA0012 foil at $\alpha = 8°$. The parameters used in the numerical schemes are the same as

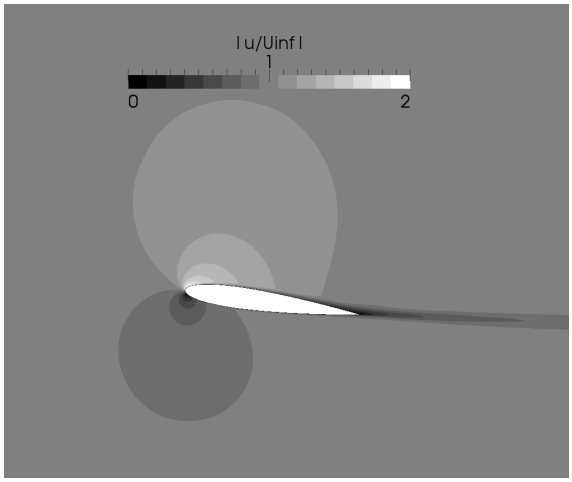

(a) The magnitude of velocity normalized by the freestream velocity.

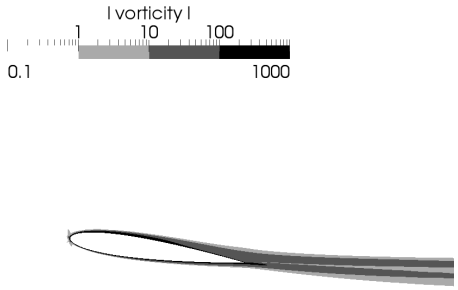

(b) The magnitude of the vorticity.

Figure 4.31: Contours of velocity and vorticity for the flow over the NACA0012 at $\mathrm{Re} = 1.34 \cdot 10^6$ and $\alpha = 8°$.

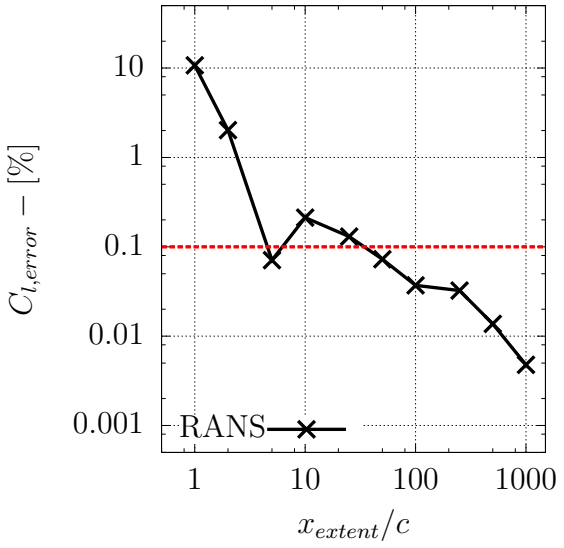

(a) Error in the lift coefficient.

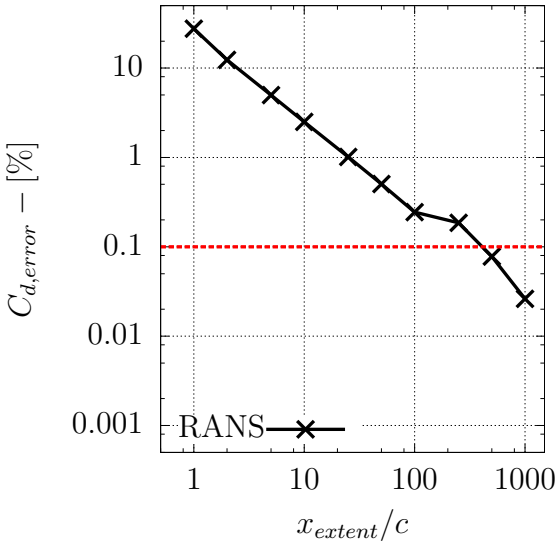

(b) Error in the drag coefficient.

Figure 4.32: The effect of reducing the domain size on the components of the integrated force on the NACA0012 foil at $\mathrm{Re} = 1.34 \cdot 10^6$ at $\alpha = 8°$.

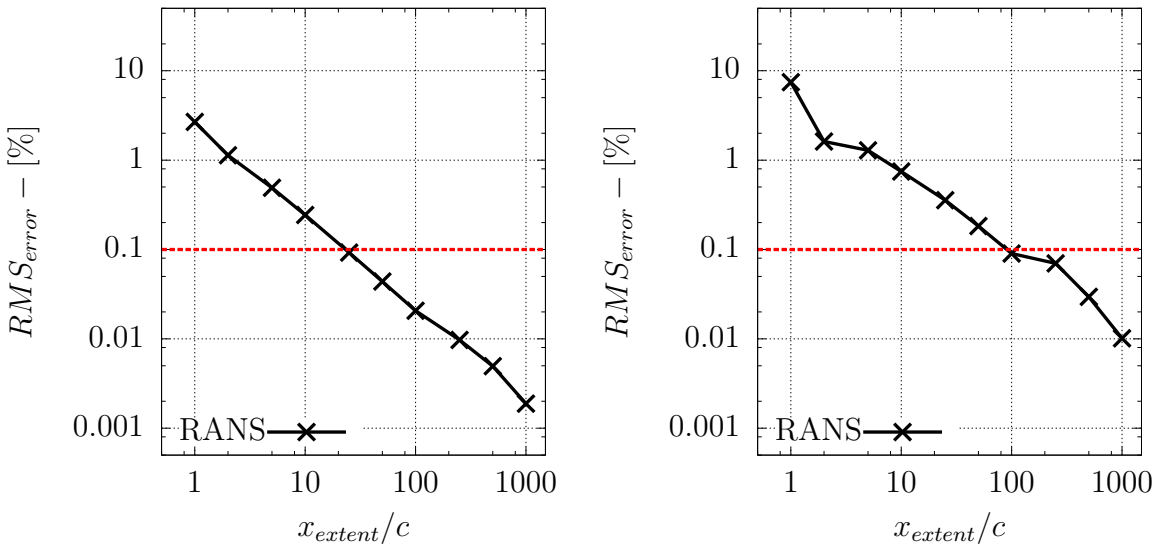

(a) Error in the streamwise velocity at the midchord.

(b) Error in the streamwise velocity at the trailing edge.

Figure 4.33: The effect of reducing the domain size on the streamwise component of velocity over two sample lines on the NACA0012 foil at $\mathrm{Re} = 1.34 \cdot 10^6$ at $\alpha = 8°$.

those used in the laminar case given in Table 4.5. The velocity decomposition approach is compared to the RANS solutions in the same manner as the laminar case. Fig. 4.34 shows the error in the lift and drag coefficients compared to the RANS solution solution calculated on a domain with $x_{\text{extent}}/c = 2000$. The domain with size $x_{\text{extent}}/c = 25$ has a predicted drag value equal to the drag predicted by the large domain RANS solution, this is coincidental. Fig. 4.35 shows the root-mean square error in the streamwise velocity over sample lines at the midchord and trailing edge. In all plots the error in the velocity decomposition simulations is less than the RANS solution.

Fig. 4.36 shows contours of vortical component of velocity, which is calculated as the difference between the total velocity and the velocity potential. Fig. 4.36a shows contours of the vortical component calculated using the inviscid potential while Fig. 4.36b shows contours of the vortical component calculated using the viscous potential. The difference is not as pronounced as the laminar case, but still shows the

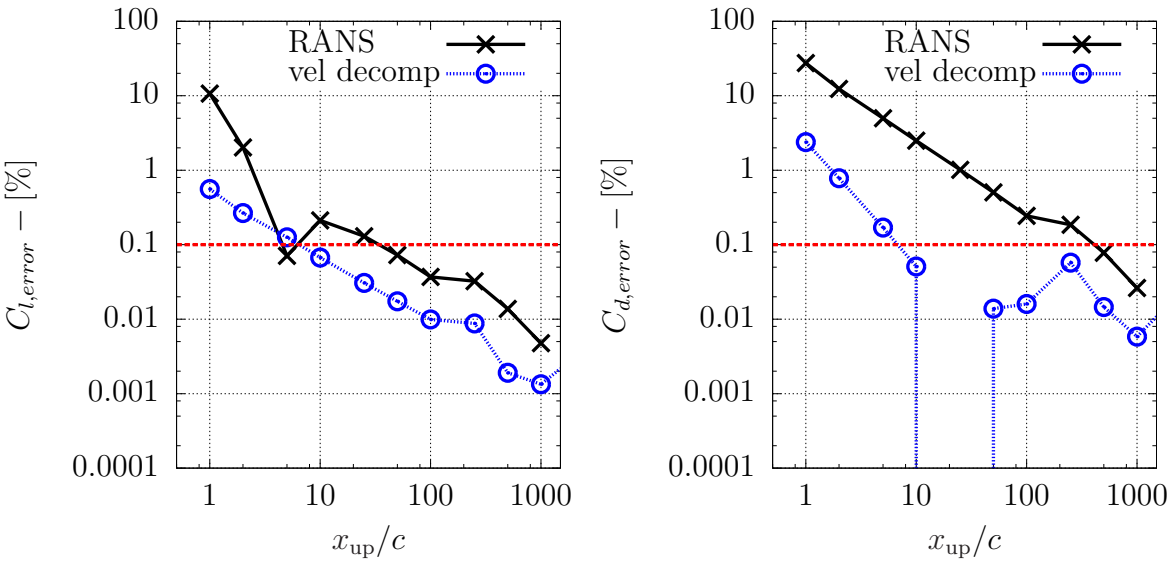

(a) Error in the lift coefficient.

(b) Error in the drag coefficient.

Figure 4.34: The error in the integrated forces on the NACA0012 foil calculated using the iterative velocity decomposition solver compared to the forces calculated from a converged Navier-Stokes solution on a large ($2000c$) domain.

remarkable improvement of the viscous potential over the inviscid potential. These figures show that the viscous potential drives the vortical component of velocity to zero much more rapidly than the inviscid potential.

The velocity decomposition approach does not give as much advantage in accuracy for the same domain size as it did in the laminar case. It is hypothesized that the larger gradients in the pressure field limit the domain reduction in these high-lift situations. It is doubtful that the calculation of the viscous potential is to blame because the viscous potential *does* satisfy the Navier-Stokes problem outside of the vortical regions (where $\mathbf{w}$ is negligible) to within less than 1% of the free-stream value as shown in Fig. 4.36b.

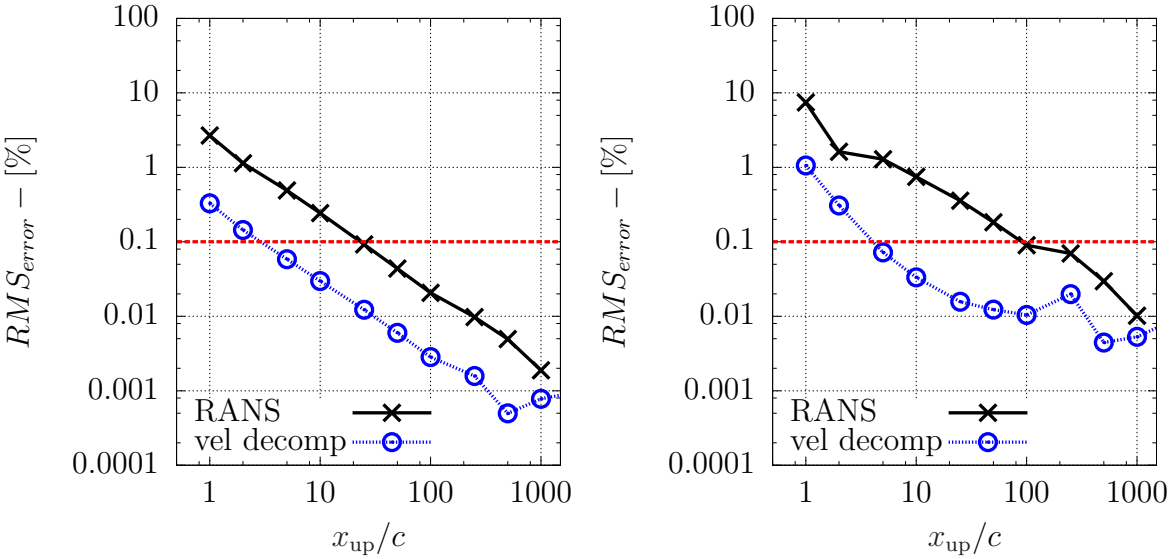

(a) Error in the streamwise velocity on a sample line at the midchord.

(b) Error in the streamwise velocity on a sample line at the trailing edge.

Figure 4.35: Error in the streamwise component of the total velocity calculated using the iterative velocity decomposition solver compared to the streamwise component of the total velocity calculated on a converged Navier-Stokes solution on a large ($2000c$) domain.

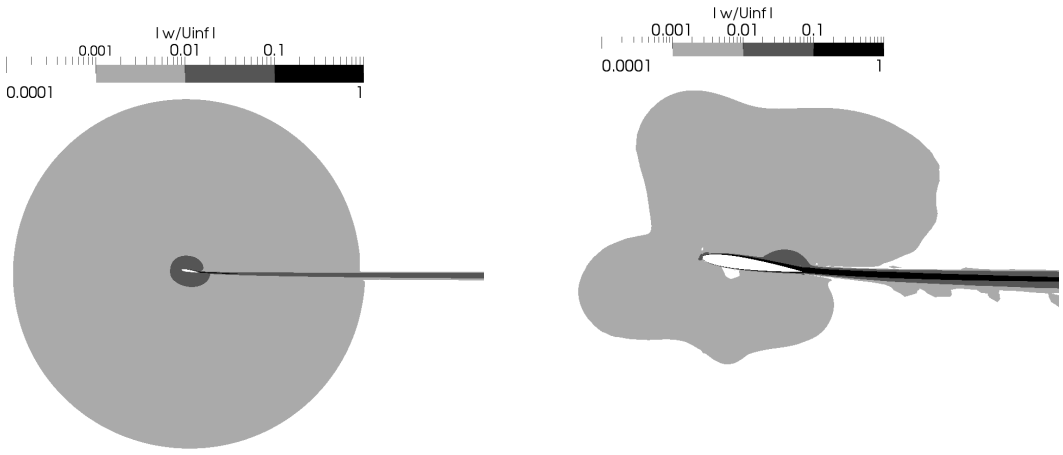

(a) The vortical velocity using the inviscid potential.

(b) The vortical velocity using the viscous potential.

Figure 4.36: A comparison of the inviscid potential and viscous potential by showing contours of the magnitude of the vortical velocity normalized by the freestream velocity.

4.5 Summary

In this chapter, results were presented using the velocity decomposition approach to solving the Navier-Stokes problem for lifting flows. First, the wake model to capture asymmetry in the wake region using coincidentally located source and dipole panels was evaluated. This approach was applied to the case of a flat plate with different boundary layers above and below the plate. The viscous potential was able to satisfactorily match the real viscous flow for all cases.

The velocity decomposition approach was then used to calculate the flow over a NACA0012 at two different Re's and angles of attack. The velocity decomposition approach gave remarkable results for the laminar case which included separation and significant loss of lift. In this case, the total circulation condition is essential to the high level of accuracy of the solution from the velocity decomposition approach. A Navier-Stokes domain with $x_{\text{extent}}/c = 2.0$ gave an error of less than 0.1% in the RMS_{error} and lift and drag coefficients. This is a large improvement over the larger domains ($> 50c$) recommended by Thomas and Salas (1986) and Rumsey and Ying (2002) when using $\mathbf{u} = \nabla\Phi$ on $\partial\Omega_I$. The speedup in these calculations ranged from $3-7.5\times$. Although it seems that the velocity decomposition approach gives a suitable viscous potential, the results for the turbulent case were good, but not as impressive.

Considering the deeply-submerged cylinder results from Edmund (2012) briefly discussed in Section 2.2, the velocity decomposition approach is able to solve problems with massive amounts of separation. Furthermore, given the results of the NACA0012 at $\text{Re} = 2000$ and $\alpha = 5°$, the velocity decomposition approach is also able to accurately calculate lifting problems with moderate loss of lift. The applicability of velocity decomposition for lifting problems seems only limited to the existence of steady solutions.

The use of velocity decomposition for lifting problems is preferred over a coupled inviscid / viscous solution technique like that used in XFOIL. The approach used

to model the boundary layer in XFOIL only allows for limited separation, while the velocity decomposition approach has been shown to work for separated flows. Futhermore, the velocity decomposition approach is a very flexible approach which is extendable to more complex problems; as shown in the next chapter, free-surface effects are included in a straightforward manner. The approach could also be extended to include multiple bodies.

CHAPTER 5

Free-surface Flow

In this chapter the velocity decomposition approach is applied to free-surface problems. The body is fully submerged in all cases presented and all free-surface effects are included through the linear free-surface condition in the viscous potential.

Before results are presented, the linear free-surface solver is validated for a variety of cases. Then, the velocity decomposition approach is applied to the flow over a bottom-mounted bump. Finally, the velocity decomposition approach is applied to the flow over a submerged foil at $\alpha = 0°$.

5.1 Validation of the Velocity Potential for Free-surface Flow

The free-surface solver is validated in a number of steps. First, the solver is validated for the cases of flow over a submerged point vortex. The effect of the location of the upstream and downstream free-surface boundaries is investigated for the flow over the point vortex. The effect of the number of collocation points (equal to the number of free-surface point sources) per fundamental wavelength, N_λ, is also investigated. The free-surface solver is then validated for the case of the flow over a submerged cylinder with and without circulation. The final validation case is that of a thick foil at $\alpha = 0°$.

Fig. 5.1 shows the computed free-surface elevation for a point vortex with strength $\Gamma/2\pi = 2.7$, located at 4.5 ft below the mean free surface, with a freestream velocity of $U_\infty = 10$ ft/s. The calculated free-surface elevation compares very well with the linear free-surface calculations from Salvesen and Von Kerczek (1975) for the same case.

The free-surface solver is first validated for the flow over a point vortex. In these cases, unless it is otherwise stated, the free-surface parameters are $x_{\text{up}}/\lambda_0 = 16$, $x_{\text{down}}/\lambda_0 = 24$, and $N_\lambda = 48$. Fig. 5.2 shows the effect of the location of the downstream boundary on the free-surface elevation for the flow over a point vortex. The location of the downstream boundary has little effect on the solution, except for the 3λ case where the final crest is slightly over-predicted because it is very near the downstream boundary.

Fig. 5.3 shows the effect of the location of the upstream boundary on the free-surface elevation for the flow over a point vortex. The location of the upstream boundary also has little effect on the solution. The only small issue is the case of 2λ where there is a slight disagreement. In this case the free-surface radiation condition is applied too close to the disturbance.

Fig. 5.4 shows the effect of the number of collocation points (and desingularized sources) per wavelength, N_λ, on the free-surface elevation. It is very clear from this plot that using 12 points per wavelength does not give an acceptable solution, anything more than that is enough. It is interesting to note that the 96 points per wavelength calculation required that the sources above the free surface be moved closer to the collocation points because the conditioning of the matrix became poor due to the relative proximity of the point sources to each other.

Next, the linear free-surface solver is verified for the case of a submerged circular cylinder. Eq. (5.1) is an analytical expression from Kochin et al. (1964) for far-field

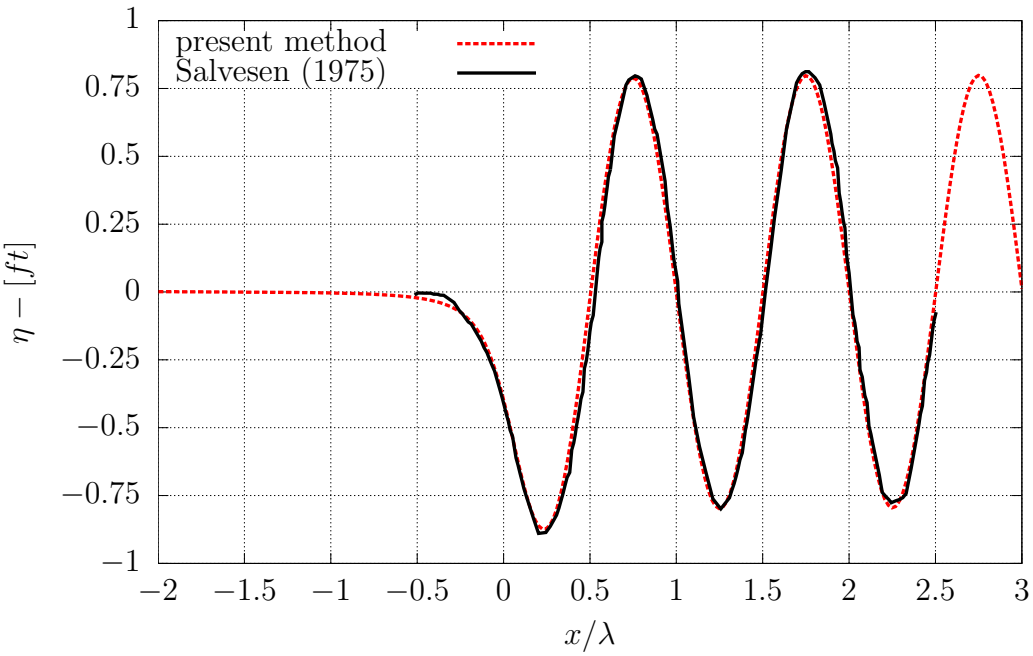

Figure 5.1: The free-surface elevation due to a point vortex located at $(x, z) = (0, -4.5)$ with strength $\Gamma/2\pi = 2.7$ at $h = 4.5$ ft with $U_\infty = 10$ ft/s compared to the linear result from Salvesen and Von Kerczek (1975).

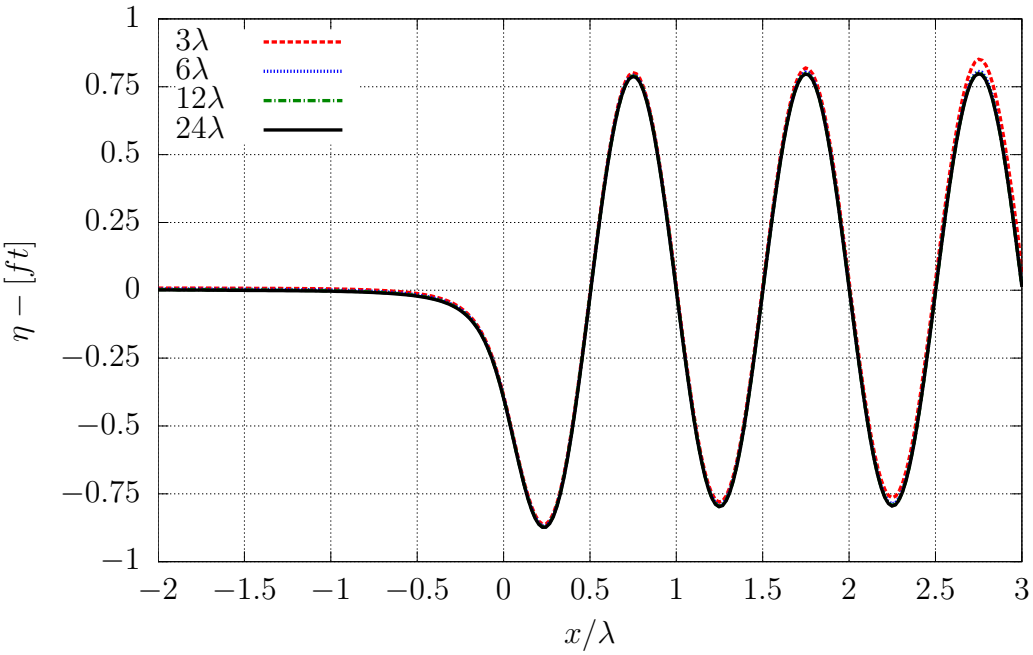

Figure 5.2: The effect of the location of the downstream boundary on the free-surface elevation due to a submerged point vortex with strength $\Gamma/2\pi = 2.7$ at $h = 4.5$ ft with $U_\infty = 10$ ft/s.

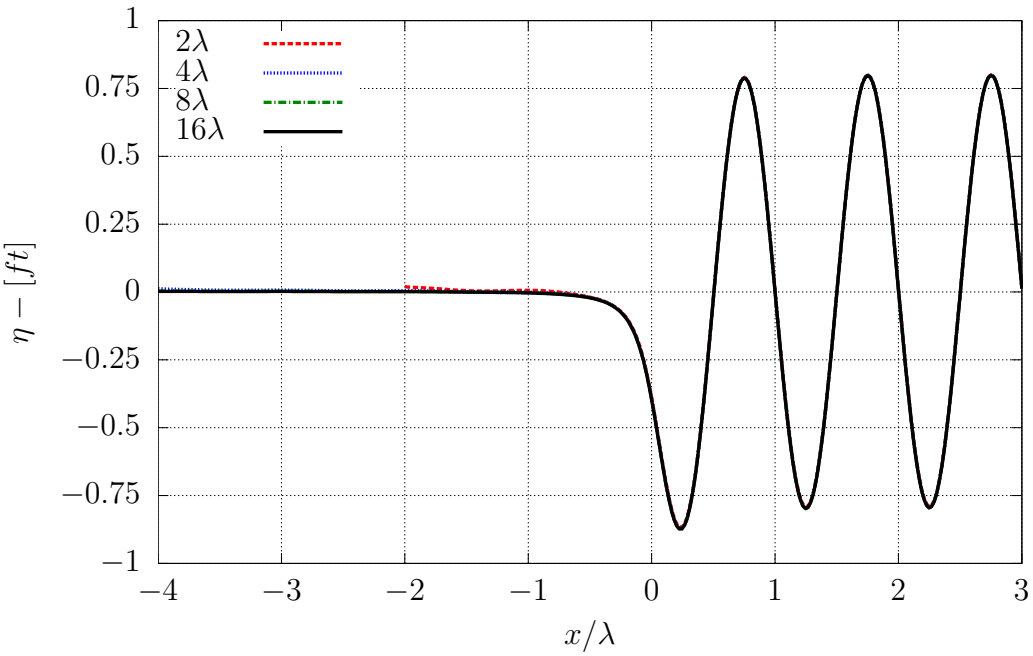

Figure 5.3: The effect of the location of the upstream boundary on the free-surface elevation due to a submerged point vortex with strength $\Gamma/2\pi = 2.7$ at $z = -4.5$ ft with $U_\infty = 10$ ft/s.

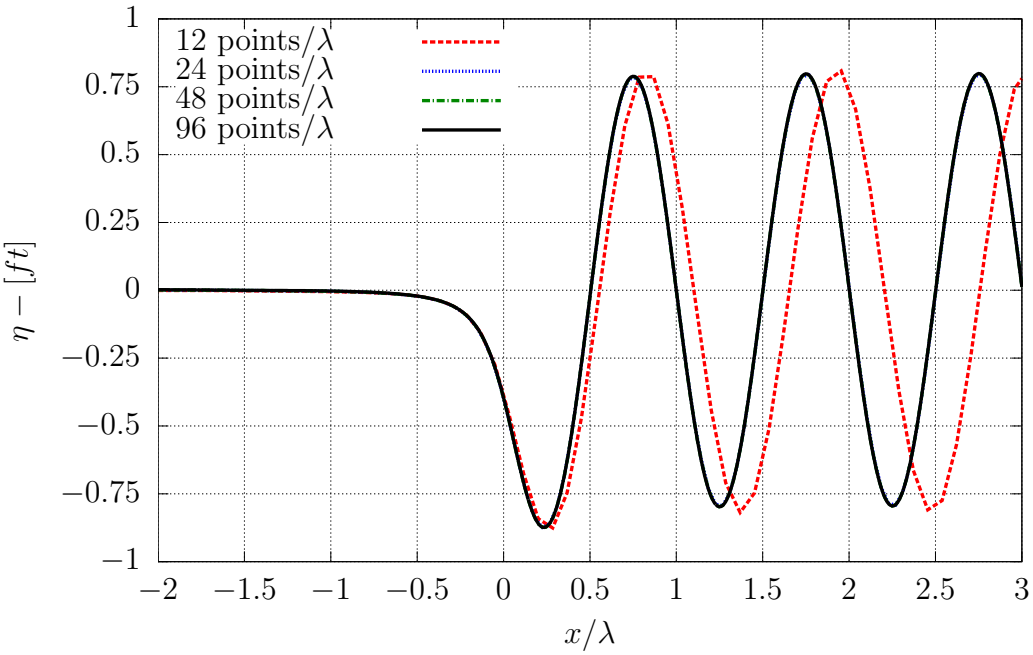

Figure 5.4: The effect of the number of sources per wavelength on the free-surface elevation due to a submerged point vortex with strength $\Gamma/2\pi = 2.7$ at $z = -4.5$ ft with $U_\infty = 10$ ft/s.

Γ	analytical $[m]$	present method $[m]$
0.00	0.040	0.040
0.25	0.065	0.065
0.50	0.090	0.090
0.75	0.115	0.116
1.00	0.140	0.141

Table 5.1: The free-surface wave amplitude due to a submerged cylinder with circulation Γ calculated analytically following Kochin et al. (1964) and calculated using the linear free-surface solver.

wave amplitude resulting from the flow over a circular cylinder with circulation Γ.

$$A = \frac{2}{U_\infty}\left(\Gamma + \frac{2\pi g r^2}{U_\infty}\right) e^{-gh/U_\infty} \tag{5.1}$$

Where r is the radius of the cylinder, and h is the depth of submergence. Table 5.1 compares the analytical result with the result from the current method for a circular cylinder of radius 0.25 m submerged 3.0 m below the mean free-surface, measured to the center of the cylinder. The freestream velocity is $U_\infty = 1.0$ m/s, gravity is set to $g = 1.0$ m/s^2, the location of the upstream boundary is $x_{\text{up}} = -60.0$ m, the location of the downstream boundary is $x_{\text{down}} = 60.0$ m, and $N_\lambda = 48$. The surface of the cylinder was discretized using flat, linearly varying vortex panels and the total circulation condition was used to provide the specified circulation around the cylinder. The agreement is very good.

Next, the free-surface elevation is calculated for the same circular cylinder case. The body is represented using flat constant strength source panels, constant strength dipole panels, and linearly varying vortex panels as well as a point dipole. The strength of the point dipole was set to model a circular cylinder of the same radius in an infinite fluid. This is simply a check to make sure that the influence coefficients for the different panels on the free-surface boundary condition are calculated correctly.

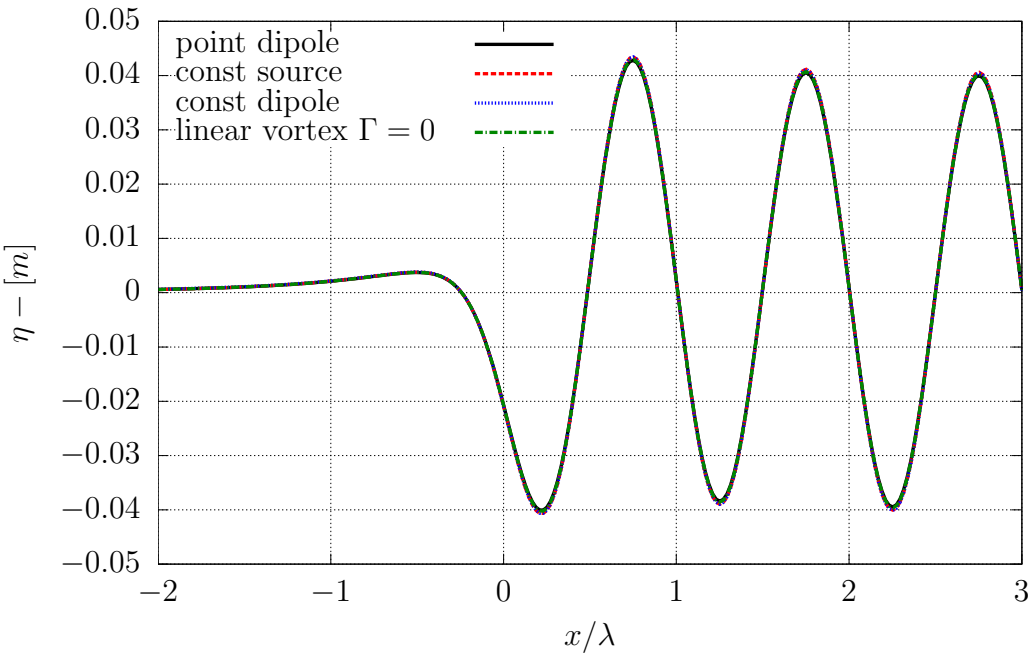

Figure 5.5: A comparison of the free-surface elevation due to a submerged circular cylinder represented using three different singularity elements as well as a submerged point dipole of equivalent strength.

There in no distinguishable difference between the free-surface elevations predicted.

Next, the free-surface solver is validated for the case of a symmetric Joukowski foil with $t/c = 0.12$ with $\alpha = 5°$ with the trailing edge located at $h/c = 1.0$ and $\mathrm{Fn_c} = \mathrm{Fn_h} = 0.95$ ($c = 1.0$ m, $U_\infty = 0.95$ m/s, $g = 1.0$ m/s^2). Fig. 5.6 compares the calculated free-surface elevation to linear calculations from Bai and Han (1994) and Bal and Kinnas (2002). Fig. 5.7 shows the pressure coefficient on the body compared to experimental and numerical results from Bai and Han (1994) and numerical results from Bal and Kinnas (2002). Again, the agreement is quite good.

Finally, the free-surface solver is validated against the numerical results from Salvesen (1966). The Salvesen case was chosen for validation because it is also used in the velocity decomposition results. In this case, there is a thick ($t/c = 0.375$) foil at $\alpha = 0°$ submerged beneath the free surface. The chord length is $c = 1.0$ ft, the free-stream velocity is $U_\infty = 1.0$ ft/s, with $g = 32.2$ ft/s^2, and $h/c = 1.25$.

The free-surface elevation is calculated for two situations and compared to the

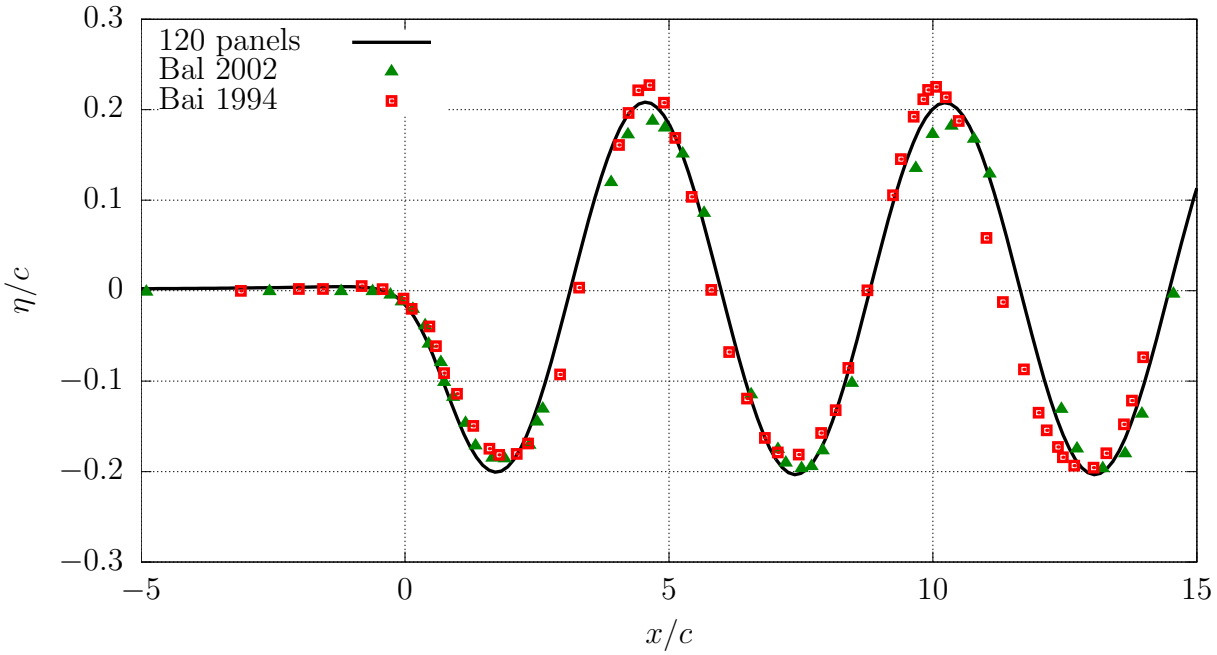

Figure 5.6: The free-surface elevation due to a submerged Joukowski foil at $\alpha = 5°$, $h/c = 1.0$, and $\mathrm{Fn_c} = \mathrm{Fn_h} = 0.95$ compared to Bal and Kinnas (2002) and Bai and Han (1994).

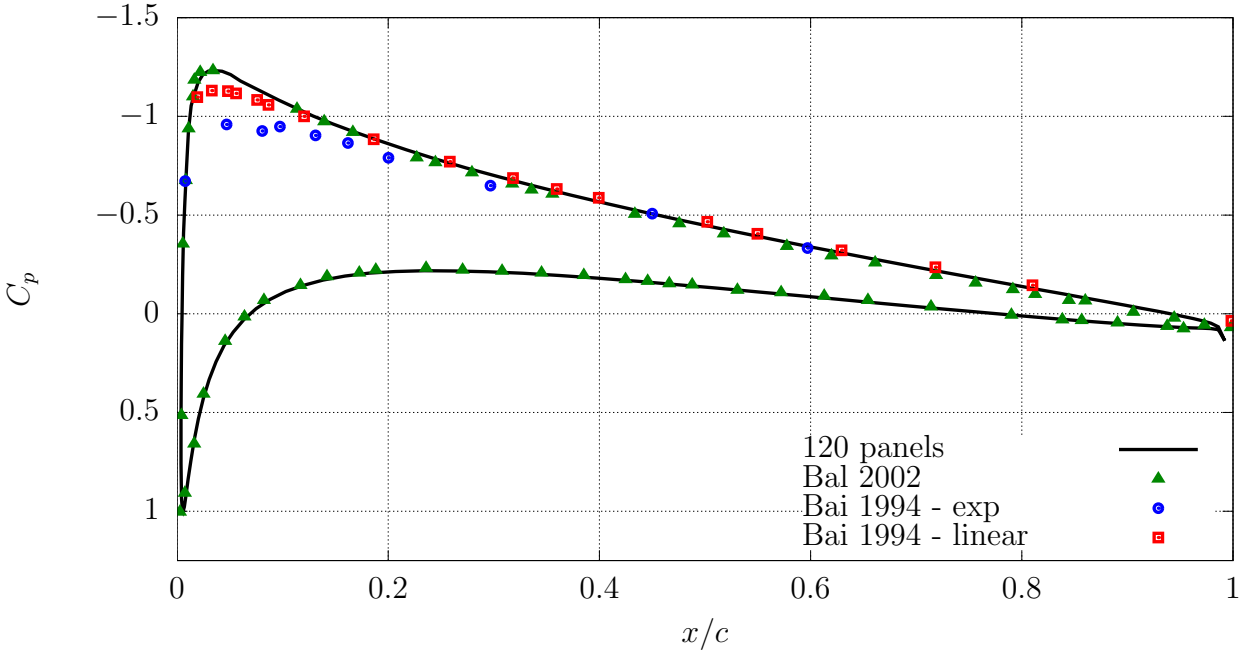

Figure 5.7: C_p on body of the submerged Joukowski foil compared to Bal and Kinnas (2002) and Bai and Han (1994).

linear result given from Salvesen (1966). Fig. 5.8 shows the calculated free-surface elevation for a case where $h/c = 1.25$ and $\mathrm{Fn_c} = 0.62$ ($\mathrm{Fn_h} = 0.55$). Fig. 5.9 shows the calculated free-surface elevation for a case where $h/c = 1.5$ and $\mathrm{Fn_c} = 0.97$ ($\mathrm{Fn_h} = 0.79$). The agreement to the numerical result from Salvesen (1966) is quite good considering that there is likely some error in reproducing the data from the original paper.

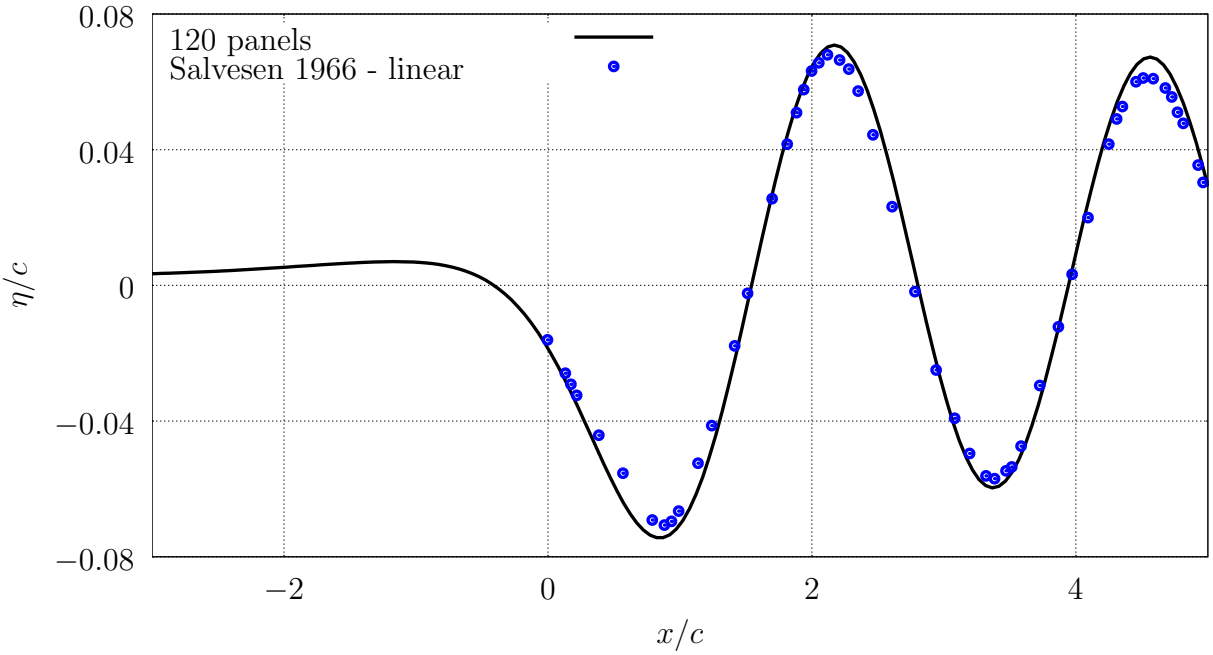

Figure 5.8: The free-surface elevation due to a submerged symmetrical foil at $\alpha = 0°$, $h/c = 1.25$, and $\mathrm{Fn_c} = 0.62$ compared to Salvesen (1966).

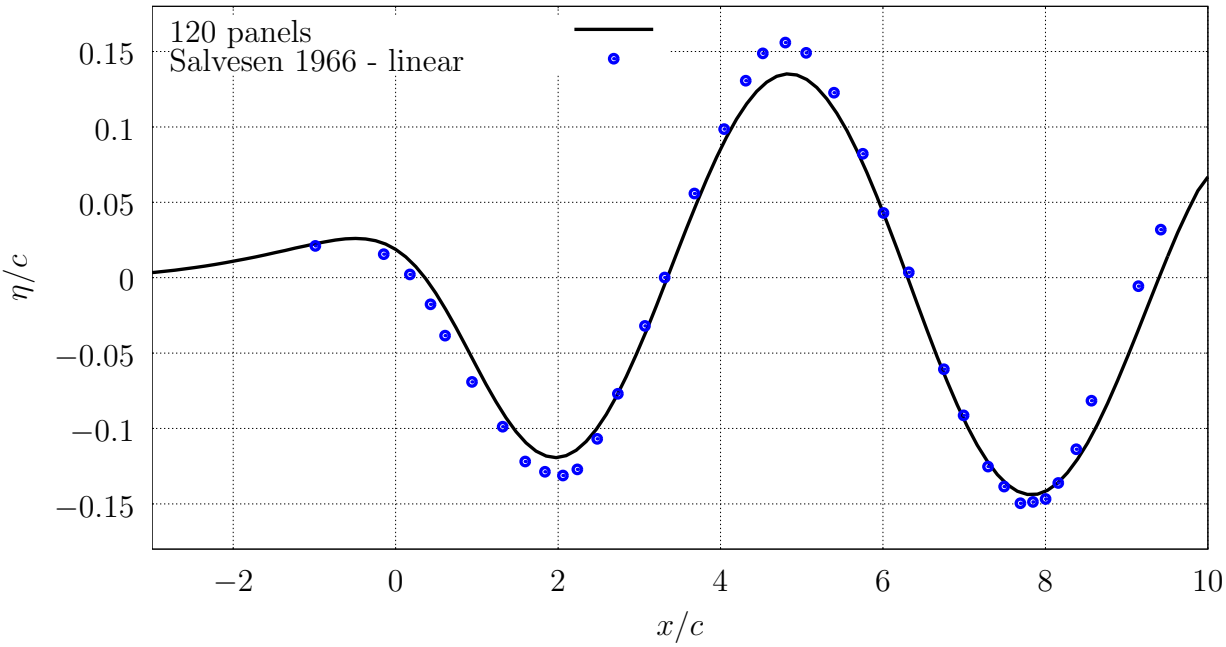

Figure 5.9: The free-surface elevation due to a submerged symmetrical foil at $\alpha = 0°$, $h/c = 1.5$, and $\mathrm{Fn_c} = 0.97$ compared to Salvesen (1966).

5.2 Bottom-mounted Bump

A bottom-mounted bump is the first case that velocity decomposition for free-surface flow is applied to. The setup will mirror the experiments in Cahouet (1984). The geometry of the bump is defined mathematically in Eq. (5.2).

$$z(x) = \frac{27}{4}\frac{H}{L^3}x(x-L)^2 \quad \text{for} \quad 0 \leq x \leq L \tag{5.2}$$

Where $L = 0.42\ m$ is the length of the bump, $H = 0.042\ m$ is the maximum height of the bump. The z-coordinate is translated vertically as needed to achieve the correct submergence depth, h. Fig. 5.10 shows the location and size of the bump relative to the calculated linear free surface.

The velocity decomposition approach is used to calculate the free-surface elevation over the bump for two different pairs of $\mathrm{Fn_h}$ and H/h. The velocity decomposition

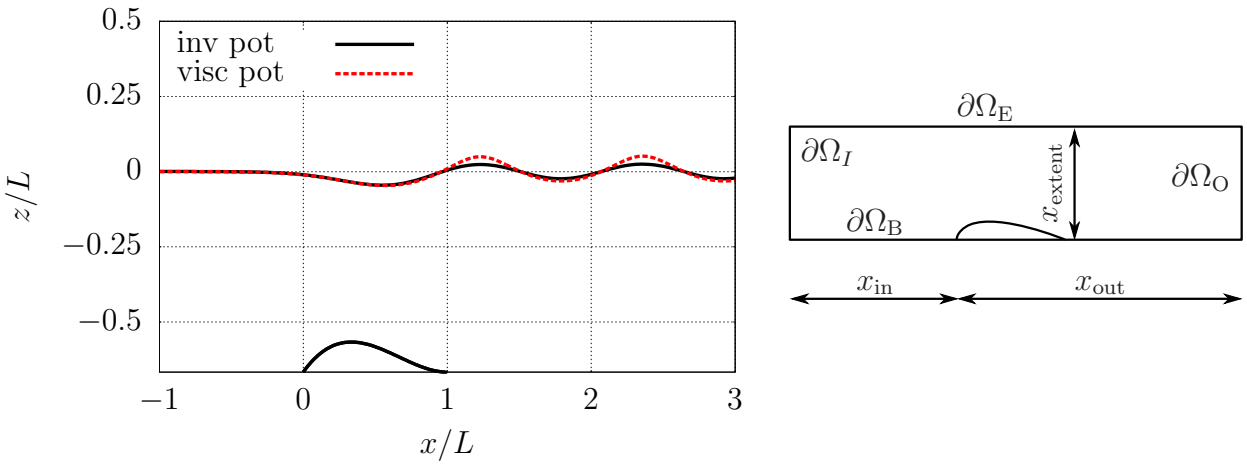

(a) The location and size of the bump relative to the calculated free-surface elevation for the case where $\mathrm{Fn_h} = 0.52$ and $H/h = 0.15$.

(b) The Navier-Stokes sub-domain.

Figure 5.10: The body definition and domain of the Navier-Stokes sub-problem for the bottom-mounted bump.

parameters used for all simulations have the same value as those used in the previous chapter. In the free-surface velocity decomposition simulations, the domain of the Navier-Stokes sub-problem only includes the region near the body; all free-surface effects are included through the velocity potential. The vorticity generated at the free surface is neglected in the current work. For accurate calculation of the boundary conditions on $\partial\Omega_\mathrm{E}$, it is important that the free surface in the viscous potential fully cover the Navier-Stokes domain.

The domain of the Navier-Stokes sub-problem is rectangular with $x_\mathrm{in} = 10L$, $x_\mathrm{out} = 13L$, and $x_\mathrm{extent} = 0.36L$ vertically from the bottom boundary to $\partial\Omega_\mathrm{E}$ as shown in Fig. 5.10. The Navier-Stokes domain is fully submerged. There is a measured upstream velocity profile given in Cahouet (1984), but the location at which the profile was measured is not clear. In place of using the experimental velocity profile, the free-stream velocity is prescribed at the inlet and the no-slip condition is applied to the entire bottom boundary.

Fig. 5.11 shows the calculated free-surface elevation for the $\mathrm{Fn_h} = 0.52$ $H/h =$

0.15 case. The wave steepness, s, is $s_{exp} \approx 1/10$ for the experimental result while the viscous potential result is $s_\varphi \approx 1/14$. This is the shallower of the two submergences tested. The nonlinear result shown is an inviscid nonlinear result also from Cahouet (1984). The viscous potential result satisfactorily predicts the wave amplitude, but is off in the phasing. Fig. 5.12 shows the streamlines for the of the flow over the bump overlaid on contours of the pressure field normalized by the stagnation pressure for the same case. The effect of the free-surface can be seen in both the streamlines and pressure field.

Fig. 5.13 shows the calculated free-surface elevation for the $\mathrm{Fn_h} = 0.43$ $H/h = 0.2$ case. The wave steepness is $s_{exp} \approx 1/9$ for the experimental result, while the viscous potential result gives waves with steepness, $s_\varphi \approx 1/35$. The bump is submerged deeper in this case than the previous case. The free-surface waves are even more steep in this case. Although the viscous potential does increase the amplitude of the waves, the linear free-surface condition is not sufficient.

In both cases presented here, the nonlinear result gives much better agreement than the linear viscous potential result. This suggests that it is more important to include free-surface nonlinearities than viscous effects on the body when modelling the free-surface and including free-surface effects in a problem. However, if linear theory is an acceptable assumption to make, the use of velocity decomposition to include free-surface effects can provide a tremendous computational advantage. Each simulation above required only 10 minutes of computational time on a single processor. In contrast, the time required to achieve a converged steady solution by solving the RANS equations with an interface capturing technique could require hours of computational time.

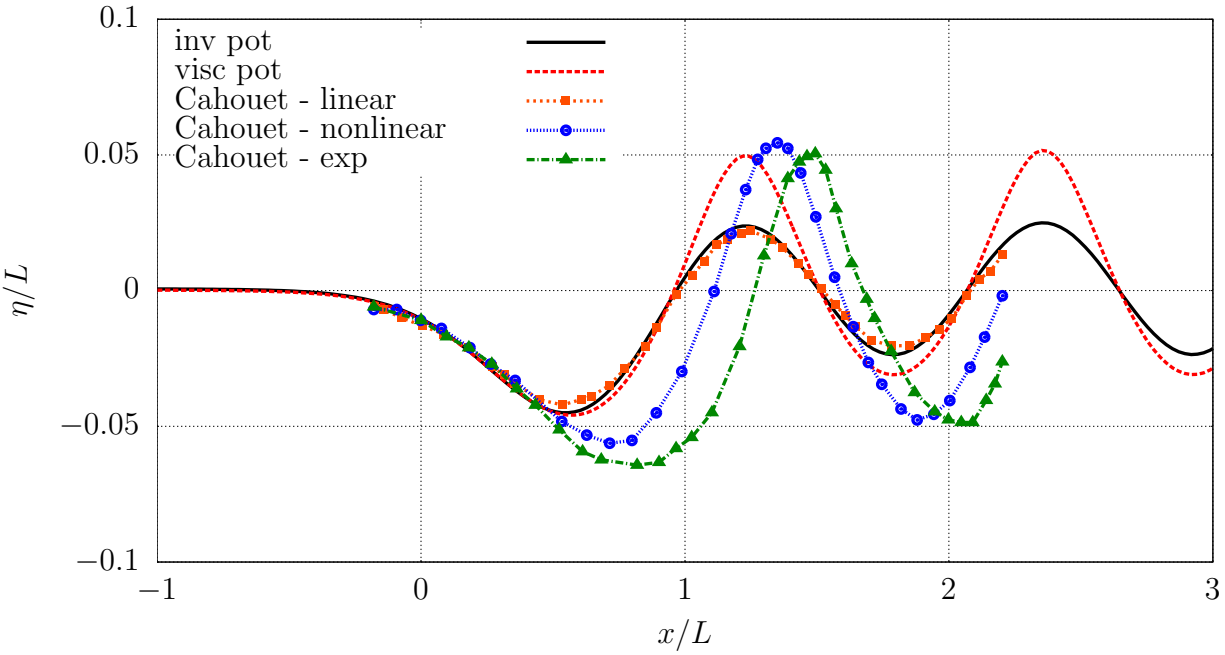

Figure 5.11: Calculated and experimental free-surface elevation for the bottom mounted bump with: $\mathrm{Fn_h} = 0.52$, $H/h = 0.15$, $\mathrm{Re} = 358000$, $s_{exp} \approx 1/10$, $s_{\varphi} \approx 1/14$

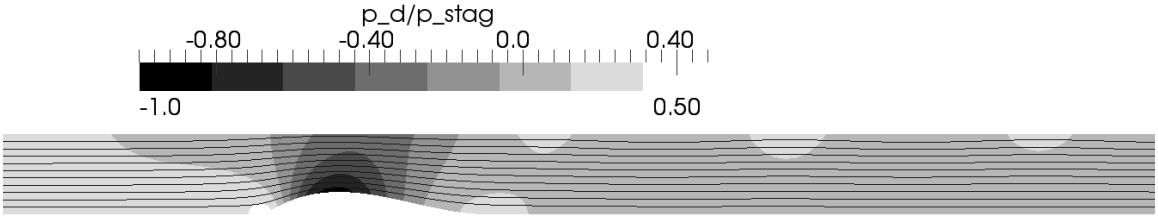

Figure 5.12: Streamlines (in white) overlaid on contours of pressure for the $\mathrm{Fn_h} = 0.52$, $H/h = 0.15$ case.

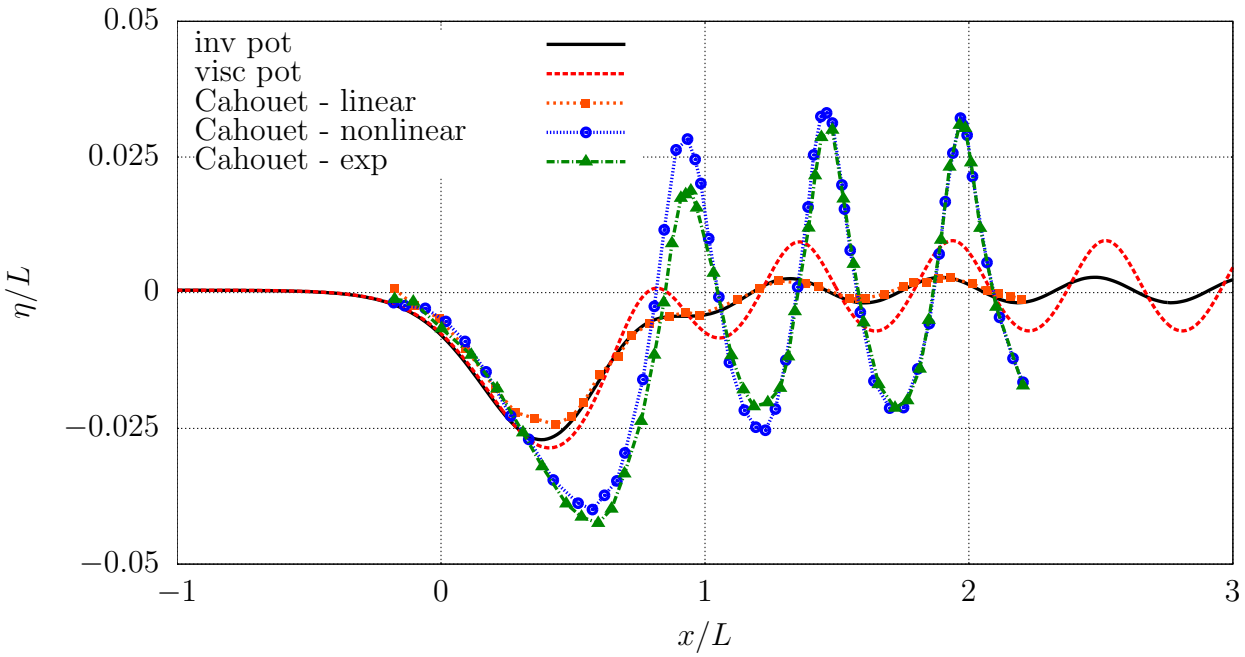

Figure 5.13: Calculated and experimental free-surface elevation for the bottom mounted bump with: $\mathrm{Fn_h} = 0.43$, $H/h = 0.2$, $\mathrm{Re} = 257000$, $s_{exp} \approx 1/9$, $s_{\varphi} \approx 1/35$.

5.3 Salvesen Foil

Finally, the velocity decomposition approach is applied to the fully submerged thick foil at $\alpha = 0°$ from Salvesen (1966). The shape of the foil is defined in Fig. 5.14. The foil location under the free surface as well as the definition of the Navier-Stokes domain are shown in Fig. 5.15. Salvesen (1966) gives experimental free-surface elevations as well as first- and second-order calculations for three different submergences at a range of $\mathrm{Fn_c}$'s. The two deepest submergences, $h/c = 1.25$ and $h/c = 1.5$, are used to evaluate the velocity decomposition approach for free-surface flow. The shallowest submergence, $h/c = 1.0$ was not used because breaking waves were present in the experiments for three values of $\mathrm{Fn_c}$.

The computational domain of the Navier-Stokes sub-problem extends from $x_{\mathrm{in}} = 1c$ to $x_{\mathrm{out}} = 40c$ with the lateral boundary located at $x_{\mathrm{extent}} = 1c$ from the body.

The parameters which control the velocity decomposition scheme and determination of the viscous potential have the same values as those in the previous chapter.

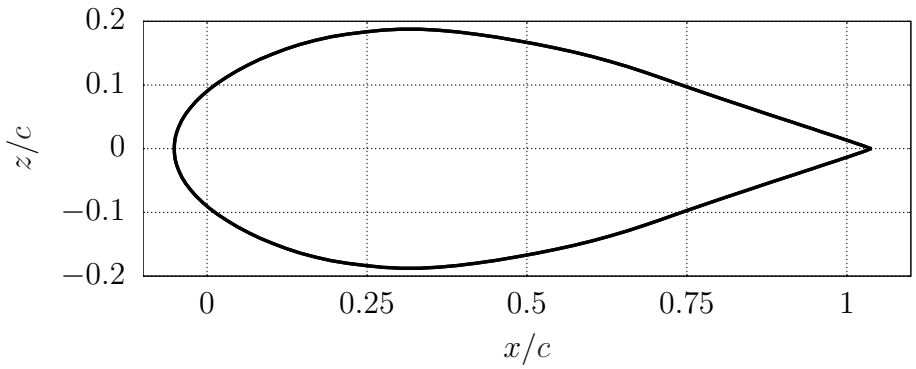

Figure 5.14: The geometry of the foil from Salvesen (1966).

However, the total length of the wake surface and the growth rate of the wake panel length, ζ_{wake}, are adjusted. A much lower value of $\zeta_{\text{wake}} = 0.02$ is used for the wake growth rate. The smaller growth rate will result in a much smaller maximum panel length. This is important because it is essential that the wake surface lie directly on a streamline of the viscous flow and smaller panel lengths will give better resolution of the wake surface.

As shown in Fig. 5.16, the wake surface is placed on a streamline in the free-surface calculations. If the total length of the wake surface is greater than $3c$ then the wake surface is not placed exactly on a streamline of the flow because the Navier-Stokes grid becomes more coarse and it is more difficult to calculate the exact location of the streamline. If the wake surface is not placed directly on a streamline, then it seems to appear as another body which results in spurious free-surface elevations. Fig. 5.17 shows the effect of the total wake surface length on the free-surface elevation. It appears that the free-surface elevation is converging as the wake surface length increases and that a total length of $3c$ is sufficient. This length will be used in all subsequent calculations.

Fig. 5.18 shows the calculated results for the $h/c = 1.5$ submergence. The linear viscous potential free-surface elevations are compared to the experimental result as well as the second order results for three different Fn_c. Fig. 5.19 gives the same

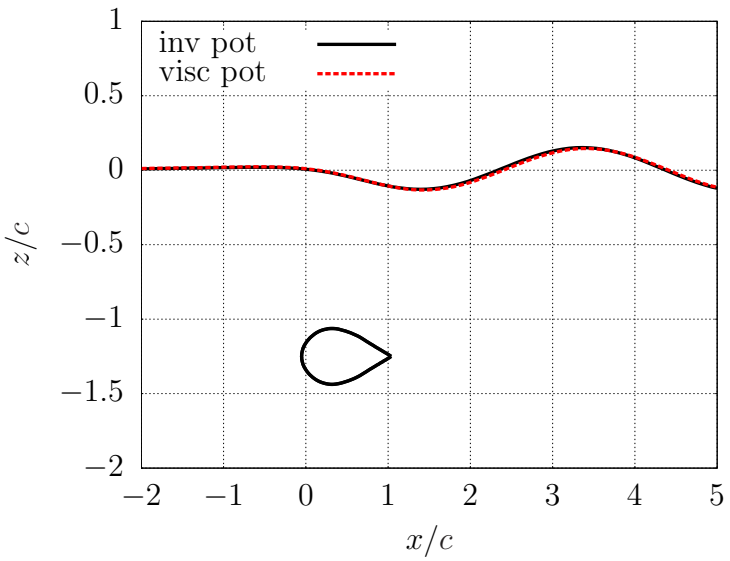

(a) The foil under the free surface for $h/c = 1.25$, $\mathrm{Fn_c} = 0.79$, $\mathrm{Fn_h} = 0.71$.

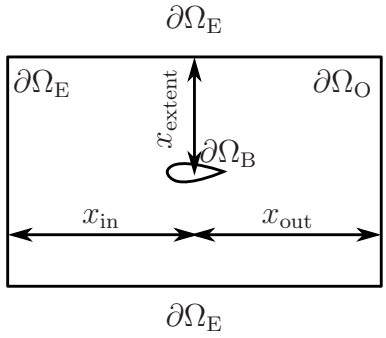

(b) The Navier-Stokes domain.

Figure 5.15: The body definition and domain of the Navier-Stokes sub-problem for the Salvesen foil.

comparison for the $h/c = 1.25$ submergence.

The agreement to experiments is acceptable for most cases considering that there is likely error present in the original experimental measurement as well as in the process of reproducing the data from the original paper. It is interesting that in some cases the amplitude of the free-surface waves calculated from the viscous potential is larger than the inviscid results, while in other cases the opposite occurs. It is possible that this is due to the lift on the body. In the cases where the free-surface amplitude is smaller for the viscous potential, the lift is positive. The opposite is true for the cases in which the amplitude of the free-surface waves calculated from the viscous potential is larger. Similar to the bottom-mounted bump results, the higher-order inviscid free-surface elevation agrees better with the experiments than the linear viscous potential result for most cases.

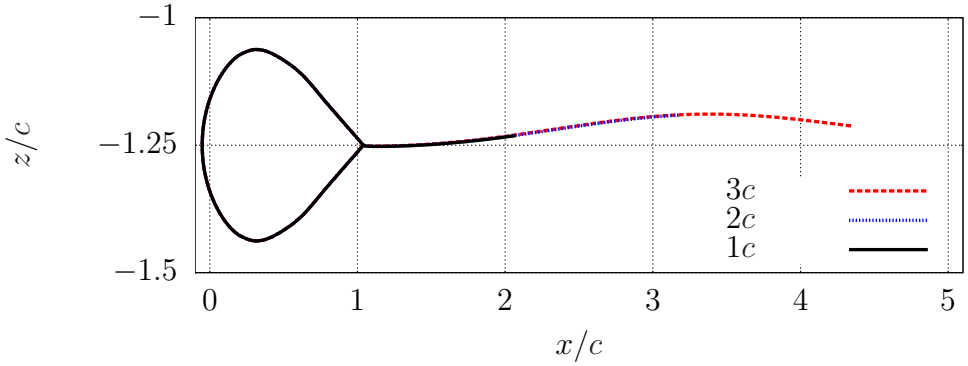

Figure 5.16: The wake panel distribution with varying total length for the Salvesen foil.

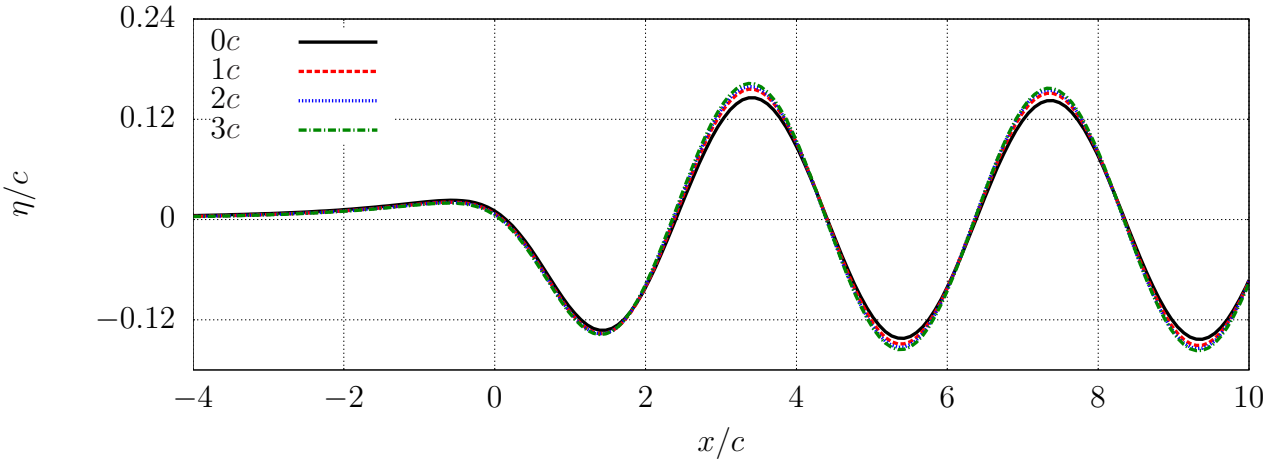

Figure 5.17: The effect of the total wake surface length on the free-surface elevation for the Salvesen foil at $\mathrm{Fn_h} = 0.79$ and $h/c = 1.25$.

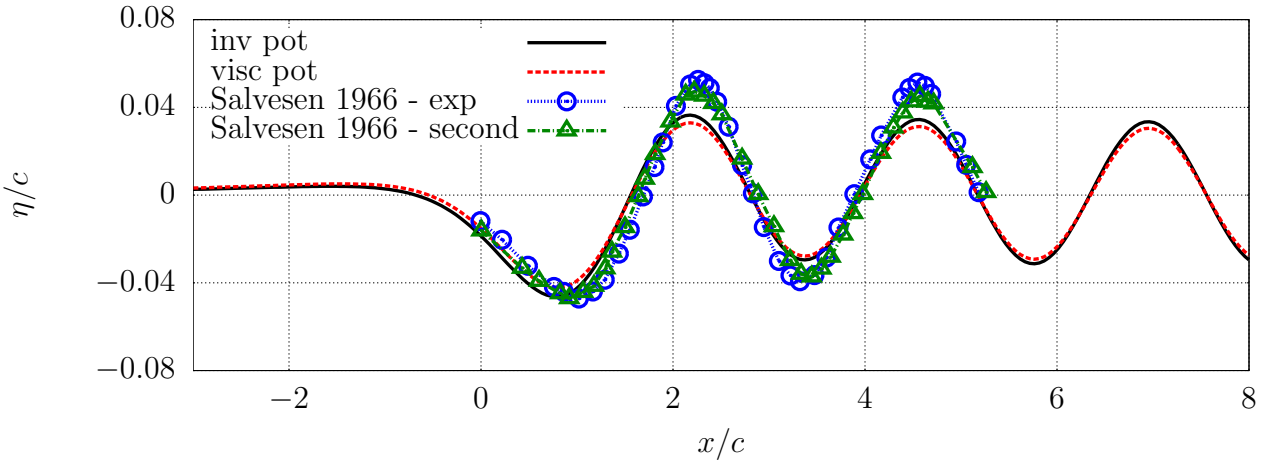

(a) $h/c = 1.5$, $\mathrm{Fn_c} = 0.62$, $\mathrm{Fn_h} = 0.50$, $s_{exp} \approx 1/25$, $s_\varphi \approx 1/40$

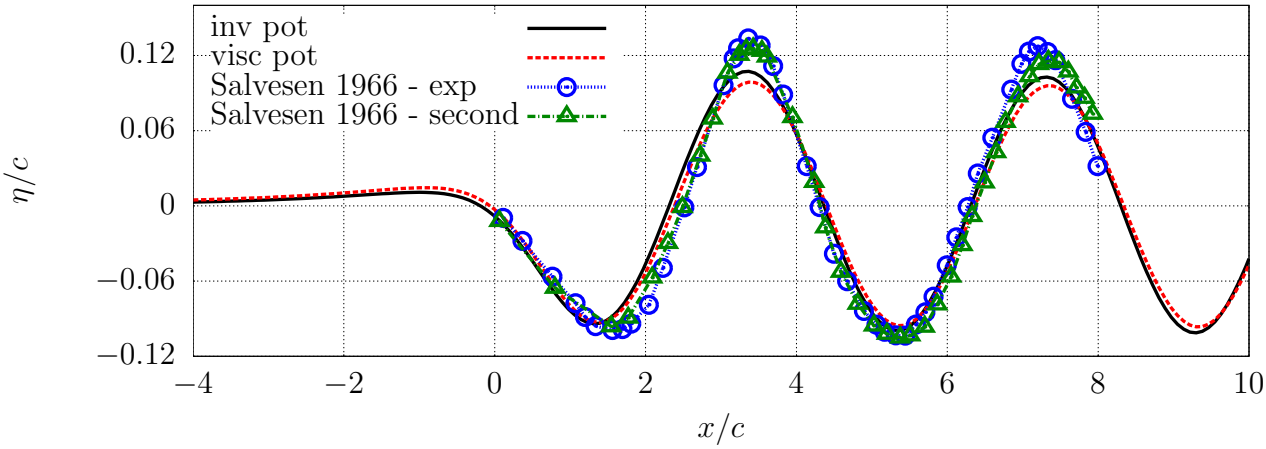

(b) $h/c = 1.5$ $\mathrm{Fn_c} = 0.79$, $\mathrm{Fn_h} = 0.65$, $s_{exp} \approx 1/17$, $s_\varphi \approx 1/21$

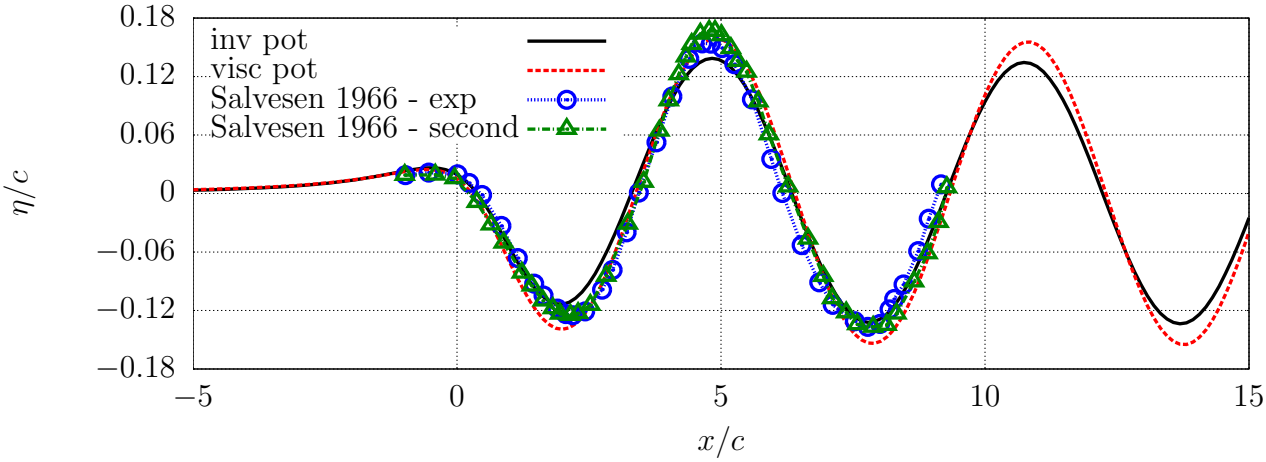

(c) $h/c = 1.5$ $\mathrm{Fn_c} = 0.97$, $\mathrm{Fn_h} = 0.79$, $s_{exp} \approx 1/19$, $s_\varphi \approx 1/20$

Figure 5.18: Free-surface profiles for a range of $\mathrm{Fn_c}$ at $h/c = 1.5$ compared to the numerical and experimental results from Salvesen (1966).

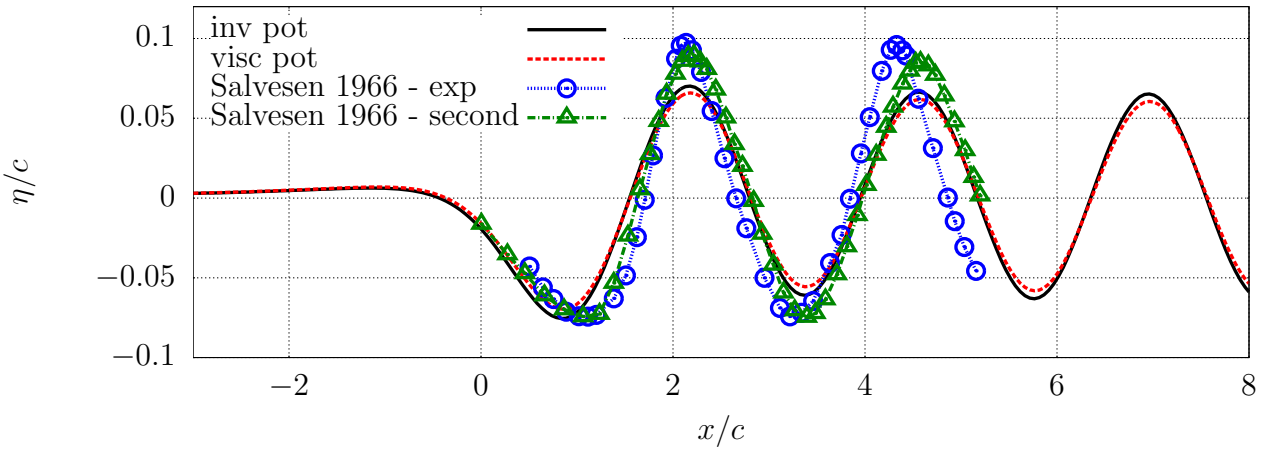

(a) $h/c = 1.25$ $\mathrm{Fn_c} = 0.62$, $\mathrm{Fn_h} = 0.55$, $s_{exp} \approx 1/13$, $s_\varphi \approx 1/20$

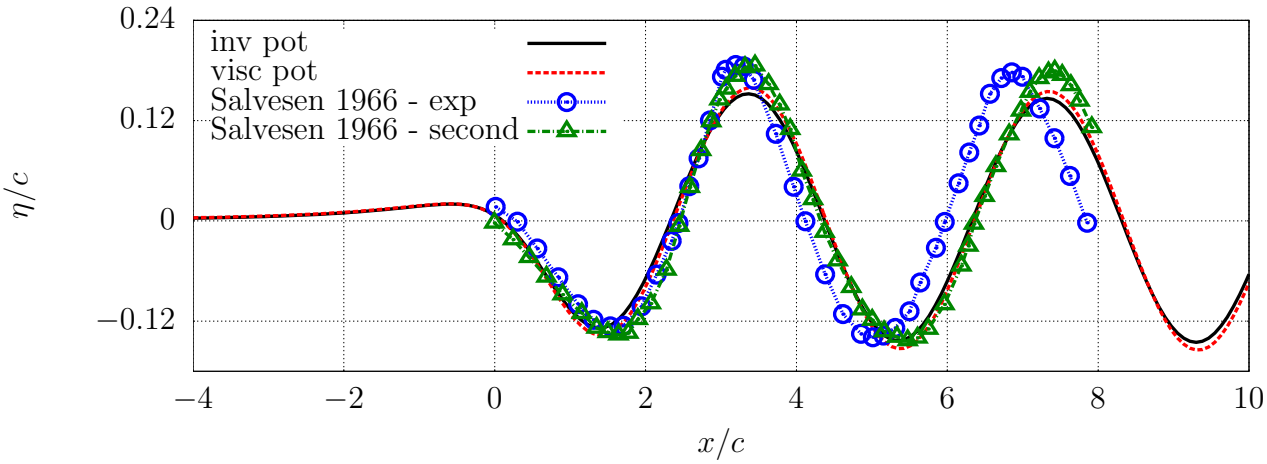

(b) $h/c = 1.25$ $\mathrm{Fn_c} = 0.79$, $\mathrm{Fn_h} = 0.71$, $s_{exp} \approx 1/11$, $s_\varphi \approx 1/14$

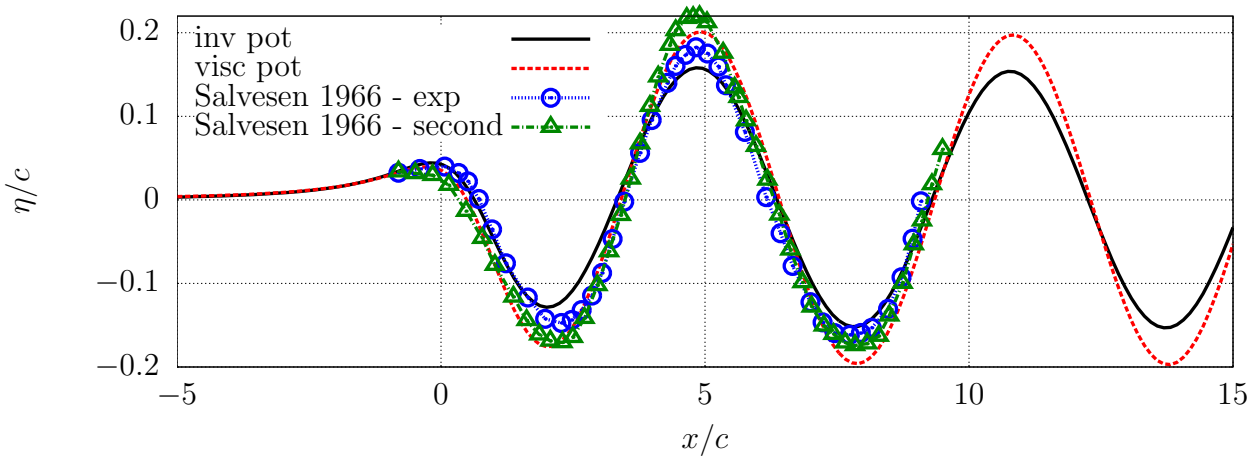

(c) $h/c = 1.25$ $\mathrm{Fn_c} = 0.97$, $\mathrm{Fn_h} = 0.87$, $s_{exp} \approx 1/16$, $s_\varphi \approx 1/19$

Figure 5.19: Free-surface profiles for a range of $\mathrm{Fn_c}$ at $h/c = 1.25$ compared to the numerical and experimental results from Salvesen (1966).

5.4 Summary

In this chapter, free-surface problems were solved using the velocity decomposition approach. In this approach, all free-surface effects are included through the viscous potential and the effects of viscosity at the free surface are neglected. The applicability of the velocity decomposition approach to solve free-surface problems depends almost entirely on the suitability of the free-surface conditions satisfied within the viscous potential sub-problem. Currently, the viscous potential satisfies the inviscid linear combined free-surface condition.

Although the use of velocity decomposition for free-surface flow seems limited, it does, however, offer the possibility of large computational savings. Although no rigorous benchmarking is performed in this chapter, the run times of all cases presented are on the order of 5-20 minutes. From personal experience, this is much less time than is required to calculate a fully viscous result by solving the full Navier-Stokes problem with an interface-capturing technique. Additional time savings is found when comparing different submergences of the same body. It is very simple to vertically translate the reduced Navier-Stokes domain under the free surface. It would be much more complicated, and time consuming, to create individual grids for each submergence (which would be required if using a Navier-Stokes solver with interface capturing).

The primary advantage of using velocity decomposition for free-surface flows lies in the ability to quickly calculate results for the viscous flow around a fully submerged body.

CHAPTER 6

Conclusions, Contributions and Possibilities for Future Work

6.1 Conclusions and Contributions

In this work, the velocity decomposition approach was extended to 2D lifting and free-surface problems. Central to this extension was the formulation of the viscous potential for lifting flow. This involved the development of the source and dipole wake distribution and the condition on the total body-bound circulation. The source and dipole wake distribution allows for the asymmetry in the viscous wake which is present in lifting flows to be included in the viscous potential. The total circulation condition allows for the viscous potential to correctly capture the loss of lift due to separation, which is purely a viscous effect. A linear free-surface solver was also included in the velocity potential in order to solve free-surface problems. Many small modifications to the computer code were also made in order to achieve a much greater computational efficiency.

The velocity decomposition approach to solving the Navier-Stokes problem presented in this thesis is a continuation of the work presented in Edmund (2012). Therefore, it is especially important to differentiate the contributions from Edmund (2012) to those presented here. In Edmund (2012), the velocity decomposition approach was developed and successfully applied to 2D and 3D, steady, non-lifting problems.

Specifically, the body-boundary condition for the viscous potential was developed and implemented. The work by Edmund (2012) was used as a starting point for the work presented here.

The application of velocity decomposition to the flow over a NACA0012 at two different Re's and angles of attack demonstrated the accuracy and efficiency of the approach. Specifically, it was demonstrated that the proposed approach is successful in calculating a viscous potential for lifting problems. In the laminar case, the lift and drag coefficients where predicted to within 0.1% accuracy on a Navier-Stokes domain with $x_{\text{extent}}/c = 2.0$ using velocity decomposition. The speed-up was 7.5× compared to the conventional Navier-Stokes solver.

The results of the application of velocity decomposition to free-surface problems were not as promising when compared to experimental and higher-order inviscid results. The use of a linear free-surface condition appears to hinder the quality of the results. However, for problems where the linear theory is valid, the possibility of large computational savings is present. Although no rigorous benchmarking was performed, the run times of all cases presented were on the order of 5-20 minutes. Additional time savings could also be found when comparing different submergences of the same body. It is very simple to vertically translate the reduced Navier-Stokes domain under the free surface. It would be much more complicated, and time consuming, to create individual grids for each submergence (which would be required if using a Navier-Stokes solver with interface capturing). The primary advantage of using velocity decomposition for free-surface flows lies in the ability to quickly calculate results for the viscous flow around a fully submerged body.

6.2 Possibilites for Future Work

The velocity decomposition approach presented here has been shown to be very accurate and efficient in the numerical solution of the Navier-Stokes problem. The current results are very promising and suggest that velocity decomposition can be applied to a wide range of problems. In this section, modifications, improvements, and suggestions for future work are presented.

Ideally, the velocity decomposition approach would eventually be developed for 3D, unsteady problems with multiple surface-piercing bodies and a nonlinear free-surface condition which also accounts for the viscous effects at the air-water interface. This, however, is quite an undertaking. From the results presented here, it would seem that it should be straightforward to develop velocity decomposition for 3D, steady problems with a fully submerged body and a nonlinear free-surface. The application to 3D, deeply-submerged problems has already been explored in Edmund (2012). Another straightforward development would be including the effects of multiple bodies. This would be purely a coding task because the theory behind the velocity decomposition would not be affected.

Many small improvements have been made to the various numerical tasks that are involved in calculating the viscous potential. However, there are still improvements to be made. The iterative loop to calculate the viscous potential could benefit from a more insightful convergence criteria. The sampling algorithm which was developed to sample the vorticity field in order to determine the $\delta-$boundary occasionally becomes "stuck" on high-aspect ratio or highly skewed cells. If there were an automatic approach to determining the convergence of the velocity decomposition updates, then the parameter N_{updates} could be discarded and the solver would become more user friendly. Also, it has been suggested that a mixed Dirichlet / Neumann boundary condition on the total velocity on the reduced boundary may help reduce the spurious vorticity generated there.

BIBLIOGRAPHY

Anderson, E., Bai, Z., Bischof, C., Blackford, S., Demmel, J., Dongarra, J., Du Croz, J., Greenbaum, A., Hammarling, S., McKenney, A., and Sorensen, D. *LAPACK Users' Guide*. Society for Industrial and Applied Mathematics, Philadelphia, PA, Third edition, 1999. ISBN 0-89871-447-8 (paperback).

Arfken, G. and Weber, H. *Mathematical Methods for Physicists*. Elsevier Academic Press, 6th edition, 2005.

Baar, J. and Price, W. Developments in the calculation of the wavemaking resistance of ships. In *Proceedings of The Royal Society London*, volume 416, pages 115–147, 1988.

Bai, K. J. and Han, J. H. A localized finite-element method for the nonlinear steady waves due to a two-dimensional hydrofoil. *Journal of Ship Research*, 38(1):42–51, 1994.

Bal, S. and Kinnas, S. A BEM for the prediction of free surface effects on cavitating hydrofoils. *Computational Mechanics*, 28(3-4):260–274, 2002.

Brard, R. The Neumann-Kelvin problem for surface ships. Technical Report 11, Bassin d'Essais des Carenes, Paris, France, 1971.

Cahouet, J. *Etude Numerique et Experimentale du Probleme Bidimensionnel de la Resistance de Vagues Non-Lineaire*. PhD thesis, ENSTA, Paris, France, 1984.

Campana, E., Di Mascio, A., Esposito, P., and Lalli, F. Viscous-inviscid coupling in free surface ship flows. *International Journal for Numerical Methods in Fluids*, 21 (9):699–722, 1995.

Cao, Y., Schultz, W., and Beck, R. Three-dimensional desingularized boundary integral methods for potential problems. *International Journal for Numerical Methods in Fluids*, 12(8):785–803, 1991.

Chen, C. Y. and Noblesse, F. Comparison between theoretical predictions of wave resistance and experimental data for the wigley hull. *Journal of Ship Research*, 27 (4), December 1983.

Chen, H.-C. and Lee, S.-K. Interactive RANS/Laplace method for nonlinear free surface flows. *Journal of Engineering Mechanics*, 122, 1996.

Chen, H. and Lee, S. RANS/Laplace calculations of nonlinear waves induced by surface-piercing bodies. *Journal of Engineering Mechanics*, 125:1231, 1999.

Dawson, C. A practical computer method for solving ship-wave problems. In *Proceedings 2nd International Conference on Numerical Ship Hydrodynamics*, pages 30–38. DTIC Document, 1977.

Drela, M. XFOIL: An analysis and design system for low Reynolds number airfoils. In *Low Reynolds Number Aerodynamics*, volume 54 of *Lecture Notes in Engineering*, pages 1–12. Springer, 1989.

Edmund, D. O., Maki, K. J., and Beck, R. F. An improved viscous / inviscid velocity decomposition method. In *International Workshop on Water Waves and Floating Bodies (IWWWFB)*, volume 26, 2011.

Edmund, D. *A Velocity Decomposition Method for Efficient Numerical Computation of Steady External Flows*. PhD thesis, University of Michigan, 2012.

Ferrant, P., Gentaz, L., Alessandrini, B., Luquet, R., Monroy, C., Ducrozet, G., Jacquin, E., and Drouet, A. Fully nonlinear potential / RANSE simulation of wave interaction with ships and marine structures. In *Proceedings of the ASME 27th International Conference on Offshore Mechanics and Artic Engineering*, 2008.

Gresho, P. and Sani, R. On pressure boundary conditions for the incompressible Navier-Stokes equations. *International Journal for Numerical Methods in Fluids*, 7(10):1111–1145, 1987.

Guillerm, P. and Alessandrini, B. 3D free-surface flow computation using a RANSE/Fourier-Kochin coupling. *International Journal for Numerical Methods in Fluids*, 43(3):301–318, 2003.

Hafez, M., Shatalov, A., and Nakajima, M. Improved numerical simulations of incompressible flows based on viscous/inviscid interaction procedures. *Computers & Fluids*, 36(10):1588–1591, 2007.

Hafez, M., Shatalov, A., and Wahba, E. Numerical simulations of incompressible aerodynamic flows using viscous/inviscid interaction procedures. *Computer Methods in Applied Mechanics and Engineering*, 195(23-24):3110–3127, 2006.

Hoekstra, M. and Eça, L. Parnassos: An efficient method for ship stern flow calculation. In *Third Osaka Colloquium on Advanced CFD Applications to Ship Flow and Hull Form Design, Osaka, Japan*, 1998.

Iafrati, A. and Campana, E. A domain decomposition approach to compute wave breaking (wave-breaking flows). *International Journal for Numerical Methods in Fluids*, 41(4):419–445, 2003.

Katz, J. and Plotkin, A. *Low-Speed Aerodynamics*. McGraw-Hill, Inc., 1991.

Kendon, T., Sherwin, S., and Graham, J. An irrotational / vortical split-flow approach to viscous free surface flow. In *2nd MIT Conference on Computational Fluid and Solid Mechanics*, 2003.

Kim, K., Sirviente, A., and Beck, R. F. The complementary RANS equations for the simulation of viscous flows. *International Journal for Numerical Methods in Fluids*, 48:199–229, January 2005.

Kim, S., Rhee, B., Shan, H., Gorski, J., Paterson, E., and Maki, K. A scalable multiphase RANS capability based on object-oriented programming and its applications to ship hydrodynamics. In *Gothenburg 2010: A workshop on CFD in Ship Hydrodynamics*, 2010.

Kochin, N., Kibel, I., and Roze, N. *Theoretical Hydrodynamics*. John Wiley and Sons, 1964.

Lighthill, M. On displacement thickness. *Journal of Fluid Mechanics*, 4(04):383–392, 1958.

Luquet, R., Gentaz, L., Ferrant, P., and Alessandrini, B. Viscous flow simulation past a ship in waves using the SWENSE approach. In *25th Symposium on Naval Hydrodynamics. St. John's, Newfoundland and Labrador, Canada*, 2004.

Michell, J. The wave resistance of a ship. *Philosophical Magazine Series 5*, 45(272): 106–123, 1898.

Morino, L. Helmholtz decomposition revisited: vorticity generation and trailing edge condition. *Computational Mechanics*, 1(1):65–90, 1986.

Morino, L., Salvatore, F., and Gennaretti, M. A new velocity decomposition for viscous flows: Lighthill's equivalent-source method revisited. *Computer Methods in Applied Mechanics and Engineering*, 173(3-4):317–336, 1999.

Noblesse, F. A slender-ship theory of wave resistance. *Journal of Ship Research*, 27 (1):13–33, March 1983.

Nordström, J., Mattsson, K., and Swanson, C. Boundary conditions for a divergence free velocity–pressure formulation of the navier–stokes equations. *Journal of Computational Physics*, 225(1):874–890, 2007.

Patankar, S. V. *Numerical Heat Transfer and Fluid Flow*. Taylor & Francis, 1980.

Raven, H. Variations on a theme by Dawson. In *Seventeenth Symposium on Naval Hydrodynamics*, page 151. National Academies, 1989.

Rempfer, D. On boundary conditions for incompressible navier-stokes problems. *Applied Mechanics Reviews*, 59:107, 2006.

Rempfer, D. Two remarks on a paper by Sani et al. *International Journal for Numerical Methods in Fluids*, 56(10):1961–1965, 2008.

Rosemurgy, W. J., Maki, K. J., and Beck, R. F. The application of velocity decomposition to airfoil problems. In *International Workshop on Water Waves and Floating Bodies (IWWWFB)*, volume 28, 2013.

Rumsey, C. L. and Ying, S. X. Prediction of high lift: review of present CFD capability. *Progress in Aerospace Sciences*, 38(2):145–180, 2002.

Salvesen, N. and Von Kerczek, C. Numerical solutions of two-dimensional nonlinear body-wave problems. In *Proc. 1st. Int. Conf. on Numerical Ship Hydrodynamics*, pages 279–293, 1975.

Salvesen, N. Second-order wave theory for submerged two-dimensional bodies. In *6th Symposium on Naval Hydrodynamics*, 1966.

Sani, R. L., Shen, J., Pironneau, O., and Gresho, P. Pressure boundary condition for the time-dependent incompressible navier–stokes equations. *International Journal for Numerical Methods in Fluids*, 50(6):673–682, 2006.

Scullen, D. *Accurate Computation of Steady Nonlinear Free-Surface Flows*. PhD thesis, University of Adelaide, February 1998.

Spalart, P. and Allmaras, S. A one-equation turbulence model for aerodynamic flows. *AIAA Journal*, 92(0439), 1992.

Thomas, J. L. and Salas, M. Far-field boundary conditions for transonic lifting solutions to the Euler equations. *AIAA Journal*, 24(7):1074–1080, 1986.

Wang, Y., Sproston, J. L., and Millward, A. Calculations of wave resistance for a high-speed displacement ship. *International Shipbuilding Progress*, 43(435):189–207, 1996.

Weller, H., Tabor, G., Jasak, H., and Fureby, C. A tensorial approach to computational continuum mechanics using object-oriented techniques. *Computers in Physics*, 12:620, 1998.